Synthesis and characterization of $BaTiO_3$ and $SrTiO_3$ thin film capacitors with RuO_2 electrodes

Dissertation

zur Erlangung des akademischen Grades
Doktor rerum naturalium
(Dr. rer. nat.)

vorgelegt dem
Fachbereich Physik der
Universität Duisburg-Essen

Von
Y. K. Vayunandana Reddy
aus
Kadapa, India

Erstgutachter: Prof. Dr. D. Mergel
Zweitgutachter: Prof. Dr. V. Buck

Tag der mündlichen Prüfung: 12th July, 2006

Essen, May 2006

List of Tables

Chapter 1

Table 1.1 Important ferroelectric materials. 30

Table 1.2 Analytical techniques and characterization of the thin films. 41

Chapter 3

Table 3.1 XRR measurement results of RuO_2 thin films. 71

Table 3.2 Preparation parameters and resistivity results of RuO_2 thin films. 73

Chapter 4

Table 4.1The deposition parameters, dielectric permittivity and activation energies for all investigated capacitors, ε_r values are obtained at room temperature. 83

Table 4.2 Literature comparison of ε_r values for $SrTiO_3$ films. 97

Chapter 5

Table 5.1The deposition parameters, dielectric permittivity (ε_r) and activation energies for investigated capacitors. 105

Table 5.2 Literature values of ε_r for $BaTiO_3$ films. 117

Chapter 6

Table 6.1The deposition parameters, dielectric permittivity (ε_r) and activation energies for investigated capacitors. 125

Chapter 7

Table 7.1 and Table 7.2 The deposition parameters of C-H-B-S and C-H-B-BS heterostructure system. 141

List of Figures

Chapter 1

Fig. 1.1 Parallel plate capacitor filled with dielectric under short circuit condition (*E* = constant). 7

Fig. 1.2 Various polarization processes (a) electronic polarization (b) ionic polarization, (c) orientation polarization, and (d) space charge polarization. 18

Fig. 1.3 Frequency dependent relative dielectric constant. 19

Fig. 1.4 Ferroelectric hysteresis: polarization, *P,* as a function of the Electric field, *E*, dashed line single domain single crystal, full line polycrystalline. 22

Fig. 1.5 Barium titanate phase transition. 23

Fig. 1.6 (a) Barium titanate crystal structure with octahedral (b) BTO phase transitions with respective to temperature and their other properties. 24

Fig. 1.7 Relative dielectric constant (ε_r) and dielectric loss (Tan δ) of $BaTiO_3$ ceramic. 25

Fig. 1.8 Phase diagram of $Ba_xSr_{1-x}TiO_3$. 26

Fig. 1.9 Phase transitions for different compositional $Ba_xSr_{1-x}TiO_3$. 27

Fig. 1.10 Applications of ferroelectric materials. 28

Fig. 1.11 Bismuth layer structure $SrBi_2Ta_2O_9$. 29

Fig. 1.12 Rutile structure of RuO_2. 35

Fig. 1.13 Sputtering mechanism. 36

Fig. 1.14 Capacitively coupled rf magnetron sputter target. 37

Fig. 1.15 Structure zone model diagram for sputter deposited metals. 38

Fig. 1.16 (a) von Ardenne LS 500 S DC/RF magnetron sputter machine,
(b) inside the sputter chamber and two sputter cathodes. 40

Fig. 1.17 Our capacitor structure. 41

Chapter 2

Fig. 2.1 Density and deposition rate of BTO thin films deposited at various temperatures. The deposition rate was calculated from the measured mass per area and the crystalline density of $BaTiO_3$ (5.85 g/cm^3, dashed line). 50

Fig. 2.2 XRD spectra of the BTO thin film deposited at 450°C. The intensity has been normalized in order to account for the finite thickness of the thin film [16]. The vertical dotted lines represent the position of the reflexes of the cubic structure. The PDF intensities of the cubic and the hexagonal phase are indicated by the diamond and the cross symbols, respectively. The vertical bold lines represent the position of some hexagonal reflexes that are clearly distinct from the cubic ones. 51

Fig. 2.3 Normalized XRD spectra of the BTO thin film deposited at various temperatures. The reflexes of the cubic phase are marked with vertical dotted lines. The powder diffractogram of the hexagonal powder is represented by the bold vertical lines close to the x-axis. From bottom to top: 450°C, 600°C, and 750°C, respectively. 51

Fig. 2.4 Lattice distortion of BTO thin films deposited at various temperatures, calculated from Eq. (1). 54

Fig. 2.5 Plot of $\Delta(2\theta)$ (full width at half maximum) for some reflexes with first and second order peaks vs. $\sin\theta$. 54

Fig. 2.6 Micro-strain (statistical strain) of the BTO thin films evaluated according to Eq. (3). 54

Fig. 2.7 Transmittance and simulated spectra of BTO thin films deposited at 600°C with different simulation parameters (Simulated-3L-M and Simulated-3L-M-rough, represented as, simulated with 3 layer model and with rough interface, respectively.). 56

Fig. 2.8 Band gap (E_g) and pore volume (V_{por}) as calculated from the optical simulation. 56

Fig. 2.9 Refractive index *n* and extinction coefficient *k* (inset) as a function of wavelength for three samples deposited at 450°C, 600°C, and 750°C, respectively. 59

Fig. 2.10 Cross sectional SEM of the film deposited at 600°C (arrow marks indicates the growth change and the white line indicates crystal growth). 59

Fig. 2.11 Raman spectra of the BTO thin films prepared at different temperatures. Broken vertical and chain lines represent the Raman lines of the perovskite [30] and the hexagonal [27] phase, respectively. 61

Fig. 2.12 AFM images of the BTO thin films deposited at (a) 450°C, (b) 600 and (c) 750°C. 62

Chapter 3

Figs. 3.1a to d show x-ray diffractograms of RuO_2 thin films: (a) Films (~ 100 nm) deposited on glass substrates at R.T. and annealed at different temperatures, (b) Films (~70 nm) deposited on quartz substrates at different temperatures, (c) Films (~50 nm) deposited on different substrates at 540°C substrate temperature, (d) Films deposited at R.T on Si substrates later annealed at various temperatures. 69

Figs. 3.2a to c show the surface morphology of RuO_2 thin films: (a) and (b) film (~ 70 nm) deposited on quartz substrate at 300 and 700°C substrate temperatures, respectively, (c) film (~50 nm) deposited on Si/SiO_2 substrate at 540 °C. 71

Fig. 3.3 show the XRR curve with simulation of the R-4 sample. 71

Fig. 3.4 Cross-sectional SEM of $BaTiO_3$ capacitor with RuO_2 electrodes. 72

Fig. 3.5 show the resistivity vs. temperature for different thicknesses films. 73

Fig. 3.6a to c show the Raman spectra of RuO2 thin films: (a) Films (~50 nm) deposited on different substrates at 540°C substrate temperature (b) Films (~70 nm) deposited on quartz substrates at different temperatures, (c) Films (~ 100 nm) deposited on glass substrates at R.T. and annealed at different temperatures. 75

Chapter 4

Fig. 4.1 XRD patterns of $SrTiO_3$ thin film capacitors normalized with respect to film thickness. The vertical dashed lines represent $SrTiO_3$ (coded as S) peaks and RuO_2 peaks (coded as R). The bottom diffractograms represents the uncoated Si substrate. Its peaks are marked with *. Fig. 4.1a. Capacitors prepared at 700°C with 5% oxygen. Top to bottom: CS-6 (220 nm), CS-8 (360 nm), CS-4 (960 nm). Fig. 4.1b. Capacitors prepared at different oxygen partial pressures. From top to bottom: CS-8 (5%), CS-11 (10%), CS-12 (20%), CS-13 (10%) all prepared at 700°C except CS-13 that was prepared at 500°C. 84

Fig. 4.2 Cross-sectional SEM of sample CS-4 prepared at 700°C with 5% O_2, thickness 960 nm. 85

Fig. 4.3 Impedance in the complex plane. Experimental data together with simulated curves. The full diamonds correspond to the decades starting at 10 Hz and the arrow indicates the direction of increasing frequency. Fig. 4.3a. Sample CS-13 prepared at 500°C with 10% O_2. The inset shows the equivalent circuit of one resistance and two RC elements in series used for the simulation. Fig. 4.3b. Data of sample CS-6 prepared at 700°C with 5% O_2 with the thickness 220 nm with deconvolution and simulated curve (dashed line). Fig. 4.3c. Sample CS-4 prepared at 700°C with 5% O_2 and a thickness of 960 nm. 87

Fig. 4.4 Imaginary part (Z'') of the impedance vs. frequency (f) of sample CS-6 for different measuring temperatures. 90

Fig. 4.5 Arrhenius plot, $\ln f_{max}$ vs. $1000/T$ [K^{-1}] for sample CS-6 (700°C, 5% O_2, 220 nm). 90

Fig. 4.6 Arrhenius plot of the bulk conductivity of all investigated capacitors (except CS-4), values obtained from the RC simulations. 93

Fig. 4.7 Frequency dependent dielectric permittivity (ε_r) as calculated from Eq. (2). The horizontal lines represent the values obtained for the high-frequency semicircle of the RCp-simulation attributed to the bulk STO grains. 93

Fig. 4.8 Inverse dielectric permittivity ($1/\varepsilon_r$) vs. temperature. Average of the values obtained from the RQ and RC simulations, with error bars. 93

Fig. 4.9 Dielectric loss ($\tan \delta$) vs. temperature for the three samples prepared at 700°C, 5% O_2, with different thicknesses. 96

Chapter 5

Fig. 5.1a to b: (a) X-ray diffractograms of all samples in the angular region of the (110) reflex of the perovskite structure, with the lines of the cubic (---), tetragonal (——) and hexagonal (– · – ·) single crystalline phases. CB-4 to CB-7: prepared at 600°C, CB-8: prepared at 450°C, CB-9 to CB-14: prepared at 750°C. The baseline of the various diffractograms has been shifted by an intensity of 500 with respect to the lower curve. (b) As Fig. 1a, for the (200) reflex. 106

Fig. 5.2 a and b: Cross-sectional SEM of $BaTiO_3$ capacitors deposited at 600°C substrate temperature. (a) CB-4 (30% O_2) and (b) CB-6 (10% O_2). 107

Fig. 5.3 Some Z'-Z'' plots of capacitors prepared at 600°C (a), 750°C (b) and 450°C (c). Experimental data points together with the curves obtained from the RC simulations. The frequency decades are marked with large filled squares. 108

Fig. 5.4 Imaginary part of the impedance vs. frequency of samples prepared at 600°C under various oxygen partial pressures. 109

Fig. 5.5 Dielectric permittivity as obtained from Eq. (2) vs. frequency for samples prepared at 600°C under various oxygen partial pressures. 111

Fig. 5.6 Dielectric permittivity as obtained from Eq. (2) vs. frequency for samples prepared at 750°C under various oxygen partial pressures. 111

Fig. 5.7 Dielectric permittivity obtained from the RC-simulations vs. temperature for the samples prepared at 600°C and 450°C. 113

Fig. 5.8 Dielectric permittivity obtained from the RC-simulations vs. temperature for the samples prepared at 750°C. 113

Fig. 5.9 Curie-Weiss plot of the dielectric permittivity for temperatures above the temperature of the maximum in Figs. 5.7 and 5.8. 115

Fig. 5.10 Dielectric loss tangent of the samples prepared at 750°C. 116

Fig. 5.11 Dielectric loss tangent of the samples prepared at 600°C. 116

Chapter 6

Fig.6.1 XRD diffractogram of BST-0.75 thin films (vertical lines indicate BST-0.75 phase).125

Fig.6.2 Cole-Cole plot of BST-0.75 thin films along with simulated curve (a) CBS-0.75-1 film annealed in O_2 (including deconvolution of high and low frequency curves), (b) CBS-0.75-2 film annealed in vacuum, (c) CBS-0.75-5 as deposited film at 700°C. 127

Fig. 6.3 Resistance of BST-0.75 films extracted from RQ simulations. (a) Grain, G and (b) grain boundary, GB. 128

Fig. 6.4 Relative dielectric permittivity of BST-0.75 films calculated from Eq. (2) with respect to frequency. 129

Fig. 6.5 (a) Dielectric permittivity of bulk grains of BST-0.75 films calculated from RQ simulations with respect to temperature (b) literature comparison. 131

Fig. 6.6 Arrhenius plot of bulk conductivity. 133

Fig. 6.7 Dielectric loss (tan δ) vs. frequency. 134

Chapter 7

Fig. 7.1 XRD diffractograms of the heterostructures of (a) C-H-B-S series (b) C-H-B-BS series. 142

Fig. 7.2 Cole-Cole plots of heterostructures (a) C-H-B-S series (BTO/STO) together with the simulated curve (dashed lines) (b) C-H-B-BS (BTO/BST) heterostructures together with the simulated curve (red). 144

Fig. 7.3 Relative dielectric permittivity calculated from Eq. (1) with respective frequency of the (a) C-H-B-S series heterostructures, (b) C-H-B-BS series heterostructures. 145

Fig. 7.4 Arrhenius plot of bulk conductivity of C-H-B-S series heterostructures. 146

Fig. 7.5 Bulk permittivity calculated from the RQ simulations of (a) C-H-B-S series heterostructures (b) literature comparison (c) C-H-B-BS heterostructure series. 147-9

Fig. 7.5(d) dielectric constant vs. individual layer thickness of C-H-B-S series (Traingles: obtained from Eq.(1) and Sqaures: obtained from RQ simulations). 150

Fig. 7.6 Dielectric loss of C-H-B-S series heterostructures. 151

Acknowledgements

During four years of my stay at the University of Duisburg-Essen for my Ph.D., I have had a very great time, both in academic and personal life. I would like to thank everybody who gave endless support to me.

First of all, I wish to express deep gratitude to my supervisor, Prof. Dr. Dieter Mergel, for his guidance, support, encouragement, and friendly discussions during this work.

I am grateful to all the “Graduiertenkolleg 689” students, to the faculty members and especially to our former secretary, Mrs. Birgit Wöstefeld, for their great co-operation and encouragement.

I had the great pleasure of working with many skillful scientists and technicians. They enabled me to successfully finish this work. I am greatly indebted to Mr. Martin and Mrs. Margarete Sulkowski for measurements of XRD and XRF, respectively, to Mr. Thorsten Balgar and Mr. Daniel for measurement of AFM, Mr. Werner Oswald and Ms. Tamara Gurenko for measurements and analysis of impedance spectroscopy, Mr. Stephan Reuter for measurements of Raman spectroscopy, Dr. Hans-Werner Becker (RU Bochum) for measurements of RBS.

I would like to thank all former members of the Thin Film Technology Group for timely help and support at the initial stage of my work: Mr. Marc Stroisch, Mr. Ingo Erdman, and Dr. Zhaohui Qiao.

I am sincerely thankful to Mr. Phillip Dellinger and Ms. Janika Boltz. I have had a good time with them in the office and enjoyed the candies they offered to me during their Diploma work.

It is a great pleasure to thank Mr. Martin Jerman for helping me by all means during my stay at the university and for translating the summary into German.

My sincere thanks go to all of my friends whose support and help made my work really enjoyable.

My sincere thanks go to my former Indian supervisor for my M. Phil. dissertation,
Prof. K. N. Shrivastava and Dr. K. Venkata Reddy for their encouragement during my stay in the University of Hyderabad, India.

My warm and deepest thanks are to my parents and my brother for their constant care, support and encouragement.

Essen,
Y. K. Vayunandana Reddy

Table of contents

List of Tables **2**

List of Figures **3**

Acknowledgements **10**

1. Introduction **16**

1.1. Dielectrics 16

1.2. Ferroelectrics 20

1.2.1. Ferroelectricity 21

1.2.1.1.Barium titanate 24

1.2.1.2.Strontium titanate 25

1.2.1.3.Barium strontium titanate 26

1.2.2. Other important properties of ferroelectrics 27

1.2.3. Alternative structural oxides 29

1.3. Literature review of thin films 30

1.4. The radio frequency (rf) magnetron sputtering method 36

1.4.1. Sputtering process mechanism 36

1.4.2. Magnetron sputtering 36

1.4.3. Radio frequency (rf) magnetron sputtering 37

1.5. Structure zone model 38

1.6. Experimental setup 39

1.7. Thin film capacitor structure 40

1.8. Film characterization 41

1.9. Scope of the dissertation 42

References 44

2. Structural and optical properties of $BaTiO_3$ thin films deposited by radio-frequency magnetron sputtering at various substrate temperatures 46

2.1. Introduction …… 47
2.2. Experimental details …… 48
2.3. Results and discussion …… 49
2.3.1. Deposition rate, packing density and composition …… 49
2.3.2. Structural properties from XRD …… 51
2.3.3. Optical properties from transmittance …… 55
2.3.4. Raman spectroscopy …… 60
2.3.5. Surface morphology …… 62
2.4. Conclusions …… 62
References …… 64

3. Structural and electrical properties of RuO_2 thin films prepared by rf-magnetron sputtering and annealing at different temperatures 66

3.1. Introduction …… 67
3.2. Experimental …… 68
3.3. Results and discussion …… 69
3.3.1. Structural and morphological characterization…… 69
3.3.2. Electrical properties …… 72
3.3.3. Raman spectroscopy study …… 74
3.4. Integration into capacitor structure: Issues to be considered 76
3.5. Conclusions …… 76
References …… 78

4. Impedance spectroscopy study of $RuO_2/SrTiO_3$ thin film capacitors prepared by radio-frequency magnetron sputtering 80

4.1. Introduction …… 81
4.2. Experimental …… 82

4.3. Results and discussion ………………………………………………………… 83
4.3.1. Structural analysis …………………………………………………… 83
4.3.2. Impedance spectroscopy ………………………………………….. 86
4.4. Conclusions ……………………………………………………………… 97
References ……………………………………………………………………. 99

5. Frequency and temperature dependent electrical properties of $BaTiO_3$ thin film capacitors studied by complex impedance spectroscopy 102

5.1. Introduction ..………………………………………………………….. 103
5.2. Experimental ……………………………………………………………. 104
5.3. Results and discussion …………………………………………………….. 105
5.3.1. Structural properties ………………………………………………. 105
5.3.2. Complex impedance study …………………………………………… 107
5.3.2.1. Bulk conductivity and relaxation time ………………………… 110
5.3.2.2. Dielectric properties …………………………………………… 110
5.3.2.3. Dielectric loss ……………………………………………….. 116
5.4. Conclusions …………………………………………………………... 117
Appendix ……………………………………………………………………. 118
References ………………………………………………………………….. 119

6. Annealing effects on structural and dielectric properties of $Ba_{0.75}Sr_{0.25}TiO_3$ thin film capacitors with RuO_2 electrodes 122

6.1. Introduction ……………………………………………………………. 123
6.2. Experimental …………………………………………………………… 124
6.3. Results and discussion ……………………………………………………. 125
6.3.1. X-ray diffraction study ………………………………………….. 125
6.3.2. Impedance spectroscopy study …………………………………. 126
6.4. Conclusions ………………………………………………………….. 134
References ………………………………………………………………………... 136

7. **Dielectric properties of $BaTiO_3$ / $SrTiO_3$ and $BaTiO_3$ / $Ba_{0.75}Sr_{0.25}TiO_3$ thin film heterostructures with RuO_2 electrodes** **138**

7.1. Introduction …………………………………………………………… 139
7.2. Experimental ………………………………………………………….. 141
7.3. Results and discussion ………………………………………………… 142
7.3.1. Phase analysis …… ………………………………………… 142
7.3.2. Impedance data ………… ………………………………... 143
7.4. Conclusions …………………………………………………………… 151
References ………………………………………………………………… 153

8. Summary (English) …………………….. ……………………………. 155
Zusammenfassung (German) 158
సంగ్రహం (Telugu) 162

Appendix A ……………………………………………………………….. 164
Appendix B 170

1. Introduction

In this chapter, we discuss the basics of dielectrics and ferroelectrics and their related properties, and typical ferroelectric materials. In subsequent sections we give an overview of the experimental results of different researchers, and then are given some basics of radio-frequency (RF) magnetron sputtering and their mechanism, and structure zone model and finally the scope of the dissertation.

1.1 Dielectrics:

(Source: Ref. 2)

Dielectrics are insulating materials that do not conduct electric current due to the very low density of free charge carriers. Here the electrons are bound to microscopic regions within the material, i.e. the atoms, molecules, in contrast to being freely movable in and out of macroscopic system under consideration. They are used technically because of their property of polarization to modify the dielectric function of the vacuum, e.g. to increase the capacity of capacitors. Dielectrics exhibit an electric dipole structure, in which positive and negative electrically charged entities are separated on a molecular or atomic level by an applied electric field. This is called polarization.

According to Poisson's equation, each free charge acts as a source for the dielectric displacement *D*

$$DivD = \rho_{free} \tag{1.1}$$

Here ρ_{free} defines the density of free carriers. Under the electric field (*E*), *D* is described by

$$D = \varepsilon_0 E + P \tag{1.2}$$

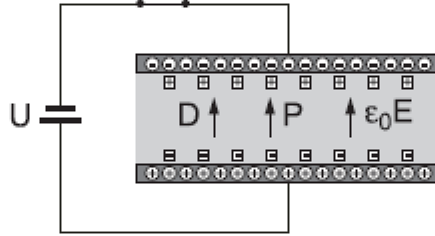

Fig. 1.1 Parallel plate capacitor filled with dielectric under short circuit condition (E = constant) [2]

The term $\varepsilon_0 E$ describes the vacuum contribution to the displacement D caused by an electric field E and P represents the electrical polarization of the matter in the system (see in Fig. 1.1). For many dielectric materials, P is proportional to the electric field strength E through the relationship:

$$P = \varepsilon_0 \chi_e E \quad (1.3)$$

This leads to

$$D = \varepsilon_0 (1 + \chi_e) E = \varepsilon_0 \varepsilon_r E \quad (1.4)$$

Here χ_e: electrical susceptibility

ε_r: relative permittivity (or dielectric constant)

Dielectric materials are characterized by a high dielectric constant, which is always greater than unity and represents the increase in charge storing capacity by insertion of a dielectric medium between two plates of the capacitor.

The capacitance C of the capacitor is a measure of this charge and is defined by

$$C = \frac{\varepsilon_0 A}{d} \quad (1.5)$$

where A is the area of the parallel plates and d is the distance of separation between them and ε_0 (8.854×10^{-12} F/m) is the permittivity of the free space. If a dielectric material is inserted

between the plates, the charge on the plates increase due to polarization in the material. The capacitance is now given by

$$C = \frac{\varepsilon_r \varepsilon_0 A}{d} \tag{1.6}$$

ε_r is a relative permittivity of the dielectric material.

In general, the polarization of dielectric material results from the four contributions shown in Fig. 1.2:

$$P = P_e + P_i + P_o + P_s \tag{1.7}$$

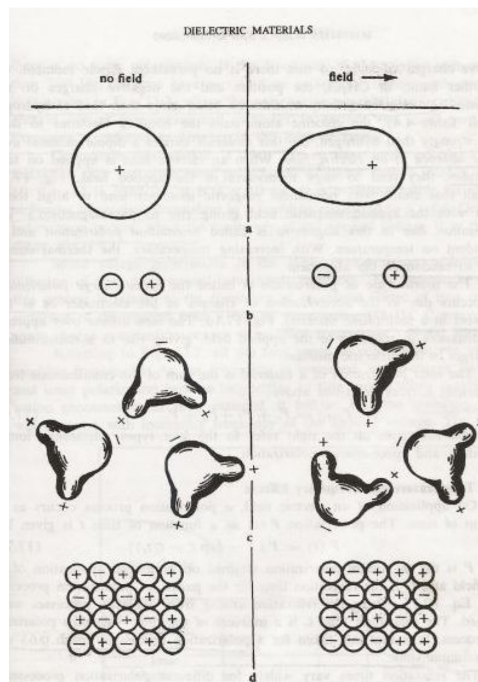

Fig. 1.2 Various polarization processes [1] (a) electronic polarization (b) ionic polarization, (c) orientation polarization, and (d) space charge polarization

The first one is the electronic polarization, P_e, which arises from a displacement of the centre of the negatively charged electron cloud relative to the positive nucleus of an atom by the electric field. The resonance of the electronic polarization is around 10^{15} Hz, it can be investigated through optical methods. The second one is the ionic polarization, P_i, which

originates from the relative displacement or separation of cations and anions from each other in an ionic solid, and their resonance is in the infrared region of 10^{12}-10^{13} Hz. The third contribution is the orientation polarization, P_o, which is found only in materials with permanent dipole moments. This polarization is generated by a rotation of the permanent moment in the direction of the applied electric field. The polarization due to the orientation of electric dipoles takes place in the frequency range from mHz, in the case of reorientation of polar ligands of polymers up to a few GHz in liquids such as water. The last one, P_s, is the space charge polarization. This type of polarization results from the build-up of charges at interfaces of heterogeneous systems. Depending on the local conductivity, the space charge polarization might be occurring over a wide frequency range from mHz up to MHz. As shown in Fig. 1.3 the different polarization mechanisms not only take place on different time scales but also exhibit different frequency dependence.

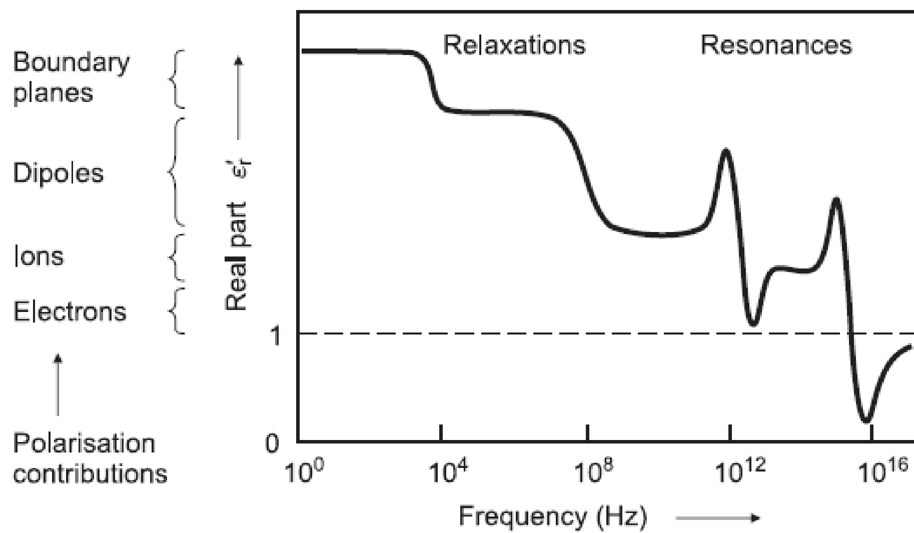

Fig.1.3 Frequency dependent relative dielectric constant [2]

The relative dielectric permittivity is written as a complex function:

$$\varepsilon_{r^*} = \varepsilon_{r'} - i\varepsilon_{r}'' \qquad (1.8)$$

the real part ε_r' characterizes the displacement of the charges, and the imaginary part ε_r'' the dielectric losses.

The loss tangent is defined as

$$\tan\delta = \frac{\varepsilon_r''}{\varepsilon_r'} \qquad (1.9)$$

The frequency-dependent contribution to the permittivity is schematically shown in Fig. 1.3.

For microwave ceramics frequently a quality factor Q is quoted:

$$Q = \frac{1}{\tan\delta} \qquad (1.10)$$

Dielectric ceramics and polymers are used as insulators. Dielectric materials for capacitors must have a high dielectric constant, low dielectric loss, high electrical breakdown strength, low leakage currents, etc.

The highest dielectric constants so far have been observed in some dielectrics as e.g. strontium titatate ($SrTiO_3$, STO) and ferroelectric perovskite ceramics, among which typical examples are barium titanate ($BaTiO_3$, BTO), barium strontium titanate ($(Ba,Sr)TiO_3$, BST), lead titanate ($PbTiO_3$, PT), lead zirconate titanate ($Pb,(Zr,Ti)O_3$, PZT), strontium bismuth tantalite ($SrBi_2Ta_2O_9$, SBT), strontium bismuth niobate ($SrBi_2Nb_2O_9$, SBN), and anti-ferroelectric materials like lead zirconate (PZ).

1.2 Ferroelectrics

Ferroelectric materials exhibit a wide variety of physical properties such as relative permittivity, piezoelectricity, pyroelectricity, electrostriction and electro-optical activity. These properties boost interest to study then in depth in science and technology, and they have an important commercial market. They have applications including multilayer capacitors, sensors and actuators, radiation detectors, optical waveguides and microwave devices [3,4]. Since miniaturization of electronic devices became more important in major applications, like

nonvolatile ferroelectric random access memories (NVFRAM) [5], dynamic random access memories (DRAM) [6], and micro electromechanical systems (MEMS) [7].

1.2.1 Ferroelectricity

(Source: Ref. 2)

Ferroelectric materials are dielectric materials characterized by a reversible spontaneous polarization, which exhibits an electric dipole moment even in the absence of an external electric field. In the ferroelectric state the center of the positive charge of the ferroelectric material unit cell does not coincide with the center of the negative charge. The polarization behavior in an electric field is highly non-linear and exhibits a hysteresis loop (*P-E* loop), as shown in Fig. 1.4. The hysteresis loop is characterized by two important parameters, including the coercive field E_c (or coercivity) and the remnant polarization P_r (or remanance). The coercivity is the field required to reduce the polarization P to zero, the remanance is the polarization at zero applied field. The value obtained by extrapolating the polarization in the high field region to zero is called the saturation polarization P_s.

In the case of an ideal crystal, the polarization versus field behavior, *P-E*, can be explained by a simple superposition of two contributions: (a) the (non-ferroelectric) dielectric ionic and electronic polarization, (b) spontaneous polarization, which is reoriented when the electric field E applied opposite to the polarization exceeds the coercive field E_c leading to the unidirectional jumps in the *P-E* curve shown in Fig 1.4 in a dotted line.

In polydomain ferroelectric materials, initially there is a statistical distribution of domains before it is polarized for the first time. Then the relation between the polarization P and the electric field E is characterized by the graph AB in Fig 1.4 in full line, starting with polarization $P=0$, P increases with increasing field until it reaches saturation at point B. The saturation polarization P_s is obtained by extrapolating the graph BC to $E=0$. If after saturation one now reduces the electric field again then at $E=0$ a remnant polarization P_R is found. P_R relates to the domain structure in the material. In order to bring the polarization to zero, a negative electric field (the coercive field E_c) has to be applied. If the negative field is further increased, then the hysteresis loop is followed in the reverse sense.

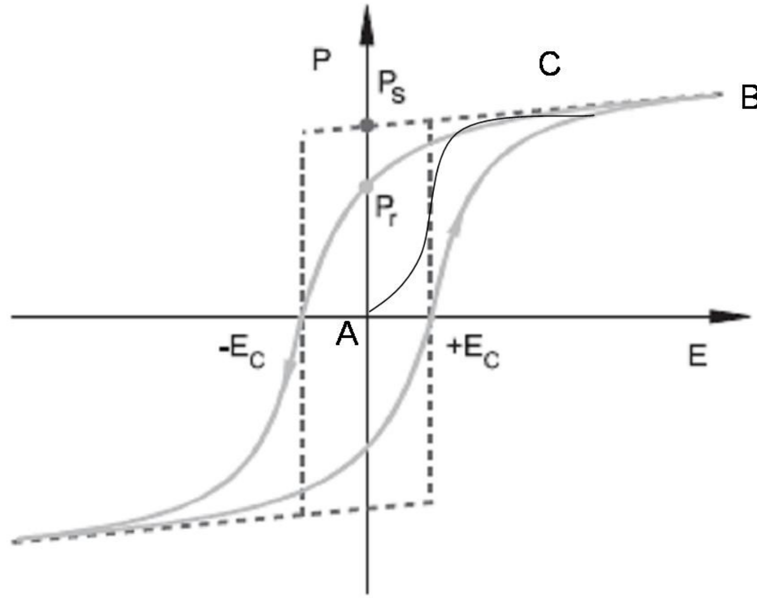

Fig.1.4 Ferroelectric hysteresis: polarization, *P,* as a function of the Electric field, *E*, dashed line single domain single crystal, full line polycrystalline.

In $BaTiO_3$ the dipole moment is caused by the displacement of either the Ti^{4+} or Ba^{2+} cations relative to the centre of the oxygen octahedron around the cation. The two-stable off-center positions correspond to the two different orientations of dipole moment. Adjacent dipoles tend to orient themselves in the same direction, which induces a spontaneous polarization. Regions of uniform polarization are called domains, separated by domain walls. In ferroelectric materials, the domain walls are extremely narrow, often not more than one or two lattice layers. In the absence of an electric field, the domains are randomly distributed, resulting in a net zero polarization. In an electric field, the domains tend to align in the field direction by movement of the domain walls and rotation of the dipoles and the polarization reaches the maximum value P_s. When the electric field is removed, domains cannot return to their original states, yielding a non-zero polarization P_r.

Different from normal dielectrics, in ferroelectrics the dielectric constant is a non-linear function of applied field, and can be evaluated from the derivative of the polarization to the applied field. Basically, there are two contributions to the dielectric constant: the intrinsic

component, which involves the switching of the dipole configurations, and the extrinsic component, which involves the domain wall motion [8,9].

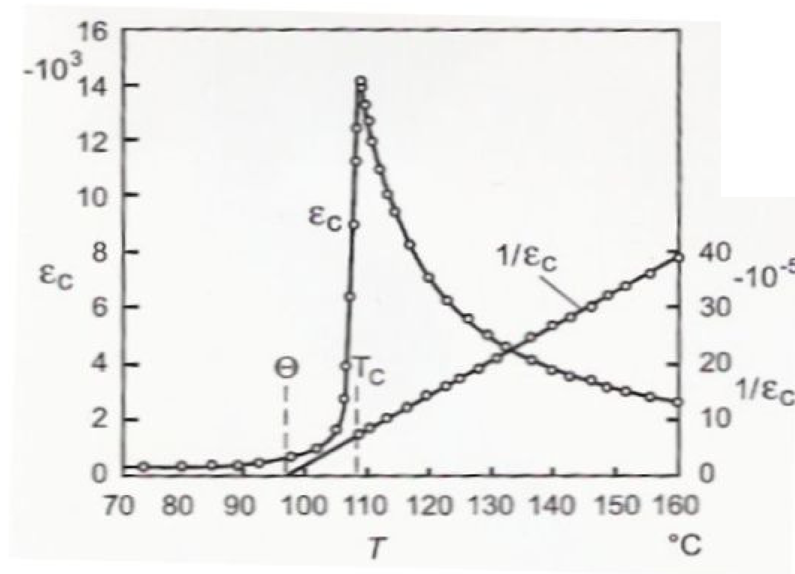

Fig. 1.5 Barium titanate phase transition [2]

A necessary condition for a crystal to exhibit ferroelectricity is that the crystal structure is non-centrosymmetric. The ferroelectric state is usually a low temperature condition, associated with the non-centrosymmetric phase. A structural phase transition from non-centrosymmetric to centrosymmetric upon heating induces a transition from the ferroelectric to the paraelectric state. The temperature at which this transition takes place is called the Curie temperature, denoted by T_c. At T_c dielectric constant (ε_r) exhibits a maximum, can be seen in Fig.1.5.

Above T_c (in cubic), the relationship between ε and the temperature follows the Curie-Weiss law:

$$\varepsilon = \frac{C}{T - \Theta} \tag{1.11}$$

Where C is the Curie constant and Θ *is* the Curie-Weiss temperature, which in most cases equal to or slightly different from T_c.

1.2.1.1 Barium Titanate ($BaTiO_3$, BTO):

Among the different ferroelectrics, oxides showing a perovskite structure or a related structure are of particular interest. Fig. 1.6 (a) displays the crystal structure of barium titanate, often regarded as the archetypical structure of the ferroelectric. In the cubic high temperature phase this material does not show any spontaneous polarization and, hence the system is paraelectric. Upon cooling below the Curie temperature (T_c<120°C), a phase transition occurs during which positive and negative metal ions displace with respect to each other, leading to a tetragonal deformation. Due to the asymmetry in the unit cell by the displacement, a spontaneous polarization in the direction of the axis of tetragonal appears. The abrupt change of spontaneous polarization of ΔP_s=0.18 C/m^2 [Waser et al.] at the cubic to tetragonal phase transition ($T<T_c$) clearly demonstrate the first order phase transition.

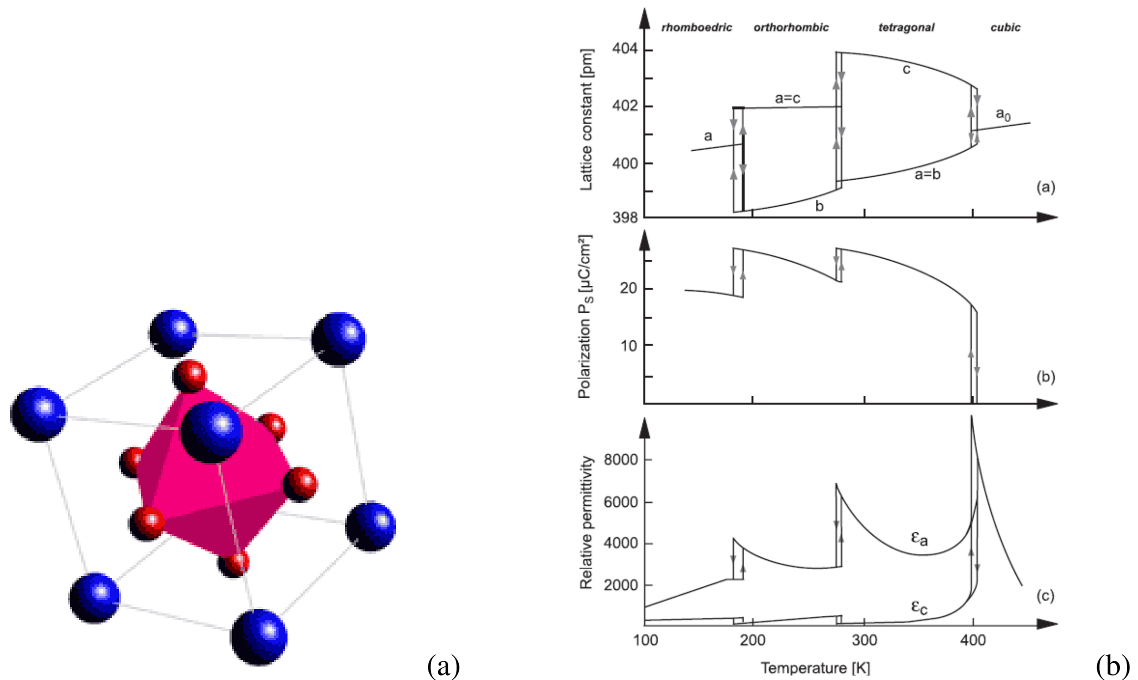

Fig. 1.6 (a) Barium titanate crystal structure with octahedral (b) BTO phase transitions with respective to temperature and their other properties [2].

BTO has another two phase transitions, the second phase transition transforms from tetragonal to orthorhombic structure at 5°C, and then finally, at -90°C the orthorhombic deforms into rhombohedral structure, can be seen all $BaTiO_3$ structural changes and their properties in Fig. 1.6 (b).

From the crystal chemical perspective, this series of phase transitions can be viewed as a consequence of the Ti $^{+4}$ ions being somewhat too small to occupy the interstice created by the Ba-O framework. As a result, the series of phase transforms takes place to reduce the Ti cavity size, in Fig. 1.7 can see the experimental results of the phase transitions of the $BaTiO_3$ ceramic.

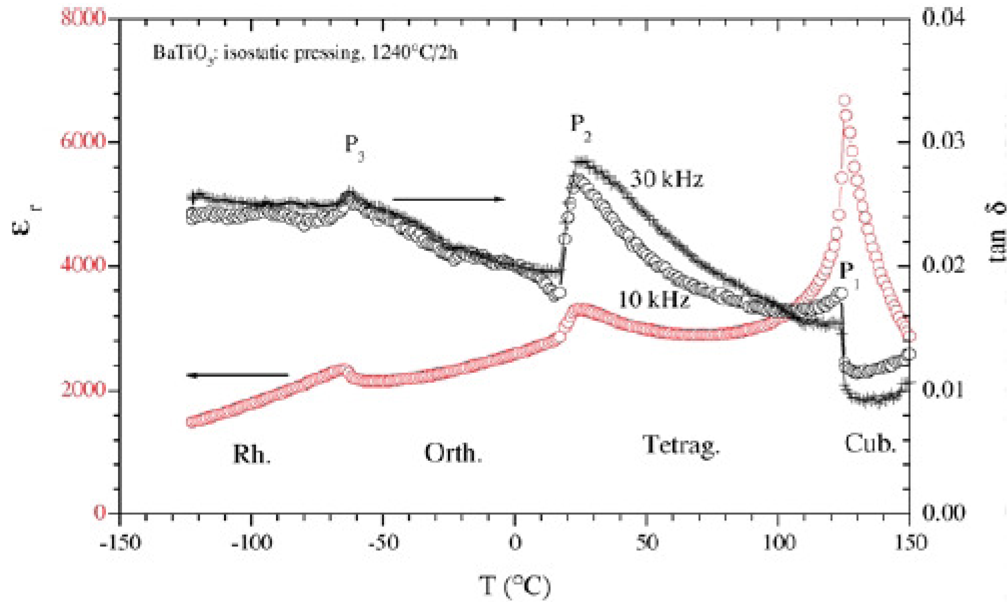

Fig. 1.7 Relative dielectric constant (ε_r) and dielectric loss (Tan δ) of $BaTiO_3$ ceramic [10]

Certainly, the radii of the ions involved impact the propensity for forming ferroelectric phases; thus both $PbTiO_3$ and $BaTiO_3$ have ferroelectric phases, while $CaTiO_3$ and $SrTiO_3$ do not.

1.2.1.2 Strontium Titanate ($SrTiO_3$, STO):

STO is the best characterized complex oxide. It is a prototypical soft-mode incipient ferroelectric [11] with a perovskite structure. At low temperatures, STO shows a non-linear, electric field tunable dielectric permittivity, which is of interest for the tunable microwave devices operating at cryogenic temperatures. In addition to their practical importance, STO film that represent a good model system for paraelectric, tunable dielectric thin films.

Bulk STO has cubic symmetry between room temperature and ~ 150 K. Below this ~ 150 K, it undergoes a structural (but not a ferroelectric) transition to a tetragonal phase. Above the transition temperature, the temperature (*T*) dependence of the dielectric susceptibility χ of bulk STO follows the classical Curie-Weiss type behavior described by the equation (1.11).

1.2.1.3 Barium Strontium Titanate ($(Ba_x, Sr_{1-x})TiO_3$, BST):

Ferroelectric films for tunable microwave devices are used in their paraelectric phase, because of the high dielectric losses and hysteresis in the ferroelectric phase due to the motion of domain walls. One of such widely studying material is BST.

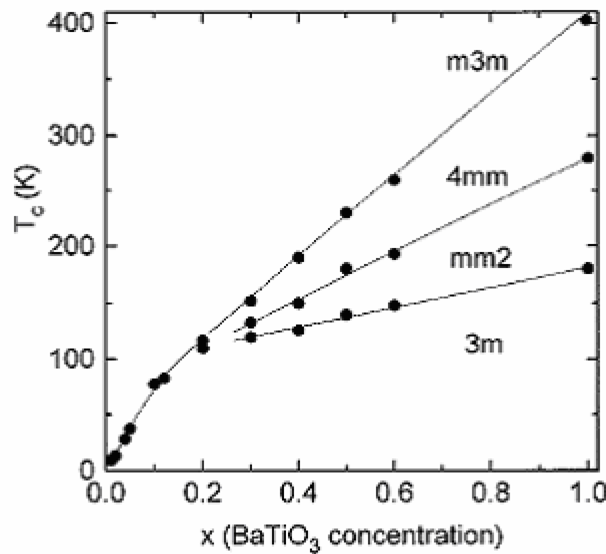

Fig. 1.8 Phase diagram of $Ba_xSr_{1-x}TiO_3$ [12]

BST is a mixed oxide of the perovskite with ABO_3 type structure and is one of the most promising candidates with different compositional grades of BTO and STO. With higher Sr^{+2} composition in BST films, T_c can go to cryogenic temperatures as the Sr^{+2} has very small atomic radius, and then ultimately the unit cell shrinks in Fig. 1.8 shown the phase diagram of the $Ba_xSr_{1-x}TiO_3$. It does not show ferroelectric hysteresis as a thin film on a Si substrate because (a) the solid solution of Sr^{+2} the A site of the Ba^{+2} shifts the Curie point to lower temperatures and (b) its stress condition also influence the BST properties, if its thermal expansion is larger than that of Si. The properties of the BST films depend on the concentration of the Ba^{+2} and Sr^{+2} ratio and conditions of

the deposition and recrystallization treatment. Phase transitions of the different compositional $Ba_xSr_{1-x}TiO_3$ films can be seen in Fig. 1.9.

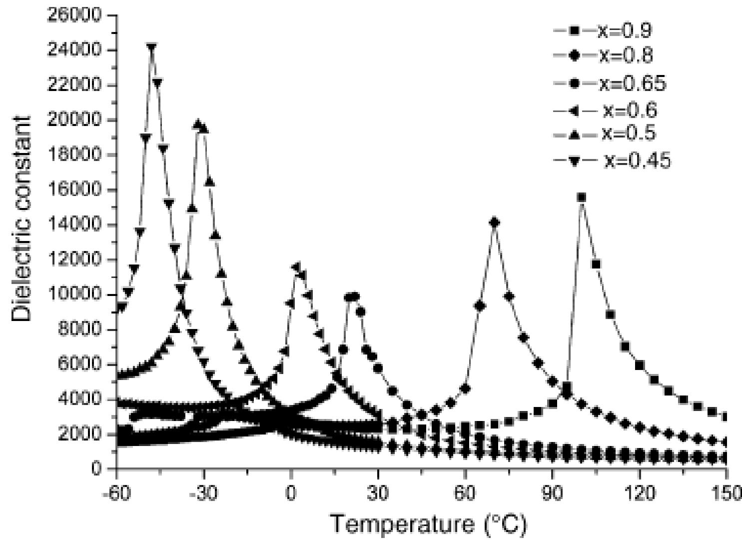

Fig. 1.9 Phase transitions for different compositional $Ba_xSr_{1-x}TiO_3$ [13]

1.2.2 Other important properties of ferroelectrics

Anti-ferroelectricity: Anti-ferroelectric materials belong to one class of deformation in the ferroelectric crystals, which has neighboring lines of ions displaced in opposite directions. The energy difference between anti-ferroelectric and ferroelectric states are very small, therefore a large applied field can switch the crystal from the former to the latter.

Electro-optic effect: By varying the ferroelectric polarization with an electric field, one produces a change in the optical properties of the ferroelectrics. The most important effect are the quadratic electro-optic (E-O) effect and the biased quadratic electro-optic (E-O) effect [14].

Pyroelectricity: This property relates to the ability to produce electric charges perpendicularly to the polar axis on the crystal faces as a result of a temperature change. However, since the spontaneous polarization, P_S, is temperature dependent, any temperature change ΔT at rate larger than the screening process will lead to uncompensated polarization charges

$$\Delta P = P_{PY}\Delta T \qquad (1.12)$$

Where P_{PY} is the pyroelectric coefficient

Piezoelectricity: All polar crystals shows piezoelectricity, since any stress T will result in a strain S because of the elastic properties of the material. Strain will affect the polarization; for polarization is caused by a displacement of the charge centers of the anions and cations. For small changes of the stress T, the relation

$$P = d \cdot T \tag{1.13}$$

Where P is called direct *piezoelectric effect*, d is called *piezoelectric coefficient*.

Ferroelasticity: A crystal that has two or more stable orientational states and can be switched from one to the other with an external mechanical stress is called ferroelastic.

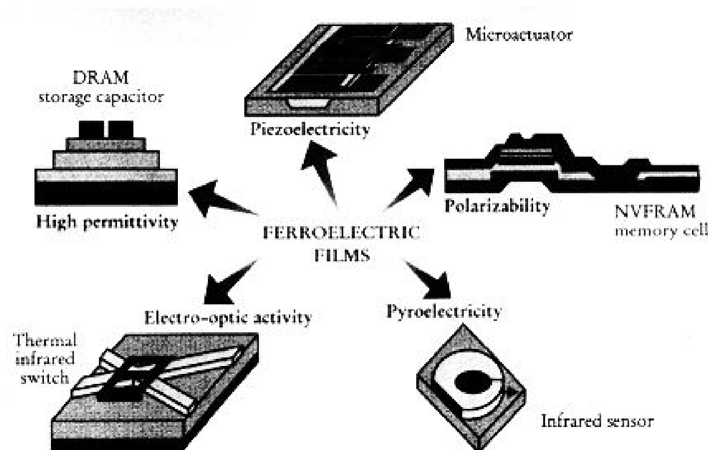

Fig. 1.10 Applications of ferroelectric materials [15]

Various potential applications of ferroelectric materials in commercial devices, exploiting their special properties are presented in Fig. 1.10. These include high-dielectric constant storage capacitors, piezoelectric micro-actuators, infrared sensors, electro-optic light valves and thin film memories.

1.2.3 Alternative structural oxides

An alternative structure that has also been widely investigated both for high temperature piezoelectric, as well as for ferroelectric memory applications is the bismuth layer structure family. Such materials as $SrBi_2Ta_2O_9$, $SrBi_2NbTaO_9$ and $SrBi_2Ti_4O_{15}$, have been explored [16]. Their general chemical formulas are represented as $ABi_2B_2O_9$ and $ABi_2B_4O_{15}$, where A is a divalent metal such as Sr, Ba or Pb, B a metal of valence +5, usually Nb for the former, and of valence +4, usually Ti, for the latter. The layered structure of this kind of material is shown in Fig. 1.11. These materials have demonstrated a high endurance during electrical cycling with excellent improved fatigue-free properties up to 10^{12} switching cycles. This very good fatigue behavior is believed to be due to the oxygen-rich bismuth layer preventing degradation of the polarization.

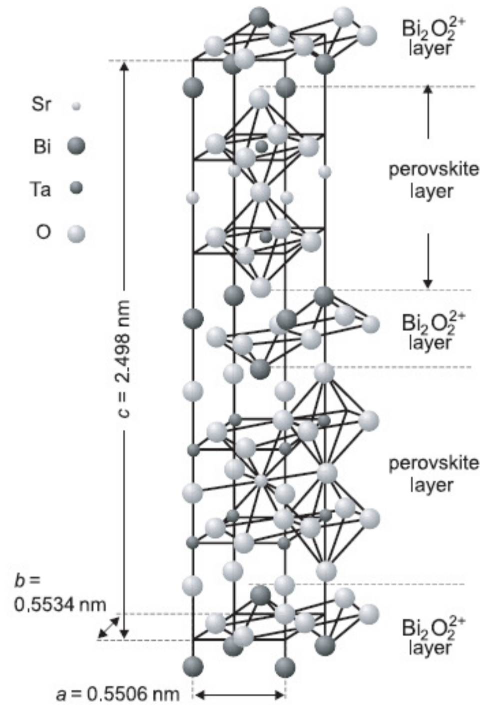

Fig. 1.11 Bismuth layer structure $SrBi_2Ta_2O_9$ [2]

$Pb(MgNb)O_3$ (PMN) is best known as a “relaxor” ferroelectric with a partially ordered perovskite structure [17]. Very large dielectric constants (> 25000) and electrostriction coefficients are observed in a broad range of temperature. The dielectric constant drops rapidly with frequency (hence, it is named a “relaxor”) because it takes time for the polarization fluctuations to respond. As

"relaxaor" ferroelectrics, PMN-based materials have found to be the most successful application as high-strain electrostrictive actuators and high dielectric constant capacitors. However, PMN ceramics are somewhat difficult to prepare. In Table 1.1 important ferroelectric materials are listed.

Material	**Chemical formula**	T_c **[K]**
Ammonium dihydrogen phosphate (KDP)	$NH_4H_2PO_4$	148
Barium titanate	$BaTiO_3$	393
Boracite	$Mg_3B7O_{13}Cl$	538
Germanium tellurium	GeTe	673
Lead titanate	$PbTiO_3$	763
Lead zirconate	$PbZrO_3$	503
Lead zermanate	$Pb_5Ge_3O_{11}$	453
Lithium niobate	$LiNbO_3$	1473
Lithium tantalate	$LiTaO_3$	938
Potassium dihydrogen phosphate (KDP)	KH_2PO_4	123
Rochelle salt	$NaKC_4H_4O_6.\ 4H_2O$	255, 297
Strontium bismuth tantalite	$SrBi_2Ta_2O_9$	843
Sodium Niobate	$NaNbO_3$	73, 627
Sodium nitrite	$NaNO_2$	437
Triglycine sulfate (TGS)	$(NH_2CH_2COOH)_3.H_2SO_4$	322

Table 1.1 Important ferroelectric materials

1.3 Literature review of thin films

It is interesting to review the literature on deposition techniques and the properties of the thin films which depend on the deposition parameters. There are several deposition techniques being exploited for the growth of ferroelectric and RuO_2 thin films.

1.3.1 Perovskite materials

It is interesting to review the literature on deposition techniques and the properties of the perovskite materials which depend on the deposition parameters. There are several deposition techniques being exploited for the growth of ferroelectric thin films. The ferroelectric thin films are used in electronic, electro-optic, and microwave device applications due to high permittivity and larger polarization associated with ferroelectric phenomena. For these applications it is important to have high-quality epitaxial thin films with smooth surfaces. Many chemical (no bombardment with energy ions), electrochemical, and physical methods (bombardment with low energy ions) were used for the deposition and growth of ferroelectric thin films.

The growth process with low energy ion bombardment includes magnetron sputtering [18], ion-beam sputtering [19], excimer laser ablation [20], electron cyclotron resonance (ECR) plasma assisted growth [21] and plasma- enhanced chemical vapor deposition (PECVD) [22]. The techniques that do not involve bombardment include sol-gel [23], metal-organic decomposition (MOD) [24], thermal and e-beam evaporations [25], flash evaporation [26], chemical vapor deposition (CVD) [27], metal-organic chemical vapor deposition (MOCVD) [28] and molecular beam epitaxy (MBE) [29].

Some results regarding the correlation between the deposition parameters and the properties of BTO film were presented by some researchers. For e.g., Kim et al. [30] and Ukino et al. [31] described the dependence of amorphous, cubic, and tetragonal phase transitions on the substrate and annealing temperatures of BTO thin films prepared by rf magnetron sputtering and they observed that on MgO and Si substrates, BTO films deposited below 450 and 500°C were amorphous, respectively. Above these temperatures the films were crystalline with the cubic phase. Mansingh et al. [32] studied the effect of the target on the structure of the BTO thin films. Desu et al. [33,34] studied the relationship between the film deposition process, stress, and the ferroelectric properties of BTO thin films by rf magnetron sputtering.

Taylor et al. [35] reported that oxygen partial pressure and total chamber pressure influence the dielectric permittivity, dielectric quality factor, and lattice parameters of STO films deposited by rf magnetron sputtering. The dielectric constant is very high and largest quality factor observed at 3.3 Pa pressure. With increasing the total pressure lattice constant was increasing from a = 3.929 Å at 3.3 Pa to a = 3.933 Å at 10 Pa.

Wang et al. [36] deposited nano-crystalline STO and observed that increasing with film thickness the crystallite size increases. The dielectric constant of STO films decreases with decreasing film thickness by changing the temperature, frequency and the bias voltage.

The efforts by researchers continue to achieve ferroelectric thin films of good quality from a single target oxide target, and the recent activity was related to the solid solution of BTO-STO. Good quality of BST thin films were reported by single target sputtering. For example, Hwang et al. [37] and Zafar et al. [38] reported on sputter-deposited stoichiometric BST thin films that posses useful device-related electrical property.

Rf magnetron sputtering technique always been the first growth attempted for the growth of ferroelectric thin films, as it has respected industrial track record and is characterized by high producibility in the chemical composition, easy process control, and compositional change of the film by using the multiple elemental target (Ba, Sr, Ti etc.,) or multiple components ($BaTiO_3$ and/or $SrTiO_3$).

Nakata et al. [39] observed interesting properties of deposition parameters and film properties of BTO thin films. They deposited BTO thin films on MgO substrates by pulsed laser deposition (PLD) in an oxygen atmosphere of 0 to 66.66 Pa and at higher substrate temperatures of 800 and 850°C, they observed that at higher oxygen pressures the lattice parameters decreased. Similar results were observed for $Ba_xSr_{1-x}TiO_3$ thin films by Tseng et al. [40] by PLD on Si substrates. The surface morphology was also greatly influenced by the oxygen partial pressure. The BTO thin films surface was relatively smoother at 1.33 Pa and also the grain sizes were larger at higher oxygen pressures.

Epitaxial BTO thin films were deposited by PLD on MgO (001) substrates by Norton et al. [41,42], they observed that BTO thin films were *c*-axis oriented and perpendicular to the substrate interface plane. It has been shown that the microstructure of the films can be varied by changing the deposition parameters. Optimizing these parameters permits the formation of thin films with controlled microstructures and properties.

Kim et al. [43] observed the relationship between the structure and microwave properties of $Ba_{0.5}Sr_{0.5}TiO_3$ thin films deposited by PLD onto MgO (100) substrate. The dielectric constant of BST thin films at 10 GHz increases after a post-deposition annealing. For annealing temperatures above 900°C, the dielectric constant of the annealed films increases with increasing tetragonal distortion. This result indicates that the larger in-plane lattice parameter provides the larger ionic displacement along the in-plane direction, resulting in a larger dielectric constant.

PLD technique offers many advantages for film growth, including epitaxial or crystalline growth at low substrate temperatures, congruent deposition of materials with complex stoichiometric and deposition of materials with high melting points and ability to form meta-stable micro-structures.

Ren et al. [44] grew $Ba_xSr_{1-x}TiO_3$ thin films by the sol-gel method by using barium acetate ($Ba(C_2H_3O_2)_2$), strontium acetate ($Sr(C_2H_3O_2)_{21}2H_2O$) and titanium isopropoxide ($Ti(C_3H_7O)_4$) in acetic acid (CH_3COOH) and ethylene glycol ($HOCH_2CH_2OH$) with appropriate stoichiometric, and obtained good crystalline and smooth films by rapid thermal annealing (RTA). They observed that microstructure and electrical properties of the BST thin films can be affected by the substrate and the annealing process. Dielectric constant and dielectric loss of the BST films at 100 kHz are 230 and 0.02, respectively. Leakage current density of the BST capacitors was $1.6X10^{-7}$ Acm^{-2} at 3 V.

Sharma et al. [45] prepared BTO thin films by the sol-gel process, using barium acetate and titanium (IV) isopropoxide precursors. The as-deposited films were amorphous. After annealing at 700°C in air for one hour, the films became crystallized and had tetragonal phase. The dielectric constant of BTO thin films at 1 kHz was 370 and T_c was observed at 125°C.

Sol-gel growth technology is used as a method for depositing high quality multi-component oxide thin film, where the processing technology needs to be rapid and inexpensive.

A good discussion of precursor preparation and subsequent delivery in a reaction zone of a MOCVD reactor has been detailed in a recent review [Ann. Rev. Mat. Sci. 25-525], which describes the growth of BTO, STO, and BST thin films. CVD and MOCVD techniques have potential advantages, including the ability to deposit high-quality, ultra-thin layers on three dimensional (3D) complex geometries, excellent composition control, and amenability to large-scale processing

1.3.2 Properties of RuO_2

Ruthenium dioxide (RuO_2) is the most investigated and well known oxide electrode candidate for capacitor applications. RuO_2 belongs to the family of transition-metal oxide compounds with tetragonal rutile structure (can be see in Fig. 1.12) with $P4_2/mnm$ symmetry, space group number 136, $a = b = 4.4902$ Å, $c = 3.1059$ Å, the unit cell volume is 62.62 Å^3, with various interesting properties such as low resistivity, high thermal and chemical stability, and high chemical corrosion resistivity. RuO_2 thin films are promising electrode for high dielectric ferroelectric materials, as it reduce the fatigue property in the electronic devices. Because RuO_2 reduces the lattice mismatch and work function difference at the electrode and ferroelectric film interface, therefore, defect entrapment and the loss of polarization reduced, ultimately the fatigue life is improved.

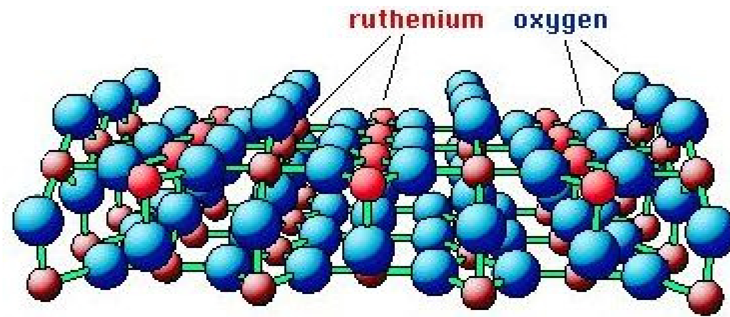

Fig. 1.12 Rutile structure of RuO_2 [46]

RuO_2 thin films have been successfully prepared to date by rf sputtering, metal organic chemical vapor deposition (MOCVD), pulsed laser deposition (PLD), and solution technique.

Kang et al. [47] deposited RuO_2 films on Si substrates by rf magnetron sputtering, and observed that RuO_2 films deposited at the low substrate temperature (100°C) showed (110) closed packed oriented grains with relatively low internal strain (0.8%), on the other hand films deposited at 300°C and annealed to 800°C in air showed randomly oriented grains with high internal strain (1.4%) and the grains transformed to mountain like, three dimensional islands. It is very clear that annealing transform the films from closed packed to the three dimensional islands, with the effect of high internal strain and high surface energy.

Kaga et al. [48] deposited RuO_2 thin films by rf reactive sputtering, and studied the effect of substrate temperature and reactive gases ($Ar+O_2$) and O_2. They observed that, in the 18-28% O_2 flow region, the deposition rate was around 28 nm/min, and it was good crystalline and with (110) oriented grains. At 32% flow region, the deposition rate was decreased to 8 nm/min and the films were (101) oriented. Above 32% O_2 region films were almost amorphous. Resistivity of the RuO_2 films decreased with increase of the substrate temperature and a minimum resistivity of 42 μΩcm was obtained at 500°C with 20% O_2 flow.

1.4 The radio-frequency (rf) magnetron sputtering method

The sputtering technique is the most versatile method for perovskite materials, to deposit thin films up to the atomic scale. It is always been the first growth attempted for the deposition of ferroelectric thin films, as it has a respected industrial record. In this work, we used to deposit our perovskite and electrode thin film materials by rf magnetron sputtering. It is worthy to discuss the mechanism of rf magnetron sputtering.

1.4.1 Sputtering process mechanism

The sputter process mechanism is illustrated clearly in Fig 1.13. The incident ion, which has been accelerated within the chamber with nearly the full voltage applied of 50 to 1000 V, hits the surface atoms (target material). The following collision cascade leads to a heating of the target and finally some of sputtered atoms which can leave the surface. The threshold energy for sputtering is much higher than the surface binding energy, W_b, of the atoms which is of the order of 4 to 8 eV. This difference can be directly understood as several collisions are necessary in order to obtain an atom in the backward direction. Hence, the threshold is observed at 4 W_b to 8 W_b corresponding to threshold energy of 20 to 50 eV. A linear increase is observed for many conditions up to voltages of 1000 eV. At higher energies the ions penetrate too deeply into the target and the sputter yield decreases again.

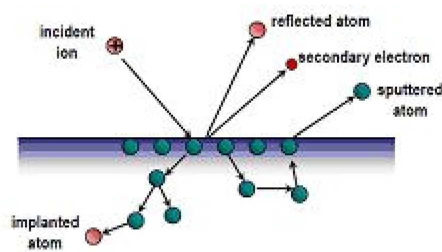

Fig. 1.13 Sputtering mechanism

1.4.2 Magnetron sputtering

An ionization degree of less than 1% of the atoms is characteristic of plasma and consequently a rather low sputter rate. To improve the ionization rate magnetic fields can be used

which force the electron onto helical paths close to the cathode and yield a much higher ionization probability [49,50]. This magnetron arrangement additionally allows a lower gas pressure. However, it has the disadvantage of more inhomogeneous target erosion than a simple planar geometry.

1.4.3 Radio frequency (rf) magnetron sputtering

Direct current (DC) sputtering works very well for conductive target materials. For insulating target materials, DC sputtering does not work, because of the charge accumulation of electric load at the target surface. To overcome this problem, a high-frequency plasma discharge must be applied in order to avoid the charge accumulation at the target surface. A typical frequency of 13.56 MHz is capacitively coupled to the target and there is only small voltage decay across the electrode as shown in Fig. 1.14.

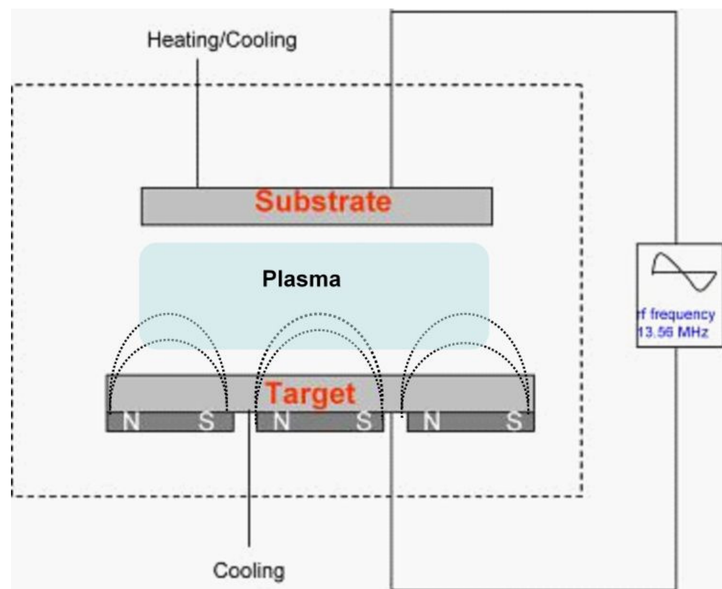

Fig. 1.14 Capacitively coupled rf magnetron sputter target

As the electrons are much faster than the ions, a negative potential at the electrodes as compared to the plasma potential evolves during each cycle. With a symmetrical arrangement of cathode and anode we would obtain similar re-sputtering rates and no film growth. However, non-symmetries, which yield some bias voltages, are introduced by the coupling of the rf and by differences in the geometry, i.e., different sizes of target and substrate, and especially by the generally applied

grounding of the substrate and the deposition chamber. However, deposition rates are much lower than DC sputtering.

1.5 Structure zone model

The pressure of the sputtering gas plays crucial role in film growth, and it is an additional and important process parameter which must be considered and optimized. The sputter gas pressure influences the mean free path of the atoms and therefore their energy, angular distribution and finally also their incorporation in the film. For metals, the famous zone model for the film growth has been developed by Thornton [51], which shows some systematic influences of the following parameters, can be seen in Fig. 1.15.

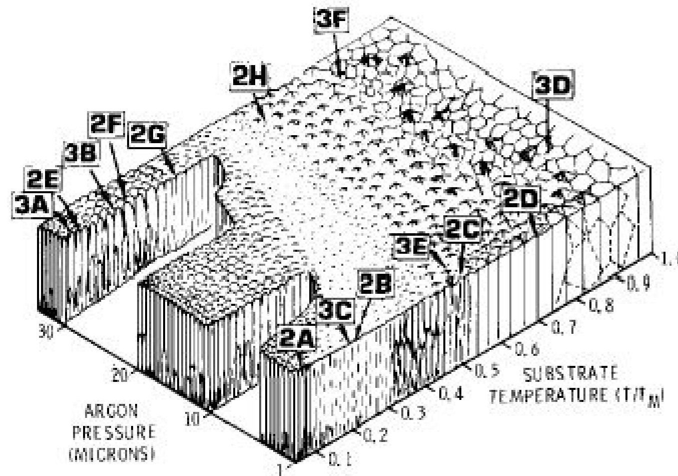

Fig. 1.15 Structure zone model diagram for sputter deposited metals [51]

Zone 1: Ts < 0.2 T/T_m: at lower temperatures no bulk diffusion and only very limited surface diffusion is observed which would allow for crystallite rearrangement. The size of the fibers increases with temperature mainly following temperature dependence of the nucleation density.

Zone Ts: (0.2-0.3 T/T_m): In this transition zone, surface diffusion becomes effective and small crystals of energetically unfavorable orientation are eliminated, i.e., competitive texture is observed and grains are poorly defined fibrous grains without grossly voided boundaries.

Zone 2: (0.3-0.5 T/T_m): In this region, the growth process is dominated by adatom surface diffusion. The structure consists of columnar grains separated by distinct dense inter-crystalline boundaries.

Zone 3: (> 0.5 T/T_m): In this region, the bulk diffusion has a dominant influence on the texture of the crystal. Texture is determined by the lowest free energy surface of the crystal. Finally, the influence of the Ar pressure decreases.

1.6 Experimental equipment

In this work, all experiments were carried out in the sophisticated von Ardenne LS 500 S DC/RF magnetron sputtering machine (as shown in Fig. 1.16). Thin films of $BaTiO_3$ and RuO_2 single layers and $BaTiO_3$, $SrTiO_3$, $BaTiO_3/SrTiO_3$, $BaTiO_3$ /$Ba_{0.75}Sr_{0.25}TiO_3$ capacitor structure ($Si/SiO_2/RuO_2$/dielectric/RuO_2) were deposited by rf magnetron sputtering with the radio- frequency of 13.56 MHz. The generator power can be use up to the maximum of 600 W. The substrates can be heated up to 750°C with carbon radiator heaters with the help of a Eurotherm thermal controller. Inside the chamber there are two cathodes with the diameter of 150 and 90 mm, instead of 150 mm, another 90 mm cathode can be used (shown in Fig 1.15 (b)). Initially for all experiments we pump down the base pressure up to 3.5 X 10^{-5} mbar (3.5 mPa), we used pure Ar (99.999%), O_2 (99.999%) for sputtering, and N_2 (99.999%) for annealing and have separate gas controllers to control each gas flow. The whole system is connected through RS 232 S interface and controlled by computer. It is easy to execute the deposition procedure.

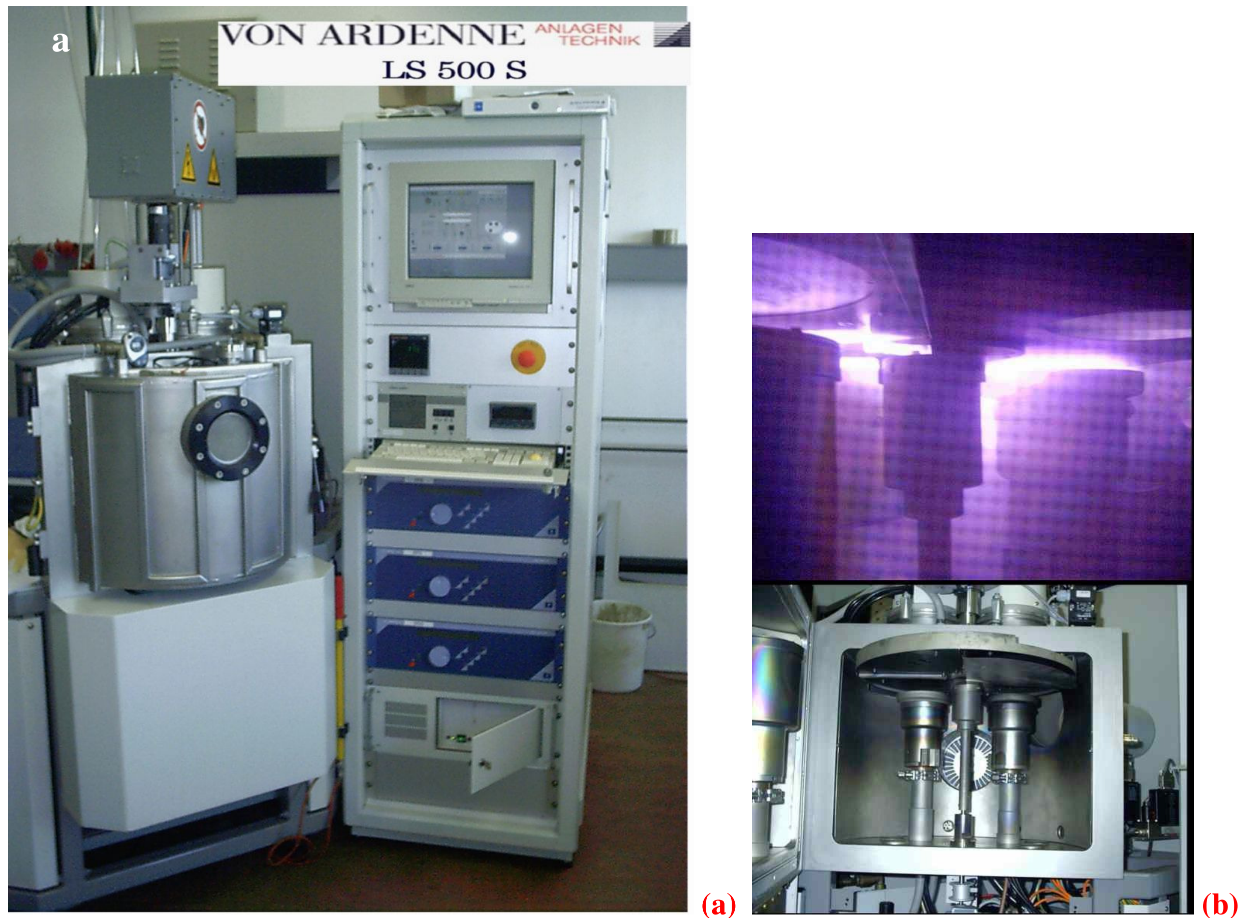

Fig. 1.16 (a) von Ardenne LS 500 S DC/RF magnetron sputter machine, (b) inside the sputter chamber and two sputter cathodes

1.7 Thin film capacitor structure

The capacitors were fabricated on Si/SiO_2 wafers, which were the diameter of 25 mm and 1 mm thick. The bottom RuO_2 electrodes were deposited on Si/SiO_2 wafers at 540°C and the top electrodes were deposited at room temperature in Ar (50 sccm) atmosphere with using stoichiometric RuO_2 target (90 mm). The dielectric films were deposited at different parameters, i.e. temperature, Ar/O_2, thickness etc., with different material stoichiometric targets of $BaTiO_3$, $SrTiO_3$ and $Ba_{0.75}Sr_{0.25}TiO_3$ with the diameter of 90 mm. The schematic diagram of the capacitor is illustrated in Fig. 1.17

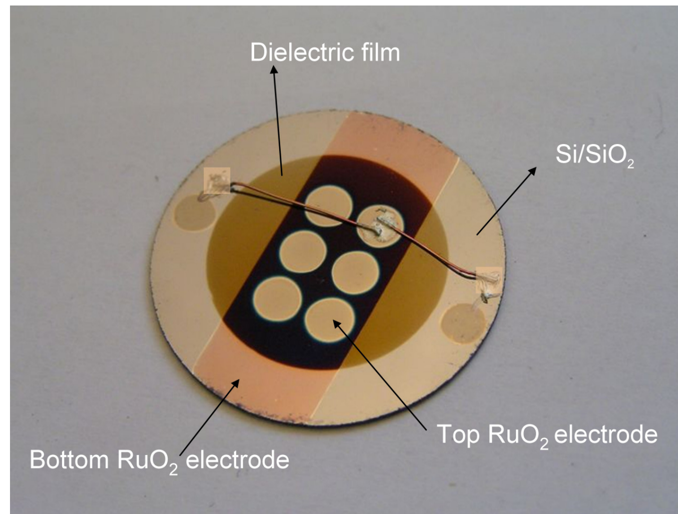

Fig. 1.17 Our capacitor structure.

1.8 Film characterization

The analytical techniques used for the characterization of thin films in this work are summarized in Table 1.2. More detailed information about the instrumentation details and the measurements can be found in the following chapters.

Technique	Characterization
IR spectrophotometer	Optical and thickness
X-ray diffraction (XRD)	Crystallinity and structure
AFM and SEM	Morphology and cross-section
RBS	Chemical composition
Impedance spectroscopy	Dielectric and electrical
Four-point probe	Resistivity
XRR	Density and thickness
Balance	Mass and density
Raman Spectroscopy	Structural and optical modes
Profilometer	Thickness
SCOUT 2 optical simulations	Optical constants
RBxN	Analyzing RBS spectra

Table 1.2 Analytical techniques and characterization of the thin films

Mass of the films is measured by weighing the film before and after the deposition in order to determine the film density and mass equivalent thickness with the balance. In order to obtain the optical properties (band gap, refractive index, etc.,) and thickness of the thin films, we measured UV-IR spectroscopy in the range of 200 to 2000 nm wavelength and simulated with SCOUT 2 simulation software. Thickness is measured with profilometer. Crystallinity and phase analysis was detected by X-ray diffraction (XRD) and for many films we normalized XRD raw data with respect to thickness, in order to understand the true nature of the film structure. Atomic force microscopy (AFM) and scanning electron microscopy (SEM) used to study the surface morphology and cross-section of the films. Resistivity is measured by using four-point probe method. X-ray reflectivity (XRR) is used to determine the thickness and density of the film for few samples in order to cross-check with other techniques results. Chemical composition of the films is determined by Rutherford Back Scattering (RBS) and the spectra were simulated by the RBxN simulation software. In order to correlate the structural results of the films with XRD, we measured the Raman spectroscopy. Depth profile is studied by means of Secondary Ion Mass Spectroscopy (SIMS). Impedance spectroscopy is employed to understand the dielectric and electrical properties of the thin film capacitors and discussed in detail in Appendix A.

1.9 Scope of the dissertation

In this dissertation, $BaTiO_3$ and $SrTiO_3$ thin film properties are systematically investigated. It concentrates on effects of substrate temperature, chamber pressure and film thickness. The basic idea of this study is to enhance the dielectric permittivity of $BaTiO_3$ and $SrTiO_3$ thin films by using RuO_2 as an electrode material, as these materials are promising candidates for many electronic applications.

This dissertation consists of eight chapters. Introduction of basic material properties (dielectric and ferroelectric), literature review and deposition methods are presented in Chapter 1.

In Chapter 2, optical and structural properties of $BaTiO_3$ thin films investigated by means of optical spectroscopy and x-ray diffraction methods are presented. The correlation of structural and optical properties is presented. These properties are very important in opto-electronic applications.

In Chapter 3, structural and electrical properties of the RuO_2 thin films are described. We attempted to understand the correlation of deposition and annealing effects with the electrical properties of RuO_2 thin films.

In Chapter 4 and 5, respectively, thin film capacitors of $SrTiO_3$ and $BaTiO_3$ with RuO_2 as an electrode material are investigated by means of impedance spectroscopy. Film thickness, deposition temperature and oxygen partial pressure has been varied in order to study their effects on dielectric properties. The impedance spectra are simulated with equivalent electrical circuits with parallel RC_p and RQ_p elements.

In Chapter 6, annealing effects on $Ba_{0.75}Sr_{0.25}TiO_3$ thin film capacitors are described.

In Chapter 7, heterostructures of $BaTiO_3/SrTiO_3$ and $BaTiO_3$/ $Ba_{0.75}Sr_{0.25}TiO_3$ thin film capacitors are described. These heterostructures have been deposited by changing the individual layer thickness. Their dielectric properties have been analyzed by means of impedance spectroscopy.

In Chapter 8, Summary is presented.

References

[1] V. Raghavan *Materials Science and Engineering*, Prentice Hall of India (Pvt) Ltd., New Delhi (1999)

[2] R. Waser *Nanoelectronics and Information technology: Advanced Electronic Materials and Novel Devices*, WILEY-VCH GmbH & Co. KGaA, Weinheim (2003)

[3] R.Ramesh, S. Agarwal and O. Auciello *Mater. Sci. Eng.* R **32** 191 (2001)

[4] M. Sayer and K. Sreenivas *Science* **247** 1056 (1990)

[5] J. F. Scott and C. A. Paz de Araujo *Science* **246** 1400 (1989)

[6] S. V. Kalinin and D. A. Bonnell *Appl. Phys. Lett.* **78** 1116 (2001)

[7] D. L. Polta *Microelectron. Eng.* **29** 51 (1995)

[8] N. B. Chaim, M. Brunstein, J. Grunberg and A. Seidman *J. Appl. Phys.* **45** 2398 (1974)

[9] F. Xu, S. Trolier, W. Ren and B. Xu *J. Appl. Phys*. **89** 1336 (2001)

[10] B. L. Cheng, M. Gabbay, M. Maglione and G. Fantozzi *J. Electroceramics* **10** 5 (2003)

[11] R. Waser and O. Lohse *Integrated Ferroelectrics* **21** 27 (1998)

[12] V. V. Lemanov, E. P. Smirnova, P. P. Syrniova, and E. A. Trarakanov *Phys. Rev. B*. **54** 3151 (1996)

[13] C. Fu, C. Yang, H. Chen, Y. Wang and L. Hu *Mater. Sci. Eng. B* **119** 185 (2005)

[14] G. H. Haertling *J. Am. Ceram. Soc*. **82** 797 (1999)

[15] O. Auciello, J.F. Scott and R. Ramesh *Physics Today* July 22 (1998)

[16] F. Jona *Ferroelectric crystals*, 1st edition, New York, Dover (1993)

[17] R. E. Newham *MRS Bulletin* **22** 20 (1997)

[18] S.B. Krupanidhi, N. Maffei, M. Sayer and K. El-Assal *J. Appl. Phys.* **54** 6601 (1983)

[19] O. Auciello, A. I. Kingon and S. B. Krupanidhi *MRS Bulletin* **21** 25 (1996)

[20] O. Auciello and R. Ramesh *MRS Bulletin* **21** 31 (1996)

[21] S. R. Mejia, R. D. McLeod, K. C. Kao and H. C. Card *Rev. Sci. Instrum*. **57** 493 (1986)

[22] S. K. Dey and P. V. Alluri *MRS Bulletin* **21** 44 (1996)

[23] B. A. Tuttle and R. W. Schwartz *MRS Bulletin* **21** 49 (1996)

[24] G. H. Haertling *The 5th US-Japan seminar on Dielectric and Piezoelectric ceramics, Kyoto, Japan, December* (1990)

[25] M. Oikawa and K. Toda *Appl. Phys. Lett*. **29** 491 (1976)

[26] L. S. Philips *Electron. Comp* **12** 523 (1971)

[27] M. de Keijser and G. J. M. Dormans *MRS Bulletin* **21** 37 (1996)

[28] M. Kojima, M. Okuyama, T. Nakagawa and Y. Hamkawa *Jpn. J. Appl. Phys. 22 Suppl*. 2 14 (1983)

[29] M. Okada, S. Takai, M. Amemiya and K. Tominaga *Jpn. J. Appl. Phys*. **28** 1030 (1984)

[30] J. H. Kim and S. Hishita *J. Mater. Sci.* **30** 4645 (1995)

[31] K. Uchino, N. Lee, T. Toba, N. Usuki, H. Aburatani and Y. Ito *J. Ceram. Soc. Jpn*. **100** 1091 (1992)

[32] A. Mansingh and C. V. R. Vasanta Kumar *J. Mater. Sci. Lett*. **7** 1104 (1998)

[33] S. B. Desu *J. Electrochem. Soc.* **140** 2981 (1993)

[34] S. B. Desu *Mater. Res. Soc. Symp. Proc*. **20** 199 (1990)

[35] T. R. Taylor, P. J. Hansen, N. Pervez, B. Acikel, R. A. York and J. S. Speck *J. Appl. Phys.* **94** 3390 (2003)

[36] M. –C. Wang, F. –Y. Hsiao, H. –H. Huang and N. –C. Wu *Jpn. J. Appl. Phys*. **43** 6323 (2004)

[37] C. S. Hawang, B. T. Lee, C. S. Kang, J. W. Kim, K. H. Lee, H. Cho, H. Horii, W. D. Kim, S. I. Lee, Y. B. Roh and M. Y. Lee *J. Appl. Phys*. **83** 3708 (1998)

[38] S. Zafar, R. E. Jones, B. Jiang, B. White, P. Chu, D. Taylor and S. Gillespie *Appl. Phys. Lett*. **73** 175 (1998)

[39] Y. Nakata, W. K. A. Kumiduni, T. Okada and M. Maeda *Appl. Phys. Lett*. **64** 2599 (1994)

[40] T. –F. Tseng, M. –H. Yeh, K. –S. Liu, and I. –N. Lin *J. Appl. Phys*. **80** 4984 (1996)

[41] M. G. Norton and C. B. Carter *J. Mater. Res.* **5** 2762 (1990)

[42] M. G. Norton, C. Scarfone, J. Li, C. B. Carter and J. W. Mayer *J. Mater. Res*. **6** 2022 (1991)

[43] W.J. Kim, W. Chang, S.B. Qadri, J.M. Pond, S.W. Kirchoefer and J.S. Horwitz *Appl. Phys. A* **70** 313 (2000)

[44] T. –L. Ren, X. –N. Wang, J. –S. Liu, H. –J. Zhao, T. –Q. Shao, L.-T. Liu and Z. –J. Li *J. Phys:D Appl. Phys*. **35** 923 (2002)

[45] H. B. Sharma, H. N. K. Sharma and A. Mansingh *J. Mater. Sci.* **34** 1385 (1999)

[46] http://www.iap.tuwien.ac.at/www/surface/STM_Gallery/nonmetals.html

[47] T.S. Kang, Y.S. Kim and J. H. Je *J. Mater. Res.* **15** 1955 (2000)

[48] Y. Kaga, Y. Abe, H. Yanagisawa and K. Sasaki *Jpn. J. Appl. Phys*. **37** 3457 (1998)

[49] O. Auciello, A. I. Kingon, A. R. Krauss and D. J. Lichtenwalner, in Multicomponent and Multilayered Thin Films of Advanced Microtechnologies: Techniques, Fundamentals and Devices, O. Auciello and J. Engemann, eds., Kluwer Acad. Press 151-208 (1993)

[50] S. M. Rossnagel, in [10] p. 1-20

[51] J. A. Thorton *J. Vac. Sci. Technol.* **11** 666 (1974)

2. Structural and optical properties of $BaTiO_3$ thin films prepared by radio-frequency magnetron sputtering at various substrate temperatures[1]

Abstract

Thin films of $BaTiO_3$ were prepared by radio-frequency magnetron sputtering at substrate temperatures from 450 to 750°C and analyzed by x-ray diffraction, optical transmittance and Raman spectroscopy. The packing density of the films relative to the crystalline density increases from 0.75 at 450°C to about 1 at 750°C. At a substrate temperature of 450°C, the film is nanocrystalline (5 to 20 nm) with big lattice expansion, large band gap and pronounced hexagonal Raman lines. This film is homogeneous in the thickness direction. Films prepared at higher temperatures exhibit perovskite peaks in the Raman spectrum and an optical band gap of 3.38 eV. At 600 °C, the film exhibits a pronounced two-phase growth with a porous nucleation layer of initial packing density of 0.78, a preferred (100)-orientation of the grains and minimum micro-strain. At 750°C, the films are again homogeneous in the thickness direction, have nearly crystalline packing density and preferably (110)-oriented grains.

[1] This chapter was published in *J. Phys. D: Appl. Phys.* **39** 1161 by Y. K. Vayunandana Reddy, D. Mergel, S. Reuter, V. Buck and M. Sulkowski.

2.1 Introduction:

Large dielectric constant materials with perovskite structure have attracted great interest for potential applications in non-volatile, high speed ferroelectric random access memories (FeRAM) and dynamic random access memories (DRAM) [1,2], in microwave devices especially like high speed microelectronics, radar, communication systems [3], humidity-sensitive sensors [4], and electro-optical devices [5], because of their high dielectric constant, low leakage current density, and high dielectric breakdown strength. Such high dielectric constant ferroelectric thin films are $SrBi_2Ta_2O_9$ (SBT), $PbTiO_3$ (PTO), $Pb_xZr_{1-x}TO_3$ (PZT), and $BaTiO_3$ (Barium titanate, BTO), these materials are extensively studied for above mentioned applications. Among these materials, BTO thin films are one of the most promising candidates.

BTO thin films have been deposited by several methods like metal-organic chemical vapor deposition (MOCVD) [6], sol-gel method [7,8], chemical solution deposition [9] and radio-frequency (rf) sputtering [10]. Among the various methods, sputtering is an excellent method to produce thin films on various substrates with good stoichiometry that can easily be upscaled for industrial applications.

Properties of thin films are dependent on various deposition parameters like deposition technique, substrate temperature, total pressure and composition of the operating gas. The substrate temperature plays a pivotal role in BTO thin film properties like orientation, crystallinity and surface morphology [11].

The function of BTO thin films in opto-electronic devices depends on structural and optical properties like grain size, lattice distortion, micro-strain, band gap, refractive index and absorption. It is important to study how these properties depend on deposition parameters. Several studies suggest that a strong correlation between the optical properties and the crystalline structure of the perovskite thin films exists. The band gap is the best example: with increasing crystallinity of the films the band gap decreases [12].

In this paper, we investigate BTO thin films prepared by radio frequency (rf) magnetron sputtering at various substrate temperatures and study their structural and optical properties, and

their surface morphology. There are some papers where a giant dielectric constant in oxygen-deficient hexagonal BTO single crystals are reported [33,34]. Therefore, we prepared oxygen-deficient BTO thin films in order to study their structural and optical properties relevant for optoelectronic applications [5]. The samples were prepared at substrate temperatures from 450°C to 750°C covering the range reported in the literature [10, 35]. We have used quartz substrates because they withstand the high deposition temperatures and allow optical transmittance spectroscopy in a wide spectral range.

2.2 Experimental details

Thin films of BTO were deposited on quartz substrates in a von Ardenne Laboratory System LS 500 S by radio-frequency (rf) magnetron sputtering with a stoichiometric BTO target with a purity of 99.99% with 150 mm diameter (FMR Anlagenbau GmbH). The substrate-to-target distance was 5 cm. Circular quartz substrates with a diameter of 25 mm were used. They are homogeneously coated as has been checked with thickness profilometry.

We used 500W rf power and 15 sccm argon flux and kept the Ar sputter chamber pressure constant at 6.5×10^{-3} mbar for all experiments. The substrates were ultrasonically cleaned for 15 minutes and then cleaned with acetone and diethyl ether prior to BTO film deposition. The substrate temperature was varied from 450 to 750°C in order to investigate the influence of processing temperature on various film properties. The thickness of the films is about 950 ± 50 nm, except for those deposited at 750°C where it is about 670 nm.

The geometrical thickness was determined at a film edge by the stylus method with a Tencor P10 profilometer. In order to produce the edge, a line was marked on a substrate with a felt pen before coating and removed after coating together with the material deposited on top of it. The mass of the films was estimated by weighing the substrates before and after deposition with a comparator balance (Sartorious C50) with a nominal resolution of 1 µg.

In order to investigate the structural properties, we have used a Siemens D5000 $\theta - 2\theta$ X-ray diffractometer using Cu $K\alpha$ radiation at 1.5046 Å. The surface morphology was examined by atomic force microscopy in contact mode (Auto-Probe CP Research). Optical transmission

spectra measurements were carried out in the wavelength range of 200 to 2000 nm by using a Perkin – Elmer Lambda-9 spectrometer. To evaluate the optical properties from transmittance spectra, we used the SCOUT 2 commercial software to fit transmittance spectra derived from physical model to the experimental data (dielectric modeling) for dielectric simulation [13]. This program was already used in our group for the dielectric modeling of transmittance and reflectance spectra of In_2O_3:Sn, SiO_2, HfO_2 and ZrO_2 thin films [14,15]. The film thickness *d* was also determined by fitting the spectra.

Micro-Raman measurements were performed at room temperature with a Jobin Yvon's LabSpec spectrometer with a magnification of 100 and a resolution of 2 cm^{-1}, using the 514.5 nm line of an argon ion laser as the excitation source with a laser output power of 45 mW.

A cross sectional micrograph was obtained by scanning electron microscopy (SEM) with a FEI Quanta 400 FEG. Rutherford Backscattering (RBS) was performed with 2 MeV He-ions, in order to obtain the chemical composition.

The error in weighing is about 5%, that in measuring the film thickness about 3.5%. The position of an XRD peak can be determined with an uncertainty of about ±0.05° to 0.1°. The uncertainty of the width of an XRD peak (full width at half maximum) is about ±0.01° to 0.04° depending on the shape of the peak.

2. 3. Results and discussion

2.3.1 Deposition rate, packing density and composition

Fig. 2.1 shows that the mass density of the BTO thin films increases with increasing substrate temperature. At lower substrate temperature (450°C), the packing density is about 0.75 and at 750°C it reached the crystalline density (5.85 g/cm^3). It shows very clearly that at higher substrate temperatures the films are uniform and compact. The deposition rate does not depend much on the temperature: at 450°C it was 0.21± .01nm/s and at higher substrate temperatures it was 0.28 ± .01nm/s.

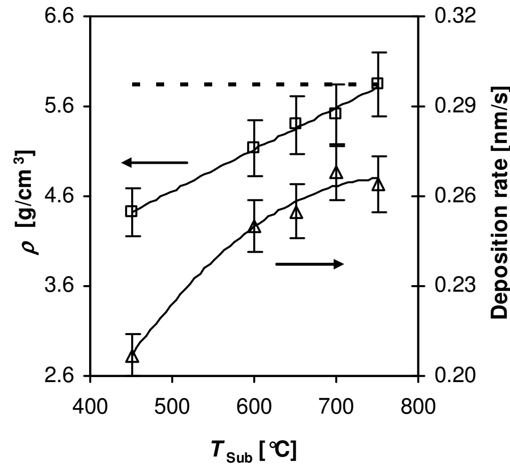

Fig. 2.1 Density and deposition rate of BTO thin films deposited at various temperatures. The deposition rate was calculated from the measured mass per area and the crystalline density of $BaTiO_3$ (5.85 g/cm³, dashed line).

In order to determine the composition of the films, Rutherford Backscattering (RBS) was performed with 2 MeV He-ions. The resulting spectra were fitted with a simulation program by varying the parameters manually. The composition of three representative samples was found to be: $Ba_{0.98}Ti_{1.01}O_{2.8}$, $Ba_{0.94}Ti_{1.03}O_{2.80}$, and $Ba_{0.95}Ti_{1.02}O_{2.95}$ for a sample prepared at 450°C, 600°C, and 750°C, respectively. The errors in the coefficients are ± 0.02 for Ba, ± 0.05 for Ti and O. They were determined by varying the parameters in the simulation until a deviation of the simulated from the measured spectra became visible. The size of the coefficients was chosen such that O_3 is expected for a mixture of BaO and TiO_2. We see that our films seem to contain more Ti than Ba ([Ti]/[Ba] = 1.05(5)) and are O-deficient (about 2% for 750°C and about 7% for 600°C and 450°C).

2.3.2 Structural properties from XRD

From x-ray diffractometry we would like to identify the crystalline phases (cubic or hexagonal) in the thin films and to estimate the texture of crystalline orientations, i. e. the preferred orientation of the grains.

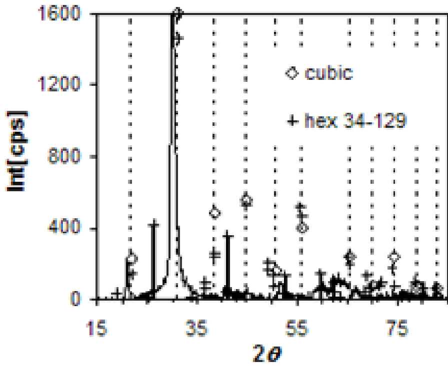

Fig. 2.2

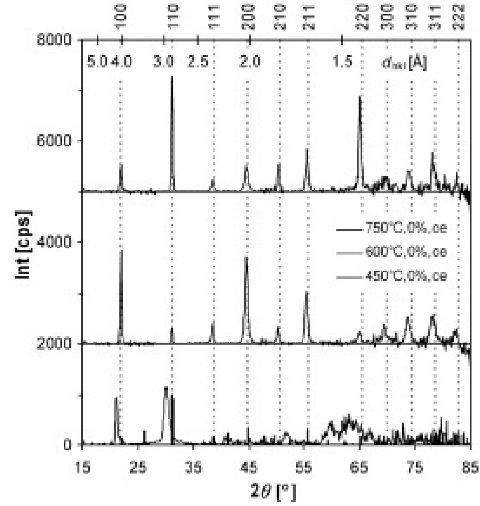

Fig.2.3

Fig. 2.2 XRD spectra of the BTO thin film deposited at 450°C. The intensity has been normalized in order to account for the finite thickness of the thin film [16]. The vertical dotted lines represent the position of the reflexes of the cubic structure. The PDF intensities of the cubic and the hexagonal phase are indicated by the diamond and the cross symbols, respectively. The vertical bold lines represent the position of some hexagonal reflexes that are clearly distinct from the cubic ones.

Fig. 2.3 Normalized XRD spectra of the BTO thin film deposited at various temperatures. The reflexes of the cubic phase are marked with vertical dotted lines. The powder diffractogram of the hexagonal powder is represented by the bold vertical lines close to the x-axis. From bottom to top: 450°C, 600°C, and 750°C, respectively.

Fig. 2.2 shows the x-ray diffractogram of a sample deposited at 450°C together with the cubic and hexagonal peaks obtained with crystalline powders (PDF 31-174 and 34-129 for the cubic and hexagonal phase, respectively). The ordinate values of the PDF data correspond to the reported PDF intensities. In order to compare the experimental data with the PDF intensities we have to correct for the final thickness of our films. This was done in the way described in Ref. [16].

Most of the peak positions of the cubic and the hexagonal phases are practically indistinguishable. There are only five hexagonal peaks that are isolated from the cubic peaks. We have then plotted them in Fig. 2 with bold vertical lines. We see that there is a considerable

measured intensity at the positions of four of these lines indicating the presence of the hexagonal phase. The strong peaks at 2θ=21.3 and 2θ=30.24 are shifted with respect to the crystalline positions of c-(100) or h-(102) and c-(110) or h-(104) to smaller angles indicating bigger lattice constants. We shall see later that the Raman spectra of the sample prepared at 450°C is distinct from the spectra of the other samples.

In order to estimate the texture of crystalline orientations, the measured x-ray intensities have been normalized with the powder diffraction intensities in the way described in Ref. [16] in detail. Essentially, the measured peak intensities are divided by the corresponding PDF intensities. For the curves in Fig. 2.3 we used the BTO cubic powder diffraction data (JCPDS-ICDD 31-174). For a random texture, i.e. when all grain orientations are equally probable, all peaks should have the same height after this normalization.

Fig. 2.3 shows XRD patterns of the BTO thin films deposited on quartz at various substrate temperatures after peak height normalization. It is evident that in our films there is no random orientation of the grains.

At a substrate temperature of 600 °C, the film shows polycrystalline nature with predominant (100) orientation together with its second-order (200). At substrate temperature 750°C, the predominant peak is (110) together with its second-order (220) and the remaining peaks exhibit only a very low intensity. The diffractograms at 650 and 700°C look similar to those at 600°C and 750°C, respectively. Finally we can say that with increasing the substrate temperature above 650°C, the films became more dense and crystallized with (110) as the most pronounced grain orientation.

The second order reflexes (200) and (220) exhibit the same intensity as the first orders, (100) and (110), respectively. This shows that the normalization with the powder intensities of the cubic crystals is reasonable.

These diffractograms reveal that (110) is the dominant orientation of grains in films prepared at higher substrate temperatures. The peak intensity (110) increases with increasing

substrate temperature up to 750°C. These results are in good agreement with those reported in the literature: Sharma et al. (films prepared by sol-gel method) [7], Hu et al. (films prepared by modified sol-gel method) [8] and Ring et al. (PVD) [17], Zhang et al. (hydrothermal technique) [18] and Wang et al. (rf magnetron sputtering) [19] also observe that.

The deposition temperature plays a pivotal role in determining the structural properties of the films. As observed by Jia et al. [10], BTO films are amorphous in nature at substrate temperatures below 450°C. The diffractogram of our sample prepared at 450°C shows strongly shifted peaks, close to cubic (100) and (110). Between $2\theta = 50°$ to 70°, the maxima are closer to hexagonal peaks. However, in the region of $2\theta = 27°$ no hexagonal peak is observed. The grain diameter for our film is about 5 to 20 nm, as inferred from AFM pictures as will be seen below.

We therefore draw the preliminary conclusion that our film prepared at 450°C consists of nano-crystals. This is well consistent with the literature. Thin films prepared at 500°C by rf magnetron sputtering are composed of granular crystallites of about 45 nm size for a film thickness of 450 nm observed by His et al. [32] and of about 30 nm size for a film thickness of 45 nm observed by Wang et al. [31]. For samples prepared at higher temperatures, the position of the (110) peak shifts to higher 2θ values indicating a smaller lattice constant.

The lattice distortion as a function of substrate temperature is shown in Fig. 2.4.
It is calculated as:

$$\delta = \frac{d - d_{hkl}}{d_{hkl}} \tag{2.1}$$

where d is the lattice spacing calculated from the measured 2θ value of the XRD peak and d_{hkl} is the ideal lattice spacing of the single crystal. This parameter is sometimes called “uniform strain”. For our samples, always a lattice expansion is observed.

At lower substrate temperature (450°C), the films have bigger lattice distortion for both (100) and (110) oriented grains, and with increasing substrate temperature, the calculated lattice distortion is very low compared with that at lower temperatures. It is a good indication that the

films are well orientated with predominant orientation of (100) and (110) for lower and higher substrate temperatures, respectively.

A shift of the (111)-reflex with respect to an ideal lattice was observed for nano-crystalline BTO powder [20]. With decreasing crystallite size the 2θ values of the (111) – peak were shifted towards smaller values. However, for a crystallite size of 15 nm, the lattice distortion was only 0.0074, a factor of five smaller than for our film prepared at 450°C.

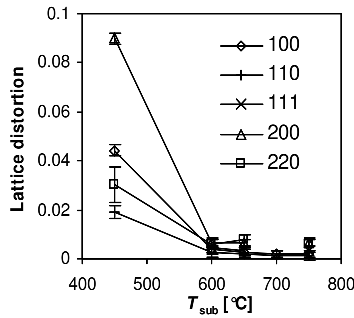

Fig. 2.4 Lattice distortion of BTO thin films deposited at various temperatures. Calculated from Eq. (1).

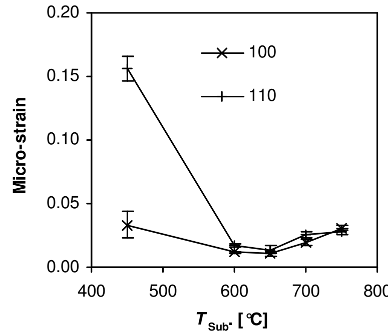

Fig. 2.5 Plot of $\Delta(2\theta)$ (full width at half maximum) for some reflexes with first and second order peaks vs. $\sin\theta$.

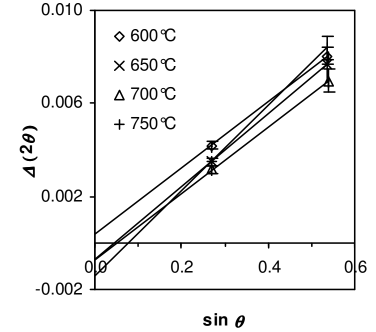

Fig. 2.6 Micro-strain (statistical strain) of the BTO thin films evaluated according to Eq. (3).

The width of the peaks is more difficult to interpret because in polycrystalline materials there are two sources of angular line broadening $\Delta 2\theta$: finite crystallite size and non-uniform strain [21]. The corresponding formulas for the evaluation are:

(1) Finite crystallite size C, described by the Scherrer formula:

$$\Delta(2\theta) = \frac{K \cdot \lambda_x}{C \cdot \cos\theta} \quad (2.2)$$

Where K is the Scherrer constant (K=0.9 for spherical particles), λ_x is the x-ray wavelength.

(2) Local variations of the lattice spacing (average non-uniform strain) $\varepsilon_{var} = \Delta d_{var}/d_o$ described by:

$$\Delta(2\theta) = 2\varepsilon_{\text{var}} \tan\theta \tag{2.3}$$

In thin films, the two effects generally superimpose. To determine C and ε_{var} from the line width when high order reflexes are present, an easy method was developed by Vook et al. [22]. The observed broadening was treated as a sum of Eqs. (2.2) and (2.3). In order to distinguish between the two mechanisms, $\Delta(2\theta)$ has to be plotted as a function of $\sin\theta$ for several reflections of the same crystallite orientation. A straight line is fitted to the data. C is then obtained from the intercept at $\sin\theta = 0$ and ε_{var} from the slope. Fig. 2.5 shows that the main effect on the width is due to the micro-strain. The intercept is nearly zero. This situation is similar to that found for thin films of In_2O_3:Sn prepared by dc-magnetron sputtering [23]. We therefore evaluate the width of the XRD peaks by means of Eq. (2.3) to get the micro-strain ε_{var}.

The "microstrain" or "average non-uniform strain" or "statistical strain" (all these terms are used in the literature) is isotropic. Its origin is defects, e.g. point defects or dislocations that cause a statistical variation of the lattice constant and therefore limit the coherence length of the lattice for the x-rays.

The micro-strain is shown in Fig. 2.6 as a function of the deposition temperature of the films. When prepared at lower substrate temperatures, the films exhibit a high statistical (non-uniform) strain indicating a higher defect density. This may be due to lower mobility of the adatoms on the growing film. At about 600°C, the micro-strain is minimum.

2.3.3 Optical properties from the transmittance

Fig. 2.7 depicts the measured optical transmittance spectrum of a BTO thin film deposited at 600°C substrate temperature, together with two other curves representing the results of fits based on dielectric modeling with two different layer stacks. The films were highly transparent in the visible region with about 85% transmittance. The ondulated shape is the result of interference between light reflected at the air-film and film-substrate interfaces. With increasing optical film thickness (= *nd*) , more interference fringes occur.

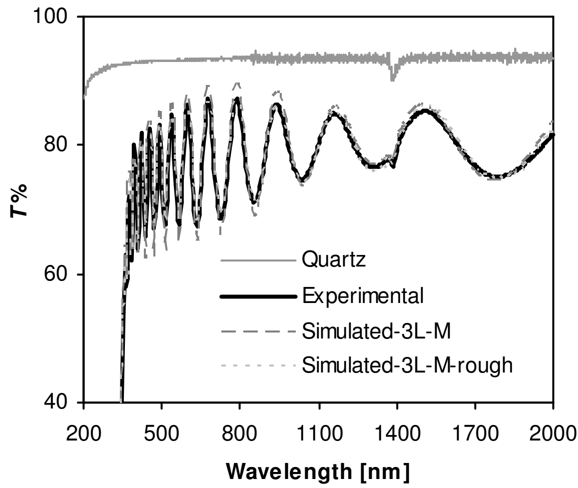

Fig. 2.7 Transmittance and simulated spectra of BTO thin films deposited at 600°C with different simulation parameters (Simulated-3L-M and Simulated-3L-M-rough, represented as, simulated with 3 layer modell and with rough interface, respectively.).

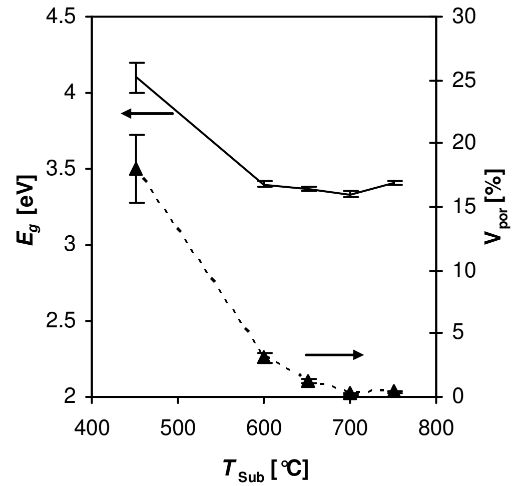

Fig. 2.8 Band gap (E_g) and pore volume (V_{por}) as calculated from the optical simulation.

Optical spectra were calculated and fitted to the experimental ones by using the SCOUT 2 simulation software [13]. The dielectric function used two types of electronic excitations: band gap transitions and inter-band transitions. The inter-band transitions were modeled by a harmonic oscillator. For the band gap transitions, the formula of O'Leary, Johnson, and Lim (OJL) was used that was proposed to model the band gap of amorphous silicon [24]. With this procedure, optical parameters like band gap E_g (defining the gap between the valence band and the conduction band), γ(reflecting the width of the exponential decay of the density of states in the band gap), and the frequency of the harmonic oscillator representing the inter-band transitions were obtained.

In our simulations, we used two different layer stacks. The first model comprises only a single homogeneous layer, the second model comprises several layers: a porous layer on the substrate and a compact top layer. Sometimes a second porous layer was introduced to model a porosity gradient. The porosity was taken account of by using the Bruggeman model [25] for an effective dielectric medium. The material parameters were supposed to be the same in all layers, only the volume fraction of the material in the porous layers was varied in order to get a good fit to the spectra for different films deposited at various substrate temperatures.

For the film deposited at a substrate temperature of 450°C, a single porous layer could describe the experimental spectrum quite well. The volume fraction of this film came out to be 90%. The packing density obtained from the mass measurement and the film thickness is about 0.75 (see Fig. 2.1), less than the volume fraction of 0.9 obtained from the optical fitting. This means that the intrinsic density of the nanocrystalline material (without pores) is only about 0.75/0.9 = 0.83 of the crystalline density. This may be due to the high density of grain boundaries in the nanocrystalline material.

The transmittance spectrum of the film deposited at 600°C substrate temperature did not reach the transmittance of the uncoated substrate (Fig. 2.7), contrary to what is expected for a homogeneous non-absorbing film. A three-layer model was necessary to get a good fit to the experimental spectrum. The dotted and the full lines in Fig. 2.7 represent the simulations without and with a rough interface top of the two porous layers, respectively.

For models including several layers, there is the danger that too many fitting parameters are involved in the simulation and the results cannot be interpreted physically. In order to avoid this trap, we have minimized the number of parameters. We assume that there is only one material characterized by band gap (OJL-model [24]) and interband transitions (represented by one harmonic oscillator). The various layers are distinguished by different filling fractions, f_V, of the material, taken into account by the Bruggeman effective medium model. Furthermore, a rough interface was assumed.

A good fit to the transmittance of the sample prepared at 600°C was obtained by a structural model with a roughness that scatters about 1% to 2% of the light and three layers with different thickness d and filling fraction f_V: a compact top layer (d = 890 to 940 nm, $f_V = 1$) a porous intermediate layer (d = 35 to 50 nm, f_V = 0.9 to 0.92) and a porous bottom layer (d = 145 to 155 nm, f_V = 0.75 to 0.8). The variation in the parameters was obtained by fixing one of the parameters and automatically adjusting the other parameters until a visible deviation of the simulated curve from the experimental data was obtained. The total thickness of the film for all these parameter variations varies only little: d_{film} = 1.09 to 1.11 µm.

For the film deposited at a substrate temperature of 450°C, a single porous layer could describe the experimental spectrum quite well. The volume fraction of this film came out to be 77% to 90%. The packing density obtained from the mass measurement and the film thickness is about 0.75(5) (see figure 1), less than the volume fraction obtained from the optical fitting. Due to the large uncertainty in the data precise conclusions cannot be drawn. A possible smaller intrinsic density of nano-crystalline material could be due to the high density of grain boundaries.

Fig. 2.8 represents the band gap and the pore volume (vol %) as obtained from the optical simulations. We see that the band gap and the pore volume follow the same trend: they decrease with increasing temperature.

It is shown in Fig. 2.8 together with the band gap E_g for the samples prepared at different temperatures. The film prepared at 450°C is nanocrystalline, homogeneous, and exhibits a relatively large band gap. The refractive index (n) at 633 nm is 1.91(1). It is seen that at 600°C a change in growth takes place. From 600°C on, the samples are crystalline with a band gap of about 3.4 eV and a refractive index of 2.19(1). At 600°C, d_{pore} exhibits a clear maximum.

The choice of the structural model is justified by inspection of Fig. 2.7. It is clearly seen that a model with one homogeneous layer does not fit to the data. Two features of the experimental data are responsible for that: the experimental transmittance does not reach the transmittance of the uncoated substrate and the amplitude of the modulation of T varies periodically with a visible minimum at about 1300 nm. These effects are due to interference at internal interfaces that are evidently well modelled by the three-layer model presented above.

In summary: the film deposited at 600°C exhibits a pronounced two-phase growth with a porous nucleation layer of initial packing density 0.78 and a total thickness of 200 nm. As can be seen in Fig. 2.3, this film exhibits preferred (100)-orientation of the grains. This two-phase structure may be the reason for the minimum micro-strain (statistical, non-uniform strain) observed in Fig. 2.6.

The films deposited at substrate temperatures above 600°C could be modelled with two layers only, a porous bottom layer and a compact layer. The bottom layer became less porous and thinner with increasing temperature. For the film prepared at 750°C, the thickness of the under-layer and the filling fraction (f_V) are 120 nm and 0.95, respectively.

Fig. 2.8 clearly shows that the band gap is decreasing with increasing deposition temperature. At lower temperature it is 3.96 eV and at higher temperature it is 3.36 eV. The same trend was also observed by Kamalasanan et al. [12].

The refractive index *n* and the extinction coefficient *k* (inset) for three samples deposited at 450°C, 600°C, and 750°C, respectively, are shown in Fig. 2.9 as a function of the wavelength. The refractive index *n* at 633 nm as calculated from the simulation is 1.92 and 2.47 for the films prepared at 450 and 750°C substrate temperatures, respectively. These values tell that with increasing crystallinity the refractive index *n* increases. A similar trend was also observed by Jia et al. [10] and Kamalasanan et al. [12]. It is clear that the optical parameters are directly correlated with the structural properties.

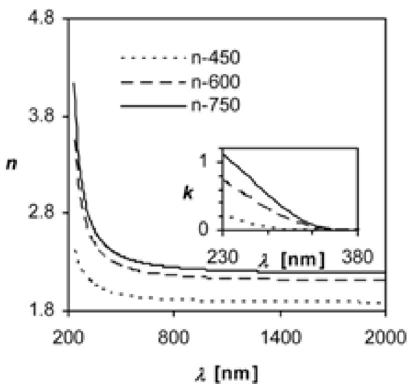

Fig. 2.9

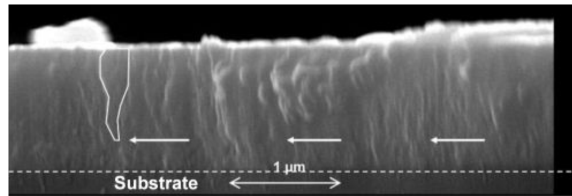

Fig. 2.10

Fig. 2.9 Refractive index *n* and extinction coefficient *k* (inset) as a function of wavelength for three samples deposited at 450°C, 600°C, and 750°C, respectively.

Fig. 2.10 Cross sectional SEM of the film deposited at 600°C (arrow marks indicates the growth change and the white line indicates crystal growth).

We have made a SEM picture (Fig. 2.10) of the cross section of the film represented in Fig. 2.7. The edge was obtained by breaking the sample. A change in film growth is observed at

about 200 to 250 nm. This has to be compared with the thickness of the porous layers of about 200 nm obtained in the simulation.

2.3.4 Raman spectroscopy

Room temperature micro-Raman spectra of the BTO thin films deposited at various substrate temperatures are shown in Fig. 2.11. The film deposited at 450°C produces a pronounced hexagonal signal and the films deposited above 450°C show perovskite signals. BTO is a typical ferroelectric material that has cubic structure above the Curie temperature ($T_C >$ 120°C) and belongs to the $P_{m3\,m}$ space group and below this ($T_C <$ 120°C) it is tetragonal with $P_{4\,m\,m}$ symmetry which again transforms into orthorhombic and rhombohedral structures at 5°C and at -90°C, respectively. In the cubic (paraelectric) phase there are four triply degenerate optical modes of vibrations ($3F_{1u}+1F_{2u}$). The F_{1u} mode is IR active and the F_{2u} mode is the so-called "silent mode" since it is neither infrared nor Raman active. In the tetragonal (ferroelectric) phase, three A_1+E phonons arise from the three F_{1u} modes, whereas one $E+B_1$ mode comes from the F_{2u} silent mode. All the A_1 and E modes are IR and Raman active, but B_1 is only Raman active. These modes further split into longitudinal (LO) and transverse (TO) components due to the long range electrostatic forces associated with lattice ionicity [26]. Again each A_1 or E mode splits into a pair of modes, A_1 into $A_1(TO)+A_1(LO)$ and E into $E(TO)+E(LO)$.

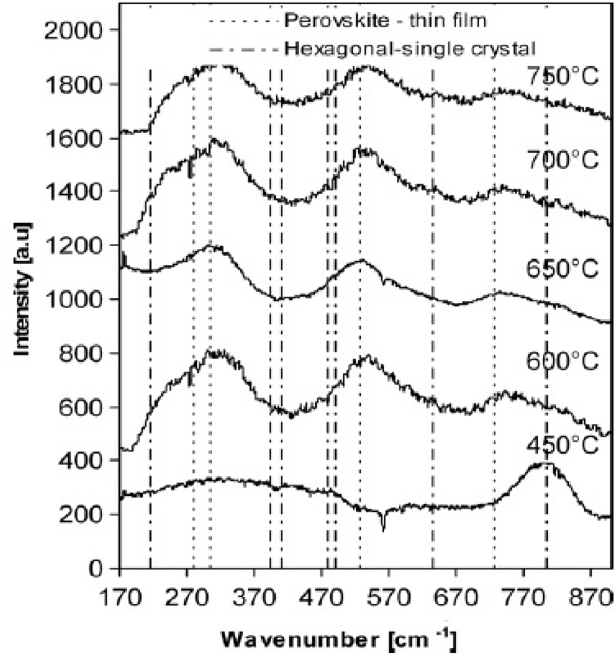

Fig. 2.11 Raman spectra of the BTO thin films prepared at different temperatures. Broken vertical and chain lines represent the Raman lines of the perovskite [30] and the hexagonal [27] phase, respectively.

For our BTO films deposited at 450°C, there is a strong signal at 800 cm^{-1}. It appears only for the low temperature film and it is highly probable that this signal appears because the film is amorphous or nano-crystalline. Such a signal was also observed for thin films with hexagonal crystal structure [27]. At higher substrate temperatures, all Raman spectra are similar and due to a perovskite crystal structure. A broad $A_1(TO_2)$ mode at 273 cm^{-1} is observed. The $E(TO_2)$ mode, which has been associated with the tetragonal-to-cubic phase transition [28], is observed at 305 cm^{-1}. The third asymmetric $A_1(TO_3)$ mode is observed at 520 cm^{-1}. The mixture of $A_1(LO_3)$ and $E(LO_3)$ mode [29] is observed at 720 cm^{-1}.

2.3.5 Surface morphology

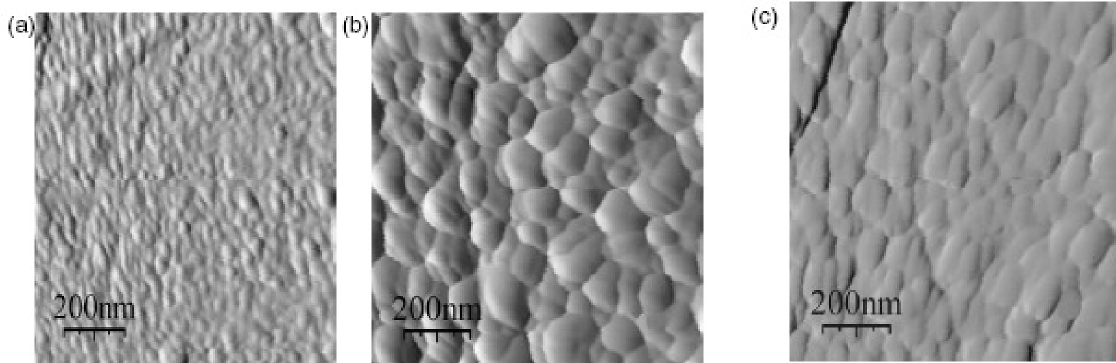

Fig. 2.12 AFM images of the BTO thin films deposited at (a) 450°C, (b) 600 and (c) 750°C.

The effect of the substrate temperature on the surface morphology of the BTO thin films was examined by atomic force microscopy. Fig. 2.12 shows the results for the films deposited at 450, 600 and 750°C, respectively. The surface roughness (rms) of these thin films is 1.16, 2.4, and 3.27 nm, respectively. The increase in surface roughness results essentially from grain formation. For the 450°C film, the image shows that there are very small grains with a diameter of about 20 nm. The film prepared at 600°C predominantly consists of platform grains with a diameter of up to 70 nm. The 750°C film with the thickness of 670 nm mainly consists of rectangular and polyhedral grains with a diameter of 90 to 115 nm. This result indicates that the growth of larger grains with increasing temperature leads to an increase in the surface roughness.

2.4 Conclusions

We investigated the structural and optical properties of BTO thin films grown on quartz substrates by radio-frequency magnetron sputtering. The BTO thin film grown at a low temperature of 450°C has a surface morphology with a lateral grain size of less than 20 nm. This could be an indication of a nano-crystalline microstructure.

This film has a packing density of 0.75 with respect to the crystalline density, large lattice distortion, large band gap (3.96 eV), and pronounced hexagonal Raman lines. It is homogeneous in the thickness direction. On the other hand, the film grown at 600°C is not homogeneous in the

thickness direction. It starts growth with a porous layer of initial packing density 0.78 and total thickness of 200 nm. The remaining film (800 nm) has crystalline density. This film shows a preferred (100)-orientation of the grains and minimum micro-strain.

The film grown at 750°C is again homogeneous in the thickness direction, has a total packing density of 0.95 and a preferred (110)-orientation of the grains. The grain size and the surface roughness as observed with AFM increase with increasing substrate temperature. With increasing crystallinity of the films, the band gap decreases and the refractive index increases. This is a clear indication of a correlation between optical and structural properties.

This study demonstrated that at 600°C a change in film growth with resulting structural and optical film properties happens and the films become inhomogeneous in the thickness direction. For use as optical layer or as dielectric layer in capacitors we suggest to use lower (450°C) or higher (>700°C) substrate temperatures for preparation.

Acknowledgements

This work was supported by the Deutsche Forschungsgemeinschaft (DFG) in the framework of the Graduiertenkolleg 689 “Reactivity in the surface area”. We would like to thank Thorsten Balgar for performing AFM and Hans Werner Becker, University of Bochum for performing RBS.

References

[1] J. F. Scott and C. A. P. De Araujo *Science* **246** 1400 (1989)

[2] M. Shimizu, M. Fujimoto and E. Tanikawa *Mater. Res. Soc. Symp. Proc*. **310** 255 (1993)

[3] M. P. McNeal, S. –J. Jang and R. E. Newnhan *J. Appl. Phys.* **83** 3288 (1998)

[4] S. N. Chen, E. S. Ramakrishnan and W. W. Grannemann *J. Vac. Sci. Technol A* **3**, 678 (1985)

[5] A. B. Kaufman *IEEE Trans. Electron Devices* **16** 562 (1969)

[6] A. R. Terren, J. A. Belot, N. L. Edleman, T. J. Marks and B. W. Wessels *Chem. Vap. Dep*. **6** 175 (2000)

[7] H. B. Sharma and A. Mansingh *J. Phys. D: Appl. Phys*. **31** 1527 (1998)

[8] Z. Hu, g. Wang, Z. Huang, X. Meng and J. Chu *Semicond. Sci. Technol*. **18** 449 (2003)

[9] J. Petzelt, T. Ostapchuk, A. Paskin and I. Rychetsky *J. Europ. Ceram. Soc*. **23** 2627 (2003)

[10] Q. X. Jia, J. L. Smith, L. H. Chang and W. A. Anderson *Phil. Mag. B* **77** 163 (1998)

[11] J. Zhang, D. Cui, H. Lu, Z. Chen, Y. Zhou and L. Li *Jpn. J. Appl. Phys*. **36** 276 (1997)

[12] M. N. Kamalasanan, N. D. Kumar and S. Chandra *J. Appl. Phys.* **76** 4603 (1994)

[13] SCOUT 2, M. Theiss, Hard- and Software for Optical Spectroscopy, Aachen, Germany, www.mtheiss.com.

[14] D. Mergel and Z. Qiao *J. Phys D : Appl. Phys* **35** 794 (2002)

[15] M. Jerman, Z. Qiao and D. Mergel *Appl. Opt*. **44** 3006 (2005)

[16] D. Mergel, K. Thiele and Z. Qiao *J. Mater. Res*. **20** 2503 (2005)

[17] K. M. Ring and K. L. Kavanagh *J. Appl. Phys.* **94** 5982 (2003)

[18] M. –S. Zhang, Z. Yin, Q. Chen, W. Zhang and W. Chen *Solid State Commun*. **119** 659 (2001)

[19] B. Wang and L. Zhang *Phys. Stat. Sol. (a)* **169** 57 (1998)

[20] H.-J. Gläsel, E. Hartmann, D. Hirsch, R. Böttcher, C. Klimm, D. Michel, H. – C. Semmelhack, J. Hormes and H. Rumpf *J. Mater. Sci*. **34** 2319 (1999)

[21] S. Mader, in Handbook of Thin Film Technology, edited by L. I. Maissel and K. Glang (McGraw Hill, New York, 1970)

[22] R. W. Vook and F. Witt *J. Vac. Sci. Technol*. **2** 243 (1965)

[23] D. Mergel and Z. Qiao *J. Appl. Phys*. **95** 5608 (2004)

[24] S. K. O'Leary, S. R. Johnson and P. K. Lim *J. Appl. Phys*. **82** 3334 (1997)

[25] D. A. G. Bruggeman *Ann.Phys.* **24** 636 (1935)

[26] M. D. Jr. Domenico, S. H. Wemple, S. P. S. Porto and R. P. Buman *Phys. Rev.* **174** 522 (1968)

[27] H. Yamaguchi, H. Uwe, T. Sakudo and E. Sawaguchi *J. Phys. Soc. Jpn*. **56** 589 (1987)

[28] B. D. Begg, K. S. Finnie and E. R. Vance *J. Am. Ceram. Soc.* **79** 2666 (1996)

[29] J. L. Parsons and L. Rimai *Solid State Commun*. **5** 423 (1967)

[30] M. S. Chen, Z. X. Shen, S. H. Tang, W. S. Shi, D. F. Cui and Z. H. Chen *J. Phys.: Condens. Matter* **12** 7013 (2000)

[31] M. –C. Wang, F. –Y. Hsiao, C. –S. Hsi and N. –C. Wu *J. Crys. Growth* **246** 78 (2002)

[32] C. –S. Hsi, F.–Y. Hsiao, N. –C. Wu and M.–C. Wang *Jpn. J. Appl. Phys*. **42** 544 (2003)

[33] J. Yu, P.–F. Paradis, T. Ishikawa, S. Yoda, Y. Saita, M. Itoh and F. Kano *Chem. Mater.* **16** 3973 (2004)

[34] J. Yu, T. Ishikawa, Y. Arai, S. Yoda, M. Itoh and Y. Saita *Appl. Phys. Lett.* **87** 252904 (2005)

[35] C. L. Li, Z. H. Chen, Y. L. Zhou and D. F. Cui *J. Phys.: Condens. Matter* **13** 5261 (2001)

3. Structural and electrical properties of RuO_2 thin films prepared by rf-magnetron sputtering and annealing at different temperatures

Abstract

Highly conductive ruthenium oxide (RuO_2) thin films have been deposited at different substrate temperatures on various substrates by radio-frequency (rf) magnetron sputtering and were later annealed at different temperatures. The thickness of the films ranges from 50 to 700 nm. Films deposited at higher temperatures show larger grain size (about 140 nm) with (200) preferred orientation. Films deposited at lower substrate temperature have smaller grains (about 55 nm) with (110) preferred orientation. The electrical resistivity decreases slightly with increasing film thickness but is more influenced by the deposition and annealing temperature. Maximum resistivity is 861μΩcm, observed for films deposited at room temperature on glass substrates. Minimum resistivity is 40 μΩcm observed for a thin film (50 nm) deposited at 540°C on a quartz substrate. Micro-Raman investigations indicate that strain-free well-crystallized thin films are deposited on oxidized Si substrates.

3.1 Introduction

Until recently, Pt has been the most commonly used electrode for ferroelectric thin film capacitors due to its low resistivity and expected high chemical stability [1]. However, during annealing in oxygen ambient above 500°C, the degree of oxidation and inter-diffusion remarkably increased, resulting in the degradation of the electrical properties of ferroelectric materials [2]. Also, the sputtered Pt electrode is known to have the disadvantage of hillock formation which can electrically short-circuit the capacitor. Therefore, an alternative electrode material is desirable. Ruthenium dioxide (RuO_2) is one of the potential candidates.

RuO_2 is a stable conductive and semi-transparent oxide. It belongs to the family of transition-metal oxide compounds with tetragonal rutile structure with the crystalline density of 7.026 g/cm^3 [3], has a large work function (~5 eV) [4], high thermal and chemical stability [5,6] and high diffusion barrier capability [7]. This combination of properties makes RuO_2 a promising candidate for many applications, such as electrodes for high-*k* materials in dynamic random access memories (DRAM) [8] and non-volatile random access memories (NVRAM) [9], interconnects, contacts [10,11], and as diffusion barrier in very large scale integrated (VLSI) metallization systems [12]. The metallic conductivity arises from the partially filled Ru 4*d* states [13]. Its bulk resistivity is about 40 μΩcm [14].

An important property of an electrode for ferroelectric films is its influence on the fatigue behavior of the ferroelectric films. The use of RuO_2 as an electrode reduces the lattice mismatch and the work function difference at the electrode-ferroelectric film interface. Therefore, the defect entrapment and the loss of polarization are reduced, and consequently the fatigue behavior is improved [9]. With RuO_2 electrodes neither chemical reactions nor inter-diffusion phenomena take place at the electrode/ferroelectric or electrode/substrate interfaces [15].

RuO_2 thin films can be synthesized by several techniques such as pulsed laser deposition (PLD) [16], chemical vapor deposition (CVD) [17], metal-organic chemical vapor deposition

(MOCVD) [18], and rf sputtering [19]. Among these techniques, radio-frequency (rf) sputtering is the most commonly used technique.

In this present work we report the deposition of RuO_2 thin films on glass, quartz, Si and Si/SiO_2 substrates by radio frequency (rf) magnetron sputtering. The surface morphological, structural and electrical characterization of the films was done by atomic force microscopy (AFM), x-ray diffraction (XRD), micro-Raman spectroscopy and four-point probe resistance measurements. The main interest of this study is to understand the effect of film thickness and temperature of preparation on the RuO_2 thin film properties.

3.2 Experimental

RuO_2 thin films were deposited by rf magnetron sputtering in a Von Ardenne LS 500 S vacuum chamber with a PPS-90 cathode. A sintered and stoichiometric RuO_2 target (purity 99.99%, 90 mm diam.) was sputtered with an rf power of 100 W in an Ar plasma at a pressure of $1.2x10^{-2}$ mbar. The sputter chamber was initially pumped down to $3.5x10^{-6}$ mbar. The substrate temperatures ranged from room temperature (R.T) to 700°C. Samples prepared at R.T. were annealed in air at temperatures from 200 to 400°C. The substrates used in this experiments are glass, quartz, and p-type Si(100) wafer substrates of different sizes with and without oxidized surfaces. They were cleaned in an ultrasonic bath and later with diethyl ether. The thickness of the films ranges from about 50 to 700 nm.

The thickness of the RuO_2 thin films was determined with a profilometer (Tencor Alpha-Step 500); the structure was determined with a Philips 1710 x-ray diffractometer with Co$L\alpha$ (1.7902Å) radiation; the surface morphology was examined by atomic force microscopy (AFM) in contact mode (Auto-Probe CP Research); the resistivity was determined with a four-point probe. Micro-Raman measurements were performed at room temperature with a Jobin Yvon's LabSpec spectrometer with a magnification of 100 and a resolution of 2 cm^{-1}, using the 514.5 nm line of an argon ion laser as the excitation source with a laser output power of 45 mW.

3.3 Results and discussion

3.3.1 Structural and morphological characterization

Figs. 3.1a to d show x-ray diffractograms of our samples. The position of the reflexes of the tetragonal rutile structure with the lattice parameters of a = 4.50 Å and c = 3.05 Å obtained from the powder diffraction file (PDF 40-1290) is indicated by vertical dashed lines. All observed peaks of the RuO_2 films are close to these positions.

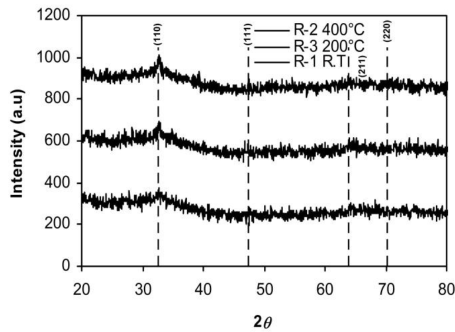

(a)

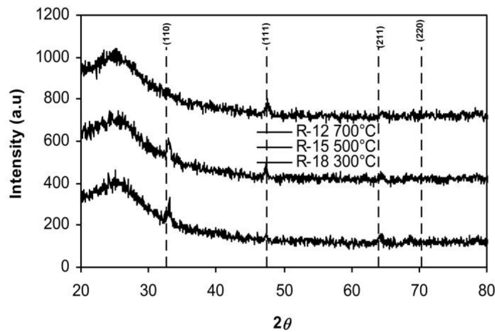

(b)

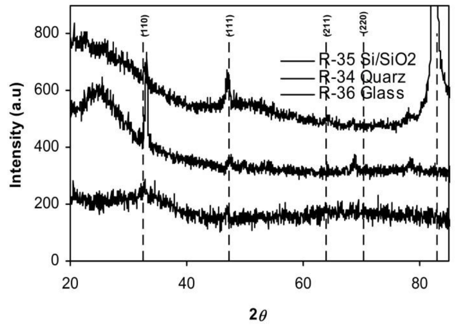

(c)

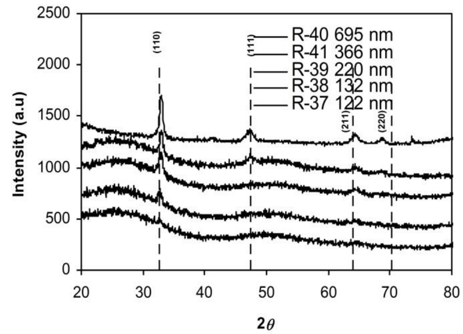

(d)

Figs. 3.1a to d show x-ray diffractograms of RuO_2 thin films: (a) Films (~ 100 nm) deposited on glass substrates at R.T. and annealed at different temperatures, (b) Films (~70 nm) deposited on quartz substrates at different temperatures, (c) Films (~50 nm) deposited on different substrates at 540°C substrate temperature, (d) Films deposited at R.T on Si substrates later annealed at various temperatures.

Fig. 3.1(a) shows the x-ray diffractograms of RuO_2 thin films deposited on glass substrates at R.T with the same thickness of about 100 nm and post-annealed at different

temperatures. The as-deposited film is amorphous and the annealed films are showing a small increase in crystallinity. With increasing the annealing temperature, the (110) and (211) peak appear.

Fig. 3.1(b) represents the films deposited on quartz at different substrate temperatures with the same thickness of about 70 nm. The broad maximum around 25° is due to the quartz substrate. At low temperature (300°C) only the (110) peak appear. With increasing the substrate temperature, the (200) peak intensity increases. At 700°C the (110) peak disappears and only the (200) peak exists. This result is consistent with the result of Lim et al [20], where at high substrate temperatures the (200) peak is predominant and the (110) peak intensity becomes weak.

Fig. 3.1(c) represents films deposited on different substrates at the same temperature (540°C) and with the same thickness (about 50 nm). It clearly shows that the crystallinity of the films depends on the type of the substrate. The RuO_2 film on the glass substrate is exhibits the smallest peaks. Films deposited on quartz and Si/SiO_2 substrates are more crystallized. On the quartz substrate, the main peak is (110). On the Si/SiO_2 substrate, the (110) peak becomes weaker and the (200) peak emerges. The strong peak at 84° is due to the Si substrate.

The diffractograms of the RuO_2 thin films with various thicknesses deposited on Si substrates at R.T and annealed at 400°C are shown in Fig. 3.1(d).

Our results are consistent with previously published data [21]. In fact, Jia et al. [22] reported that the RuO_2 thin films are (*h*00) oriented as long as the deposition temperature is maintained in the range of 400-700°C. They also observed that for a deposition temperature between 200-400°C the RuO_2 thin films show polycrystalline nature with (200) and (110) preferred orientation.

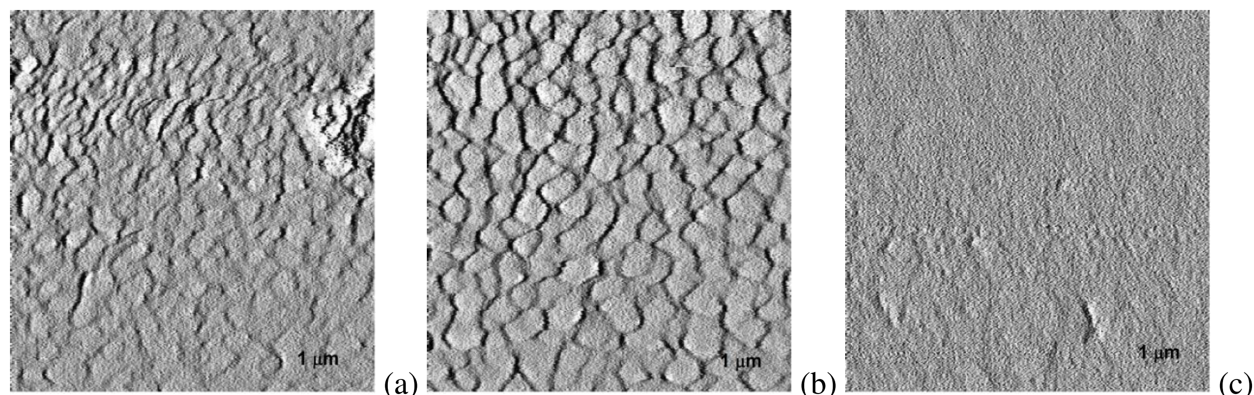

Figs. 3.2a to c show the surface morphology of RuO_2 thin films: (a) and (b) film (~70 nm) deposited on quartz substrate at 300 and 700°C substrate temperatures, respectively (c) film (~50 nm) deposited on Si/SiO_2 substrate at 540 °C.

Figs. 3.2(a) and (b) show the surface morphology of the 70 nm thick RuO_2 films deposited at different substrate temperatures onto quartz substrates. The film deposited at 700°C shows the largest grains (~140 nm) (Fig. 3.2(b)). The film deposited at 300°C shows smaller grains (~55 nm). Both films show similar surface roughness of about 7 nm. From the XRD results we know that at 300°C and 700°C the grains have (110) and (200) preferred orientation, respectively. Fig. 3.2(c) shows a 50 nm thick film deposited on a Si/SiO_2 substrate. The film is very smooth (surface roughness 2.5 nm) and contains very small grains (~30 nm).

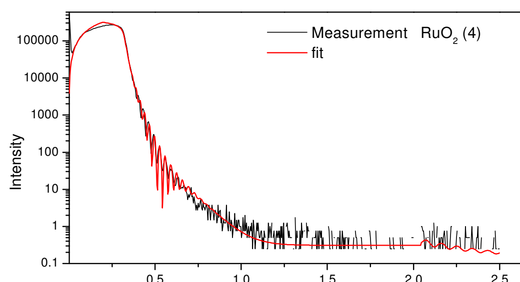

Fig. 3.3 show the XRR curve with simulation (dashed line, in color (red)) of the R-4 sample

Sample	Preparation conditions	XRR thickness(nm)	XRR roughness(nm)	XRR density(g/m^3)
RuO2 -4	Ann. 300°C	110	3	5.54
RuO2-5	R.T	97	3	5.044
RuO2-7	O_2=5 sccm	82	6	5.59
RuO2-13	T_{sub}= 700°C	69	5	6.76
RuO2-19	T_{sub}=300°C	150	6	6.07

Table 3.1 XRR parameters

X-ray reflectivity (XRR) measurements were carried out for five samples. An example is given in Fig. 3.3. The results are summarized in Table 3.1. The thicknesses obtained from these measurements are within 10% of the thickness determined with profilometry. The density of the films calculated from the XRR is always smaller than the crystalline density of 7.06 g/cm³. The smallest packing density (0.72) is observed for the film deposited at room temperature. Annealing at 300°C (film R-4) increases the packing density to 0.78. The biggest packing density (0.96) is obtained for the film deposited at 700°C.

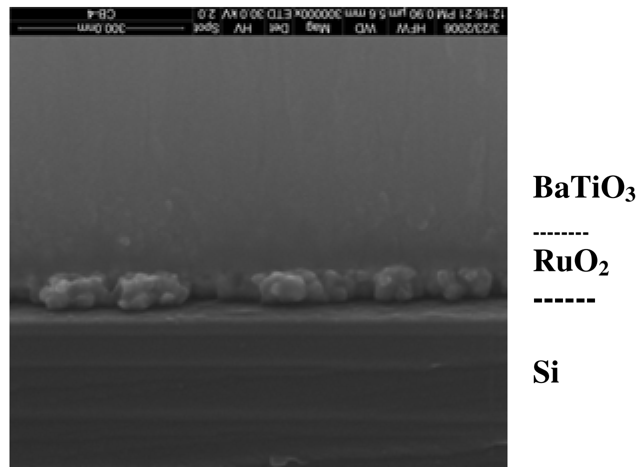

Fig. 3.4 Cross-sectional SEM of $BaTiO_3$ capacitor with RuO_2 electrodes

Fig. 3.4 shows the cross section of a $BaTiO_3$ capacitor with RuO_2 electrodes. It clearly shows that the film consists of separate grains that are only loosely coupled; such grain growth was also observed by Maiwa et al. [23] on Si/SiO_2 substrate. This is consistent with the low density observed in XRR.

3.3.2 *Electrical properties*

Electrical characterization was carried out by means of the four-point probe method at room temperature. The resistivities of the films are tabulated in Table 3.2. They are plotted as a function of temperature in Fig. 3.5.

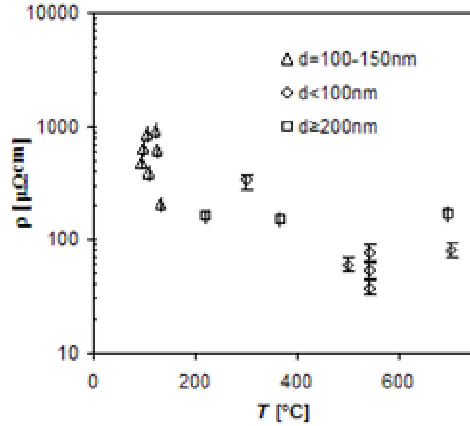

Fig. 3.5 Resistivity vs. temperature for different thickness films

	Sample	Substrate	*T* [°C]	*t* [nm]	ρ [μΩcm]
Series I	R-5	Glass	R.T	105	861
	R-1	Glass	R.T	98	643
	R-2	Glass	Ann. 200	95	489
	R-4	Glass	Ann.300	110	499
	R-3	Glass	Ann.400	107	389
Series II	R-34	Quartz	540	53	38
	R-35	Si/SiO_2	540	57	54
	R-36	Glass	540	55	77
Series III	R-18	Quartz	300	78	334
	R-15	Quartz	500	65	61
	R-12	Quartz	700	62	81
Series IV	R-37	Si	Ann.200	122	928 (232 Ann.400°C)
	R-38	Si	Ann.300	132	209 (137 Ann.400°C)
	R-39	Si	Ann.400	220	180
	R-41	Si	Ann.400	366	152
	R-40	Si	Ann.400	695	170

Table 3.2 Parameters of RuO_2 thin films

A high resistivity (861 μΩcm) is observed for the sample of Series I prepared at room temperature. With increase of the annealing temperature up to 400°C, the resistivity reaches the lower value of 390 μΩcm. Films deposited on various substrates (Series II) with the same

thickness show different resistivity values. They are lower for the films on the quartz substrate (38 μΩcm) than for films on glass substrates (77 μΩcm). For Series III samples, the resistivity decreases drastically from 334 to 80 μΩcm with increasing the substrate temperature from 300 to 700°C. Series IV samples were deposited on Si at R.T with different thicknesses. The first two samples were annealed at 200 and 300°C, and later again annealed at 400°C. They exhibit 230 and 140 μΩcm, respectively. The other samples were annealed at 400°C exhibiting about 170 μΩcm.

Fig. 3.5 clearly shows that the resistivity depends mainly on the substrate or annealing temperature, the thickness effect is comparably small. The resistivity of the film with a packing density of 0.96 is about 80 μΩcm. The minimum resistivity of about 40 μΩcm, equal to the bulk resistivity [14], is observed for the samples deposited at 540°C on quartz. The experimental error of the resistance measurement is about 10%. That of the thickness determination is 10 to 15 %.

These results agree well with others' results [20,24,25,26]. Our results are well consisted with literature values [5,7,13], which were deposited or annealed 300°C and above. Lee et al. [27] also observed that, with increasing the temperature of annealing in oxygen from 300°C to 700°C, the resistivity of RuO_2 thin films deposited on Si/SiO_2 decreases from 270 to 90 μΩcm.

The decrease of the resistivity with increase of the substrate or annealing temperature is thought to be caused by the improvement of crystallinity and ultimately increase of the average grain size [28].

3.3.3 Raman spectroscopy study

Micro-Raman spectroscopy was used to extract microstructural information about the RuO_2 thin films. Figures 3.6 (a), (b) and (c), show the Raman spectra of the RuO_2 thin films together with the positions of the single crystal modes (dashed vertical lines) in the range of 450–800 cm^{-1}. Three Raman modes, identified as E_g, A_{1g}, and, B_{2g} are observed at ~528, 646 and 716 cm^{-1}, respectively. The thin films on quartz and glass exhibit an about 20 cm^{-1} red-shift in peak position, a strong signal at ~510 cm^{-1} on Si/SiO_2 is from substrate. Red-shifts in the Raman peak

positions for RuO_2 thin films relative to those of single-crystalline RuO_2 are well known, with a broadening of the peaks as the films become less ordered [29].

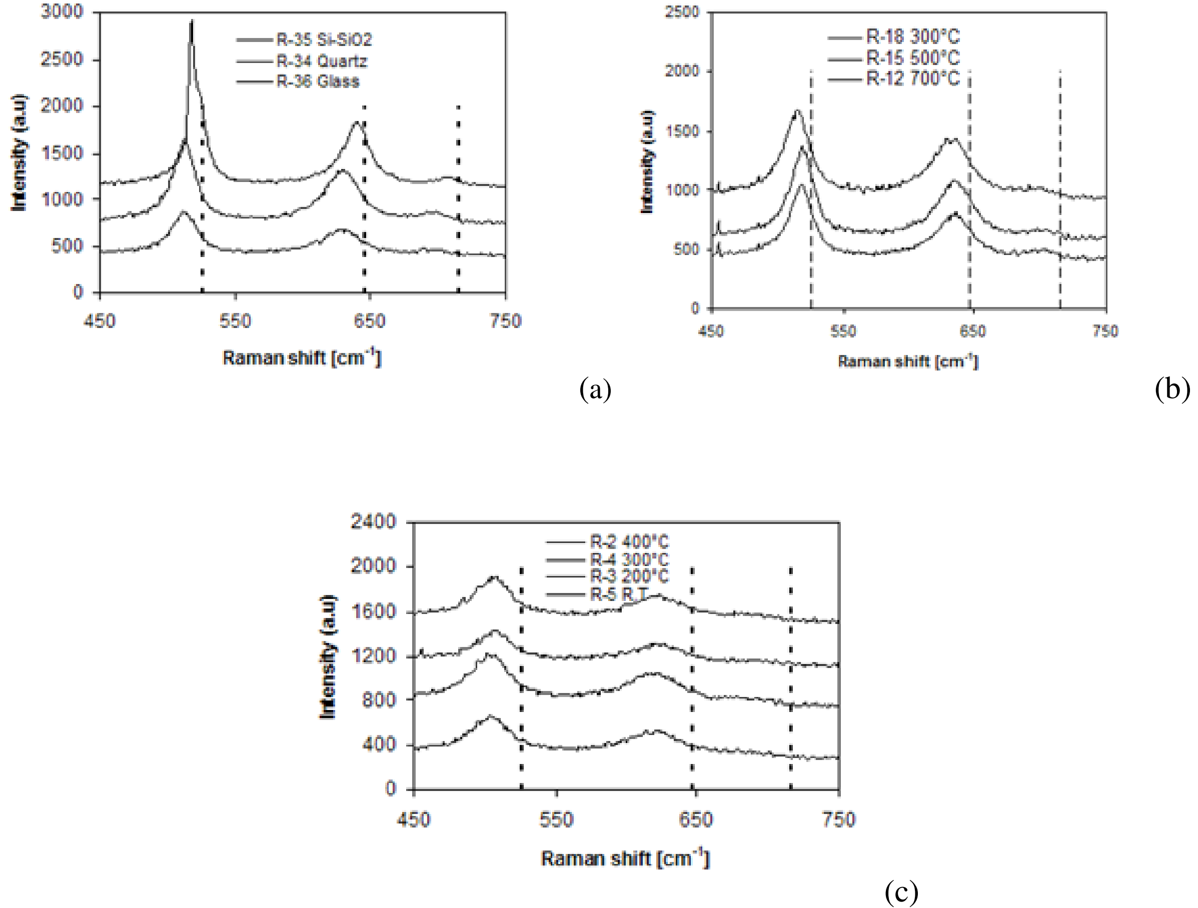

Fig. 3.6a to c Raman spectra of RuO2 thin films: (a) Films (~50 nm) deposited on different substrates at 540°C substrate temperature (b) Films (~70 nm) deposited on quartz substrates at different temperatures, (c) Films (~ 100 nm) deposited on glass substrates at R.T. and annealed at different temperatures.

It is clear that the Raman shift of the RuO_2 film on the Si substrate is less. Liao et al. [30] also observed that the Raman shift for films on Si is less than for films on fused silica. The possible mechanisms for the changes in the Raman features may result from disorder effects induced by structural defects and grain boundaries or/and by strain [31]. This occurs in films grown on substrates with different lattice constants or different thermal expansion coefficients. However, the lattice parameter and volume thermal expansion coefficient of Si are comparable with RuO_2.

3.4 Integration into capacitor structure: Issues to be considered

We have tried to integrate RuO_2 electrodes into capacitor structure. In this process, we noticed several issues, which will be useful to the future research in order to understand and overcome these problems. When, we deposited RuO_2 single layer thin films from R.T up to 700°C substrate temperatures, films shown very good adhesion and film properties. But, when the dielectric films deposited on the RuO_2 layers there was peeling off the films from the substrate for several deposition conditions: when the RuO_2 bottom electrode deposited at 540°C, and the dielectric films deposited at 450°C with no additional oxygen, there was no problem, films are perfect. But, when the dielectric film deposited with additional oxygen, then the films are peeled off from the substrate. When films deposited above this temperature with or without additional oxygen there was no problem. Maiwa et al. also observed such peeled off problems, when they deposited RuO_2 films on MgO (100) substrate; it was because of poor adhesion on the substrate. We observed that medium temperature range (about 550°C) is sufficient to get low resistivity with good adhesion properties in order to integrate into capacitor structure. Such observations also revealed for other deposition techniques, such as PLD [Kaga et al.] and reactive sputtering [Jia et al.].

3.5 Conclusions

RuO_2 thin films have been deposited at different substrate temperatures on various substrates by radio-frequency (rf) magnetron sputtering and were later annealed at different temperatures. Films deposited at higher temperatures show larger grain size (140 nm) with (200) preferred orientation. Those deposited at lower substrate temperatures show smaller grains (~55 nm) with (110) preferred orientation.

The resistivity of the films is mainly determined by the deposition and annealing temperature. The effect of film thickness is smaller. The resistivity decreases only slightly with increasing film thickness. Films deposited at room temperature on glass substrate show higher resistivity (861 μΩcm) than films annealed at higher temperatures (390 μΩcm, annealed at 400°C). The minimum resistivity of a 50 nm thick film is about 40 μΩcm observed for the

samples deposited at 540°C on quartz substrates. The micro-Raman investigation indicates that the film deposited onto an oxidized Si substrate is nearly strain-free.

References

[1] G. R. Fox, S. Trolier-McKinstry and S. B. Krupanidhi *J. Mater. Res.* **10** 1508 (1995)

[2] T. Sakuma, S. Yamamichi, S. Matsubara, H. Yamaguchi and Y. Miyasaka *Appl. Phys. Lett.* **57** (1990) 2431

[3] Joint Committee on Diffraction Standard (JCPDS)-International Center for Diffraction Data (ICDD), Powder Diffraction File, # 40-1290

[4] Y. T. Kim, C. W. Lee and S. K. Kwak *Appl. Phys. Lett.* **67** 807 (1995)

[5] K. Sakiyama, S. Onishi, K. Ishihara and K. Orita *J. Electrochem. Soc.* **140** 834 (1993)

[6] E. Kolawa *Thin Solid Films* **173** 217 (1989)

[7] L. Krusin-Elbaum, M. Wittmer and D. S. Yee *Appl. Phys. Lett*. **50** 1879 (1987)

[8] T. Kawahara, M. Yamamuka, A. Yuuki and K. Ono *Jpn. J. Appl. Phys*. **35** 4880 (1996)

[9] D. P. Vijay and S. B. Desu *J. Electrochem. Soc.* **140** 2640 (1993)

[10] M. Wittmer *J. Vac. Sci. Technol.* **A2** 273 (1984)

[11] L. Krusin-Elbaum and M. Wittmer *J. Electrochem. Soc.* **135** 2610 (1988)

[12] E. Kolawa, F. C. T. So, E. T. –S. Pan and M. –A. Nicolet *Appl. Phys. Lett.* **50** 854 (1987)

[13] K. M. Glassford and J. R. Chelikowsky *Phys. Rev. B* **47** 1732 (1993)

[14] W. D. Ryden, A. W. Lawson and C. C. Sartain *Phys. Rev. B* **1** 1494 (1970)

[15] L. A. Burstill, I. M. Reaney, D. P. Vijay and S. B. Desu *J. Appl. Phys* **75** 1521 (1994)

[16] Q. X. Jia, S. G. Song, X. D. Wu, J. H. Cho, S. R. Foltyn, A. T. Findikoglu, and J. L. Smith *Appl. Phys. Lett.* **68** 1069 (1996)

[17] H. N. Al-Shareef, K. R. Bellur, O. Auciello and A. I. Kingon *Thin Solid Films* **256** 73 (1995)

[18] W. C. Shin and S. G. Yoon *J. Electrochem. Soc*. **144** 1055 (1997)

[19] J. G. Lee, Y. T. Kim and S. K. Min *J. Appl. Phys.* **77** 5473 (1995)

[20] W. T. Lim, K. R. Cho and C. H. Lee *Thin Solid Films* **348** 56 (1999)

[21] J. Malek, A. Watanabe and T. Mitsuhashi *Thermochim. Acta* **282/283** 131 (1996)

[22] Q. X. Jia, X. D. Wu, S. R. Foltyn. A. T. Findikoglu, P. Tiwari, J. P. Zheng and T. R. Jow *Appl. Phys. Lett.* **67** 1677 (1995)

[23] H. Maiwa, N. Ichinose and K. Okazaki *Jpn. J. Appl. Phy.* **33** 5223 (1994)

[24] H. Luan, C. –H Lee and D. –L. Kwong *Appl. Phys. Lett.* **78** 1134 (2001)

[25] H. Zhong, G. Heuss and V. Misra *IEEE Electron Device Lett.* **21** 593 (2000)

[26] Y. Kaga, Y. Abe, H. Yanagisawa and K. Sasaki *Jpn. J. Appl. Phys.* **37** 3457 (1998)

[27] J. S. Lee, H. J. Kwon, Y. W. Jeong, H. H. Kim and C. Y. Kim *J. Mater. Res.* **11** 2681 (1997)

[28] T. S. Kalkur and Y. C. Lu *Thin Solid Films* **205** 266 (1991)

[29] S. Bhaskar, P. S. Dobal, S. B. Majumder and R. S. Katiyar *J. Appl. Phys.* **89** 2987 (2001)

[30] P. C. Liao, S. Y. Mar, W. S. Ho, Y. S. Huang and K. K. Tiong *Thin Solid Films* **287** 74 (1996)

[31] S. Nakashima and M. Hangyo *IEEE J. Quantum Electron.,* **QE-25** 965 (1989)

4. Impedance spectroscopy study of $RuO_2/SrTiO_3$ thin film capacitors prepared by radio-frequency magnetron sputtering[2]

Abstract

Thin film capacitors of $SrTiO_3$ with RuO_2 top and bottom electrodes on Si substrates were prepared by radio-frequency magnetron sputtering at substrate temperatures 500 and 700 °C and at various oxygen partial pressures. The thickness of the dielectric layer was varied between 200 and 900 nm. The impedance spectra of these samples could be interpreted with an equivalent circuit comprising a resistance and two RC-parallel elements in series. The dielectric permittivity ε_r of the bulk grains, as extracted from the high-frequency semicircle in the Cole-Cole plot, was in the range 300 to 600. High oxygen contents lead to high values of ε_r but also increase the grain boundary resistance.

---

[2] Accepted in *Mater. Sci. Eng. B* (doi:10.1016/j.mseb.2006.03.013) by Y.K. Vayunandana Reddy, D. Mergel and W. Osswald

4.1 Introduction

Thin films of large dielectric constant, low dielectric loss, and exhibiting good high frequency characteristics such as strontium titanate, $SrTiO_3$, are promising candidates for many applications ranging from capacitors in memory devices [1] to monolithic microwave integrated circuits [2]. The dielectric permittivity of $SrTiO_3$ thin films is significantly smaller than that of the bulk form. Various explanations have been proposed for this effect including dead-layer effects, interfacial reactions, and film stress [3-5]. Several methods are used to deposit $SrTiO_3$ thin films: pulsed laser deposition [6], sol-gel technique [7], plasma enhanced metal-organic chemical vapor deposition (MOCVD) [8], radio frequency (rf) sputtering [9], electron cyclotron resonance (ECR) sputtering [10] and rf magnetron sputtering [11,12].

$SrTiO_3$ is an incipient ferroelectric [13-15]. Bulk $SrTiO_3$ has cubic symmetry between room temperature and ~105 K. Below this temperature it undergoes a structural transition (but not a ferroelectric one) to a tetragonal phase. Above this phase transformation temperature, the dielectric permittivity follows a Curie-Weiss type law with a Curie-Weiss temperature of ~35 K [16]. Single crystals and polycrystalline ceramics of $SrTiO_3$ exhibit dielectric constants of ~300 and 250, respectively [17,18]. The dielectric properties and the Curie-Weiss behavior of perovskite films are strongly affected by film non-stoichiometry, film-electrode interfaces and film stress in the paraelectric phase [19,20].

The dielectric permittivity of ferroelectric thin films often shows pronounced thickness dependence. The origin of the thickness-dependent behavior is presently not well understood. It has been explained with low-permittivity layers at the electrode interfaces that are connected in series with the bulk of the film [21,22]. Several other mechanisms have been proposed [5,23]. They include incomplete screening of the polarization by the electrodes, interfacial contamination, and intrinsic dead layers because of their interfacial discontinuity.

Platinum (Pt) has been used as an electrode material for a long time for ferroelectric capacitors [24]. However, Pt has some drawbacks like adhesion, poor etching characteristics and interface-related issues. These problems forced to look for alternative electrode materials

[25,26]. Some of the electrode materials have been investigated for the fabrication of perovskite capacitors at high temperature in oxygen atmosphere. Among them, RuO_2, a conductive oxide, is a promising candidate as it shows low resistivity, excellent diffusion barrier effect, and high thermal stability [27,28].

A limited study is done so far on the thickness dependence of the dielectric properties of $SrTiO_3$ [29-32]. In this study, thickness dependent dielectric properties of $SrTiO_3$ thin film are investigated using conventional rf magnetron sputtering on RuO_2/SiO_2/p-Si(100) substrates. To investigate the thin film properties as a function of the deposition parameters, substrate temperature and oxygen partial pressure were varied. The $SrTiO_3$ thin films were characterized by x-ray diffraction (XRD), and profilometry. Thin film capacitors were fabricated using RuO_2 as the top and the bottom electrodes and investigated by impedance spectroscopy.

4.2 Experimental

$SrTiO_3$ thin films were deposited using rf magnetron sputtering (Von Ardenne LS 500 S). A sintered and stoichiometric $SrTiO_3$ target (purity 99.99% , rf power 300 W) was sputtered in an Ar/O_2 plasma to deposit the films at 500°C and 700°C substrate temperature. High purity (5N) Ar (50 sccm) and O_2 (2.5 to 10 sccm) gases were used. Circular p-type Si(100) wafer substrates of 25 mm diam. and about 0.5 mm thickness were cleaned in an ultrasonic bath. A SiO_2 layer was grown by thermal oxidation.

The capacitor structure comprised RuO_2 layers as bottom (50 nm) and top (30 nm) electrodes. They are deposited by rf magnetron sputtering of a RuO_2 target (purity 99.99%, Ar 50 sccm, rf power 75 W) at 540°C and room temperature, respectively. The area of the top electrode is 7 mm^2. The sputter chamber was pumped down to $3.5x10^{-6}$ mbar, and the $Ar+O_2$ pressure during deposition was $1.2x10^{-2}$ mbar. The thickness of the films ranges from around 200 to 900 nm.

The thickness of the $SrTiO_3$ thin films was determined with a profilometer (Dektak 6M Stylus). Structure determination was carried out by x-ray diffraction (Philips 1710 x-ray

diffractometer) with Co $L\alpha$ (1.7902 Å) radiation. A cross sectional micrograph was obtained by scanning electron microscopy (SEM) with a FEI Quanta 400 FEG. Rutherford backscattering (RBS) was performed with 2 MeV He-ions, in order to obtain the chemical composition.

The complex impedance was measured using a Solartron Schlumberger SI 1260 impedance/gain-phase analyzer. The temperature and frequency dependent dielectric properties were measured from 20 to 200°C and 10 Hz to 10 MHz, respectively.

Sample	p [mbar]	T_{sub}	O_2 %	d [nm]	ε_r			E_σ [meV]
					at 100 Hz	10 KHz	RC_p	
CS-6	$3.6\text{X}10^{-2}$	700°C	5	220	246	194	296	61
CS-8	$2.4\text{X}10^{-2}$	700°C	5	360	211	184	277	120
CS-4	$4.0\text{X}10^{-2}$	700°C	5	960	320	267	-	-
CS-11	$2.4\text{X}10^{-2}$	700°C	10	560	199	164	300	14
CS-12	$3.0\text{X}10^{-2}$	700°C	20	400	11034	354	609	21
CS-13	$2.2\text{X}10^{-2}$	500°C	10	405	10916	189	575	5

Table 4.1 The deposition parameters, dielectric permittivity and activation energies for all investigated capacitors, ε_r values are obtained at room temperature.

In Table 4.1, the deposition parameters of the six capacitors are tabulated together with some results of the impedance spectroscopy.

4.3 Results and discussion

4.3.1 Structural analysis

The composition of the samples, as obtained with RBS, was stoichiometric within the experimental error (about 2%).

XRD patterns of the thin film capacitors, $RuO_2/SrTiO_3/RuO_2/SiO_2$/p-Si(substrate) with various thickness of the dielectric layer are shown in Fig. 4.1.

The diffractograms in Figs. 4.1a and b represent films with thicknesses varying from 220 nm to 960 nm. This is less than the extinction length of x-rays with λ = 1.7902 Å. We therefore have to normalize the intensities. This has been done in the way described in [50] with a mass

absorption coefficient of 168 cm²/g of $SrTiO_3$ as calculated from standard tables and a mass density of 5.12 g/cm³. Different peak heights should now represent different textures of crystalline orientations.

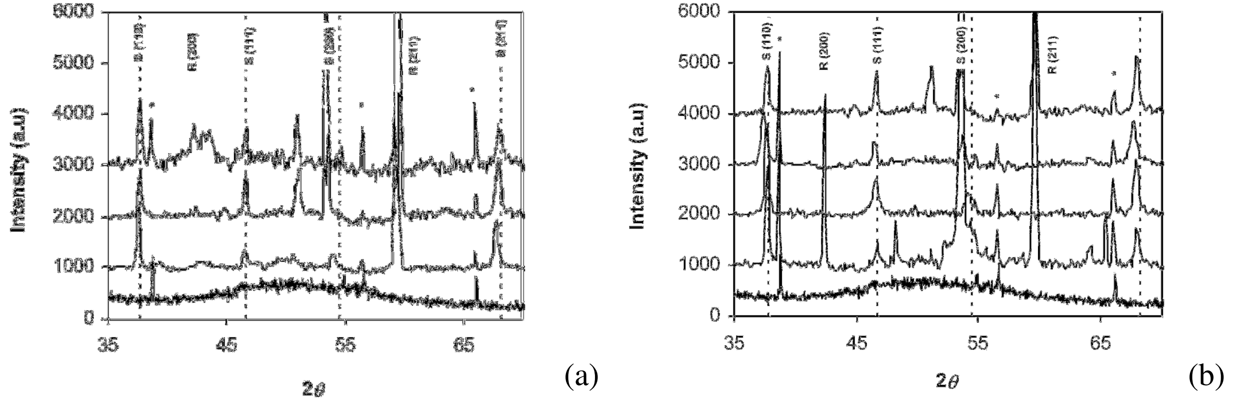

Fig. 4.1 XRD patterns of STO thin film capacitors normalized with respect to film thickness. The vertical dashed lines represent $SrTiO_3$ (coded as S) peaks and RuO_2 peaks (coded as R). The bottom diffractograms represents the uncoated Si substrate. Its peaks are marked with *. Fig. 4.1a. Capacitors prepared at 700°C with 5% oxygen. Top to bottom: CS-6 (220 nm), CS-8 (360 nm), CS-4 (960 nm). Fig. 4.1b. Capacitors prepared at different oxygen partial pressures. From top to bottom: CS-8 (5%), CS-11 (10%), CS-12 (20%), CS-13 (10%) all prepared at 700°C except CS-13 that was prepared at 500°C.

Fig. 4.1a displays diffractograms of the capacitors with different thickness of the $SrTiO_3$ layer prepared at 700°C with 5% oxygen in the sputter gas together with the diffractograms of the Si substrate.

The (110), (111) and (211) reflexes of $SrTiO_3$ are present in all samples. (110) and (211) have approximately the same size for all thicknesses. (111) is considerably smaller in the thicker film indicating a suppression of grains with this orientation in films thicker than about 400 nm. A similar phenomenon was observed for In_2O_3:Sn films prepared earlier in the same sputter chamber [40]. We observe further that the peaks already observed for the Si substrate decrease with increasing thickness as expected because the absorption of the x-rays increases. More peaks than those mentioned before are observed in the thinnest film. They are attributed to Ru-oxide phases, especially the strong peak at $2\theta = 54°$ which is (110) of RuO_2. They are suppressed in the thicker films.

Fig. 4.1b displays diffractograms of the capacitors prepared at various deposition parameters (5 to 20% O_2 in the sputter gas and substrate temperatures of 500°C and 700°C). There is no strong influence of the oxygen partial pressure on (211) and (111) but (110) increases with increasing O_2 and is sharper when the film is deposited at lower temperature.

We observe a shift of the (200) and (211) peaks towards smaller 2θ values with respect to the single crystalline positions, corresponding to larger lattice constants. The lattice distortion, $(d_{exp} – d_{ideal})/d_{ideal}$ [51], is less than 1% for (211) but more important for (200) where values up to 2% are observed. The smallest (200) distortion is observed for the thickest film CS-4 (0.8%) and that prepared with 20% O_2 (CS-12). We shall see later that CS-12 exhibits the largest ε_r value for the bulk grain.

Lattice distortion of this size have been observed in In_2O_3:Sn films and have been attributed to the incorporation of oxygen into interstitial positions of the lattice [51]. It was shown that a correlation exists between the lattice distortion and optical and electrical properties. This could also be the case for $SrTiO_3$ films. However, a reliable interpretation is not yet possible because there are not enough experimental data. From the discussion of the XRD results we conclude that (111) is suppressed with increasing film thickness and (200) = (100) as well as (110) are sensitive to the preparation conditions.

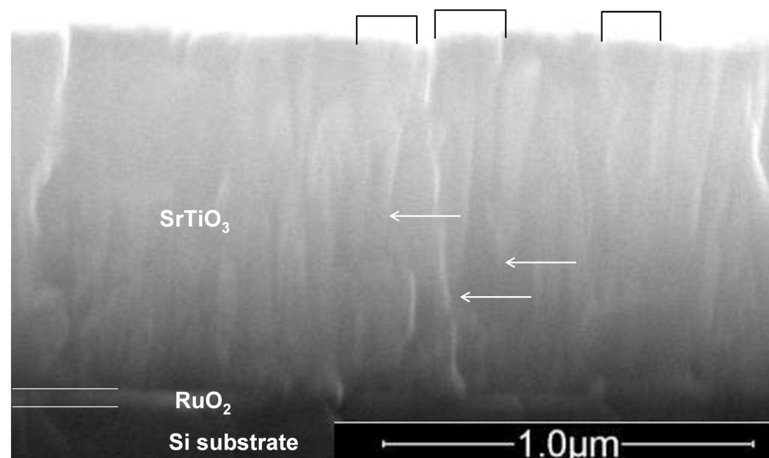

Fig. 4.2 Cross-sectional SEM of sample CS-4 prepared at 700°C with 5% O_2, thickness 960 nm.

Fig. 4.2 shows a cross section of sample CS-4. We see the RuO_2 bottom electrode with a thickness of about 50 nm and the $SrTiO_3$ film with a thickness about 960 nm. These thicknesses are consistent with the values obtained by profilometry. The $SrTiO_3$ film shows a pronounced columnar growth. This kind of growth is often observed for dielectric films prepared at higher substrate temperatures.

At some places, indicated by white arrows, the beginning of selective grain growth can be observed. Some grains grow into cone-shaped columns inhibiting other grains to grow. This occurs at a distance of 300 to 600 nm from the bottom electrode. The structure scale on the surface is indicated by brackets. It is well known for many materials in thin film form that grains with smaller defect density grow more easily than films with higher defect density. We therefore conclude that this type of grain growth in our films is an indication that films thicker than the above mentioned range become more perfect with a smaller defect density.

4.3.2 Impedance spectroscopy

4.3.2.1 Simulation with equivalent circuits

The electrical properties were investigated by means of impedance spectroscopy from 10 Hz to 10 MHz performed at an amplitude of 0.1 V by a Solartron Schlumberger SI 1260 Impedance/gain-phase analyzer.

The use of impedance spectroscopy to characterize bulk grain, grain boundary and electrode interface contributions by exhibiting successive semicircles (often with some distortion) of the impedance (real and imaginary part) in the complex plane, is well established [33,34]. A high frequency semicircle originates from the bulk conduction and dielectric processes; a low-frequency semicircle is due to ion and electron transfer at the surface contacting the electrode, and an intermediate-frequency semicircle provides information on the grain boundary and/or impurity-phase impedance. All these contributions vary with temperature, and, for a given frequency range of measurement, they may not all be found.

The complex impedance spectra are usually analyzed in terms of the complex formalism for the impedance, $Z^* = Z' + jZ''$. In general, for a single crystal, the values of resistance, R, and capacitance, C, can be analyzed by an equivalent circuit of one element with parallel R and C (RC_p) element. This RC_p element gives rise to one semicircular arc in the complex plane and has intercepts on the Z' axis at zero and R. Thus, C can be calculated with the relationship $\omega_{max}RC = 1$, where $\omega_{max}=2\pi f_{max}$. The characteristic frequency f_{max} is the frequency at the arc maximum. For polycrystalline thin films containing grain boundary and electrode interfacial layers, more than one RC_p element can be connected in series.

All our experimental impedance spectra could be explained with the model depicted in Fig. 4.3a, a series of a resistance and two RC_p elements. We shall interpret it by the electrode resistance, the grain boundary and the grain impedance.

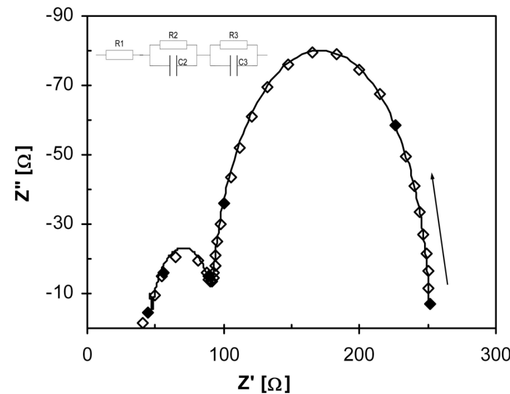

(a)

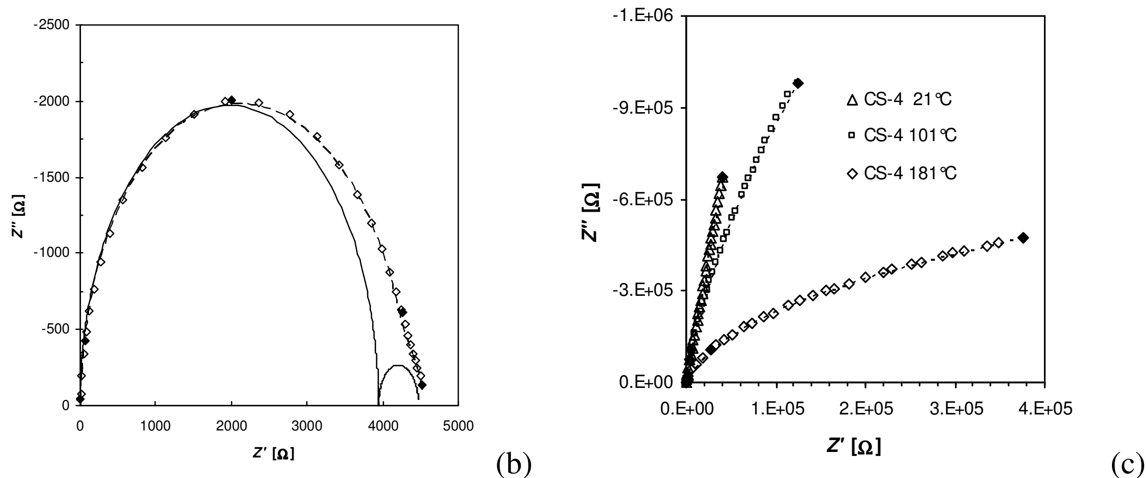

Fig. 4.3 Impedance in the complex plane. Experimental data together with simulated curves. The full diamonds correspond to the decades starting at 10 Hz and the arrow indicates the direction of increasing frequency. Fig. 4.3a. Sample CS-13 prepared at 500°C with 10% O_2. The inset shows the equivalent circuit of one resistance and two RC elements in series used for the simulation. Fig. 4.3b. Data of sample CS-6 prepared at 700°C with 5% O_2 with the thickness 220 nm with deconvolution and simulated curve (dashed line). Fig. 4.3c. Sample CS-4 prepared at 700°C with 5% O_2 and a thickness of 960 nm

Figs. 4.3a, b and c show Z'-Z" plots of the impedance of three capacitors together with the simulations.

Fig. 4.3a shows the Cole-Cole plot of CS-13 with a thickness of 405 nm together with the simulated spectrum. The arrow marks indicate the directions of increasing frequency. The deconvolution into two semicircles is uncritical for CS-13. The spectrum shows two clearly separated semicircles and it is clear that the impedance does not tend towards the zero in the complex plane. The semicircle attributed to the grain boundaries is relatively large. The sample was deposited at 500°C with a relatively high oxygen flow (5 sccm), conditions that might lead to high grain boundary resistivity. Fig. 4.3b shows the results for capacitor CS-6 with a thickness of 220 nm, prepared at 700°C. Here, the low-frequency semicircle is hidden under the high-frequency semicircle. The deconvolution is shown by the dashed curves.

The impedance spectrum of the sample CS-4 (d = 960 nm) shown in Fig. 4.3c is an exception. It exhibits a very high resistance (0.4 MΩ at 10 MHz for 180°C) and correspondingly very low relaxation frequencies. Therefore, the arc does not touch the real axis at low frequencies.

For CS-4, a good simulation with the equivalent network of Fig. 4.3a is possible, a deconvolution into semicircles is, however, not meaningful. Therefore, we calculate ε_r by means of Eq. (4.2). The data shown in Fig. 3c are more difficult to analyze. We attribute the small semicircle at low frequencies tentatively to grain boundaries. This assumption will be discussed later.

In most impedance investigations on polycrystalline dielectric thin films with perovskite structure and other dielectric compounds, a series of parallel RC- elements are used for the numerical simulation [52,53,54,55]. We also applied this model. The results are shown in Figs. 3a, b and c. The fits to the experimental data are quite good. Nevertheless, some authors think that such equivalent circuits are insufficient and that constant phase elements (Q) instead of capacitors should be used because of the (microstructural, compositional, etc.) inhomogeneity of polycrystalline materials.

Therefore, we repeated all simulations with RQ_p- elements instead of RC_p- elements. The impedance of Q is $A\cdot(i\omega)^{-\alpha}$ instead of $(i\omega C)^{-1}$ for a capacitor. In most cases, we got a perfect fit with values for one semicircle with power $\alpha = 0.94$ to 0.98 for CS-6, 0.93 to 0.99 for CS-8, and for the two semicircles of CS-13: 1.00 for the low-frequency circle and 0.90 to 1.00 for the high-frequency semicircle. We calculated ε_r values from the frequency of the maximum of Z'' of the individual RQ_p-semicircles. These values are within 10% from the values calculated from the RC_p-simulation. Therefore, we shall represent the dielectric permittivity by the average of both values together with their standard deviation in the discussion to follow.

When there is more than one semicircle, we have to decide which one is related to the grain boundary and which to the bulk grain. From the literature it is known that the resistance and the capacitance of the grain boundaries is always larger than that of the bulk grains.

We conclude that the relaxation time $\tau = RC = \rho\varepsilon_r\varepsilon_0$ is larger for the grain boundaries. Consequently, the characteristic frequency $f_g = (2\pi\tau)^{-1}$ is relatively smaller and the semicircle of the grain boundaries occurs at lower frequencies. The grain resistance is determined from the

high-frequency semicircle of the RC_p or RQ_p equivalent circuit. This procedure is well established in the literature. It has been applied in the case of many dielectric and ferroelectric materials [52,53,56,57].

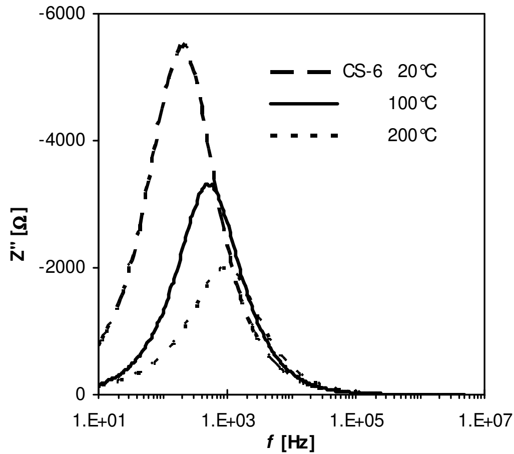

Fig. 4.4 Imaginary part (Z'') of the impedance vs. frequency (f) of sample CS-6 for different measuring temperatures.

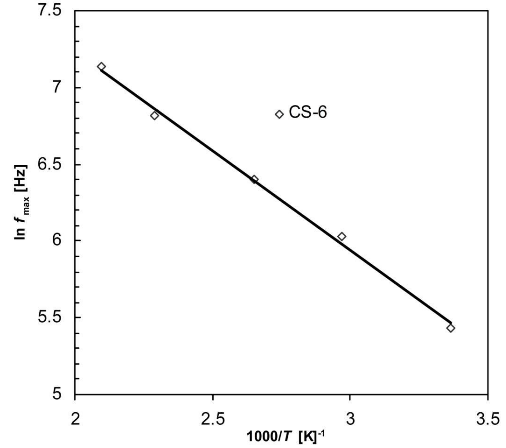

Fig. 4.5 Arrhenius plot, $\ln f_{max}$ vs. $1000/T$ [K^{-1}] for sample CS-6 (700°C, 5% O_2, 220 nm).

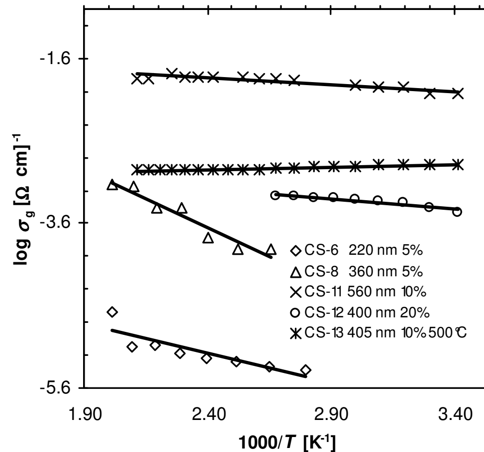

Fig. 4.6 Arrhenius plot of the bulk conductivity of all investigated capacitors (except CS-4), values obtained from the RC simulations.

Fig. 4.4 shows the variation of the imaginary part of the impedance (Z'') of sample CS-6 as a function of frequency at different temperatures for the $SrTiO_3$ thin film with 220 nm thickness. The peak shifts towards higher frequencies as the temperature increases. The magnitude of the imaginary component of the impedance at the peak frequency is also a strongly decreasing function of the temperature. An Arrhenius plot of the peak frequency is given in Fig. 4.5. The data show thermally activated behavior. The corresponding activation energy is 0.11 eV.

The overall resistance of the samples of Figs. 4.3a to c increases by many orders of magnitude with increasing film thickness (4 kΩ for CS-6 220 nm, 40 kΩ for CS-8 360 nm, 500 kΩ for CS-4 960 nm). We attribute this effect to more perfect growth of thicker films. As already mentioned above, a change in growth mode at about 400 nm was observed for In_2O_3:Sn films prepared earlier in the same sputter machine. If our hypothesis for a similar phenomenon in $SrTiO_3$ films proves true, a major task for future technology development should be to improve the growth of films thinner than 400 nm.

We assume that the relatively low resistivity of the thinner films is due to the change in film growth mode at about 300 to 600 nm discussed above. The thinner films exhibit a fine columnar structure with perhaps many conductive paths due to imperfect material. As pointed out in the discussion of Fig. 4.2, the thicker films are characterized by a selective growth of more perfect grains that may block the growth of the conductive paths. In the literature on $BaTiO_3$ ceramics, some groups argue that high conductivity is due to semiconductive behaviour of grain boundaries caused by donor defects [58,59]. We do not have enough experimental data to decide whether such effects can also play a role in our films. More investigations are needed to understand this effect.

4.3.2.2. Properties of bulk grains

Conductivity

The bulk conductivity of $SrTiO_3$ films as evaluated from the RC_p- semicircles attributed to the bulk grains is depicted in the Arrhenius plot of Fig. 4.6. It may be explained by a thermally activated transport of Arrhenius type governed by the relation:

$$\sigma = \sigma_0 \exp\left(-\frac{E_a}{kT}\right) \tag{4.1}$$

where σ_0, E_a, and k represent the pre-exponential factor, the activation energy of the mobile charge carriers and the Boltzmann constant, respectively. As seen in Fig. 4.6, the conductivity increases with increasing film thickness. This indicates improvement of growth with a reduced trap density. The activation energies are shown in Table 4.1. They are comparable to those reported in the literature for various materials: 4 to 11 meV for $SrTiO_3$ [35], 33 to 62 meV for $(Sr,Bi)TiO_3$ [36], 12 meV for $(Sr,Ca)TiO_3$ [37], and 100 meV for TiO_2 [38]. Such small activation energies have been attributed to hopping of electrons between traps generated e.g. by off-center defects.

Dielectric permittivity

The real part of the dielectric permittivity (ε_r) can be calculated with the formula [60, 61]:

$$\varepsilon_r = \frac{-Z''}{(2\pi f C_0)(Z'^2 + Z''^2)} \tag{4.2}$$

The frequency-dependent values calculated with Eq. (2) from three typical spectra can be seen in Fig. 4.7.

As a typical behavior, the dielectric constant is higher at lower frequencies and decreases with increasing frequency. Such behavior has been observed in many MIS systems [39] and various models have been proposed in terms of the frequency dispersion of the permittivity of the insulator film, the presence of a highly resistive interfacial layer or a high density distribution of interface states.

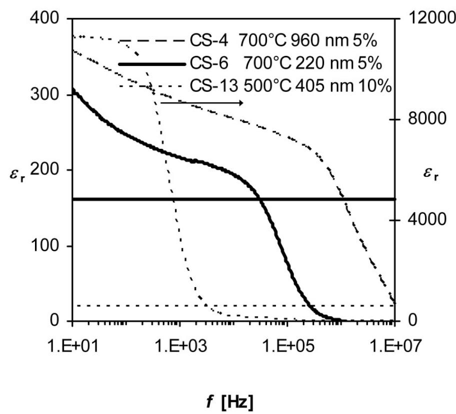

Fig. 4.7 Frequency dependent dielectric permittivity (ε_r) as calculated from Eq. (2). The horizontal lines represent the values obtained for the high-frequency semicircle of the RCp-simulation attributed to the bulk STO grains.

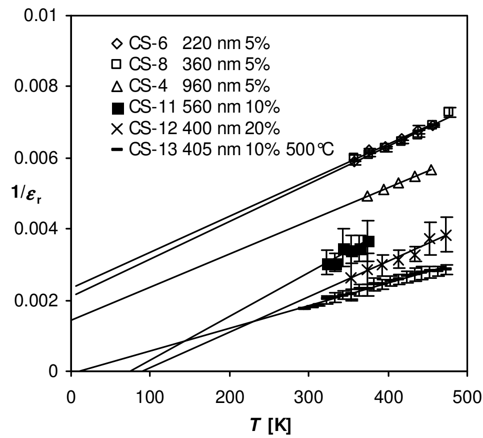

Fig. 4.8 Inverse dielectric permittivity ($1/\varepsilon_r$) vs. temperature. Average of the values obtained from the RQ and RC simulations, with error bars.

Sample CS-13, prepared at the low temperature shows a sharp decrease in the ε_r with the increase in frequency. This can be explained with interfacial polarization, contributions from interfacial polarizability due to the presence of two layers of material of different conductivity. In polycrystalline ceramics, this kind of behavior is commonly observed when the grains are semiconducting and the grain boundaries are insulating. When the resistance of the grain boundaries is much larger than that of the grains then the ε_r calculated from Eq. (4.2) is too large by a factor corresponding to the ratio of the thickness of the grains to that of the grain boundaries.

Around 10 kHz, all spectra exhibit a plateau. According to our model, the RC_p-element of the grains dominates the spectra in this spectral region. The horizontal lines in Fig. 4.7 correspond to the values of ε_r as evaluated from the simulation with the equivalent circuit of Fig. 4.3a. They are tabulated in Table 4.1 together with the values of ε_r calculated from Eq. (4.2) at 100 Hz and10 kHz.

We attribute the high ε_r-values at low frequencies to an artefact that can often been noticed in the literature: the formula used for the evaluation assumes a capacitor thickness equal to the thickness of the dielectric film. If, however, the capacitance is due to grain boundaries (or

electrode spaces) the effective thickness is much smaller and the dielectric constant is overestimated. It is seen in Table 4.1, ε_r at 100 Hz, that this effect is strong in the samples prepared with much oxygen or at low temperature. Therefore, we suppose that these conditions favour the formation of grain boundaries with larger resistance.

Of the samples prepared at 700°C, CS-12 exhibits the largest ε_r. This sample showed minimum lattice distortion related to the (200) reflex. We conclude that this sample exhibits a more perfect crystalline structure than the other samples.

In the literature, similar phenomena have been observed for $(Ba,Sr)TiO_3$ films. Shen et al. [62] observed a low frequency dielectric relaxation when they annealed their films in oxygen atmosphere at 350°C. They attribute this effect to the large amount of negatively charged oxygen ions. Pontes et al. [63] also observed a low-frequency relaxation for samples post-annealed in O_2 at 350°C and attribute it to space charge polarization or Maxwell-Wagner type interfacial polarization. They relate the space charge polarization to a non-uniform charge accumulation.

Sometimes, polycrystalline high-k thin films show a Curie-von Schweidler relaxation behaviour [1] where the grain boundary and bulk properties cannot be extracted. In our case, however, two semicircles can clearly be separated for all samples except for CS-4. We therefore assume that in our films a Maxwell-Wagner relaxation occurs which is often observed in heterogeneous systems in which the component dielectrics have different conductivities. Such behaviour has been reported for the high-k dielectrics $CaCu_3Ti_4O_{12}$ [64] and hexagonal $BaTiO_3$ [60].

Following the discussion above, only the values at 10 kHz are physically meaningful. They are attributed to the bulk grains. In this case, the assumed thickness of the dielectric layer and consequently the value of the empty capacitance (C_0 in Eq. (2)) is correct.

The sharp decrease at higher frequencies is due to the fact that we observe non-zero resistance when the frequency approaches the high-frequency limit; but the imaginary part vanishes. This leads to vanishing ε_r, according to Eq. (4.2).

From Fig. 4.7 and from Table 4.1 it can be observed that for the thickest film (CS-4) prepared at 700°C and 5% O_2, the dielectric permittivity at 10 kHz is larger than that of the thinner films. This may be due to a better crystallinity and microstructure of the thicker film. For thin films of In_2O_3:Sn prepared earlier in the same sputter machine, it was found that the defect density decreases with increasing film thickness [40]. This may also be true for our sample series.

The sample prepared at 700°C and at 20% O_2 exhibits a larger ε_r (10 kHz) ~ 350. Taylor et al. reported that a mixture of 50:50 Ar and O_2 produces films with higher dielectric constant (ε_r ~250 at 10 kHz) and nearly stoichiometric composition. This indicates that oxygen rich environments enhance stoichiometric film growth. Similar results are obtained by the laser ablation method [41]. However, we also observe a very large ε_r at 100 Hz (~11,000) indicating a strong grain boundary effect. This indicates that, with increasing the oxygen in the film, oxygen atoms accumulate at grain boundaries and ultimately increase the resistance of the grain boundaries leading to the artifact of a high ε_r in the low frequency range.

The film deposited at the lower temperature (500°C) also exhibits such a high value of ε_r at 100 Hz even for 10% O_2 admixture. This is explained with easier oxygen trapping in grain boundaries at lower temperatures.

It is often observed that the dielectric permittivity of $SrTiO_3$ in the cubic phase follows the Curie-Weiss law:

$$\varepsilon_r = \frac{C}{T - \Theta}, \qquad (4.3)$$

where C and Θ are the Curie-Weiss constant and the Curie-Weiss temperature, respectively. The Curie-Weiss temperature is in general smaller than the phase transition temperature T_c: $\Theta < T_c$.

In order to check this for our films, the inverse permittivity ($1/\varepsilon_r$) of the bulk grains, as obtained from the simulations (except for CS-4 sample which obtained from Eq. 4.2), is depicted in Fig. 4.8 versus temperature**.** Generally, it is observed that the permittivity decreases with

increasing temperature and approximately follows the Curie-Weiss law. Fitting the parameters of Eq. (4.3) to the experimental data yielded negative Θ values for CS-6, CS-8 and CS-4 and positive values for the remaining samples. For the films CS-11, 12 and 13 the values of Θ (10–50 K) are consistent with the literature values [16,42]. Negative values of Θ have also been reported in the literature [42]. Shifts of the Curie-Weiss temperatures in the films have been explained with a reduced polarizability because of Ti non-stoichiometry [5] and with biaxial mechanical stress [43,44].

Since large variations in material properties occur at the transition temperature, it is desirable to use a material whose transition temperature is beyond the operating temperature range of DRAMs. The material used should always be one phase in the ferroelectric or paraelectric phase, without substantial variations in key parameters over the operating temperature range [45]. As seen in Fig. 4.8, the ε_r of our samples does not exhibit any anomaly in the temperature range of 20°C to 200°C indicating the absence of a phase transition.

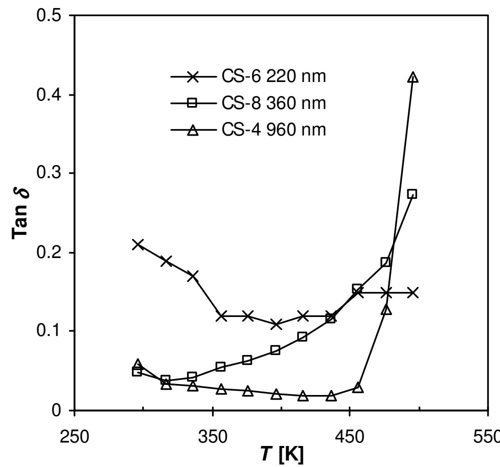

Fig. 4.9 Dielectric loss (tan δ) vs. temperature for the three samples prepared at 700°C, 5% O_2, with different thicknesses.

The dielectric loss (tan δ) at 10 kHz of the $SrTiO_3$ films prepared at 700°C and at 5% O_2 is shown in Fig. 4.9. The values we found are within the range reported in the literature for $SrTiO_3$: tan δ = 0.01 [48], 0.5 [35], 0.03 to 0.05 (at 100 kHz) [49]. The thickest film has the lowest dielectric loss, about 0.03 from room temperature up to 190°C. This means that the point

defect density decreases with increasing film thickness, and indicates again that the growth improves with increasing thickness.

Reference	Method	Capacitor stack	d [nm]	ε_r
Wang et al [32]	rf	$Si/SiO_2/Ti/Pt/STO/Pt$	450	~200 [1]
Taylor et al [44]	rf	$Al_2O_3/Pt/STO/Pt$	140	~250 [1]
Kimura et al [47]	MOCVD	$Si/SiO_2/Ta/Pt/STO/Au$	125	215 [2]
Ikuta et al [9]	ECR	InP/Pt/Ti/STO/Pt/Au	100	70 [3]
Radhakrishna et al [46]	rf	Pt/Si/STO/Pt	420	~147 [2]
Our samples	rf	$Si/SiO_2/RuO_2/STO/RuO_2$	~200-900	160-600 [1]

Table 4.2 Literature comparison of ε_r for $SrTiO_3$ films. (Thickness, d, rf magnetron sputtering, rf) Dielectric permittivity (ε_r) calculated, [1] at 10 kHz, [2] at 100 kHz, [3] at 0.1-1 GHz.

In Table 4.2 data for ε_r from the literature are summarized. Values up to 250 are reported. Our range is from 160 to 360 at 10 kHz are evaluated from Eq. (4.2). The values obtained for the bulk grains from the RC simulation are up to 600. That means that with RuO_2 electrodes at least the same dielectric permittivities as for Pt electrodes are obtained, with the potential to increase ε_r with further optimization of the deposition process.

4.4 Conclusions

Thin films capacitors with $SrTiO_3$ as a dielectric and RuO_2 as bottom and top electrodes have been fabricated by rf-magnetron sputtering. The bulk permittivity of the $SrTiO_3$ films is the same as or larger than that of films with Pt electrodes.

We have obtained best capacitors with the ε_r of bulk grains of about 300 (obtained from RC_p element simulations) for films deposited at 700°C and an oxygen content of 5% to 10% of the sputter atmosphere of about $3x10^{-2}$ mbar. With more oxygen it is possible to increase ε_r up to 600, but also isolating grain boundaries are obtained. This statement also holds for samples prepared at lower substrate temperature.

Thicker samples exhibit relatively larger ε_r (about 270) and lower dielectric loss as well as smaller lattice distortion with respect to the ideal perovskite lattice. This indicates that the growth of our films became more perfect with increasing thickness. Future investigations should therefore concentrate on improving the growth conditions for the initial stage of the deposition of the dielectric film in order to get good capacitors with thinner dielectric films.

The activation energies of the relaxation frequency or the conductivity are smaller than 100 meV indicating electron hopping between traps.

Acknowledgments

This work was supported by the Deutsche Forschungsgemeinschaft (DFG) in the framework of the Graduiertenkolleg 689 “Reactivity in the surface area”. We would like to thank Hans Werner Becker, University of Bochum, for performing RBS and Smail Boukercha, University of Duisburg-Essen, for taking the SEM cross sectional picture.

References

[1] M. Schumacher, G. W. Dietz and R. Waser *Integr. Ferroelec.* **10** 231 (1995)

[2] R. W. Babbit, T. E. Koscica and W. C. Drach *Microwave J.* 35 63 (1992)

[3] H.C. Li, W. Si, A. D. West and X. X. Xi *Appl. Phys. Lett.* **73** 464 (1998)

[4] X. X. Xi, H.C. Li, W. Si, A. A. Sirenko, I. A. Akimov, J. R. Fox, A. M. Clark and J. Hao *J. Electroceram.* **4** 393 (2000)

[5] S. K. Streiffer, C. Basceri, C. B. Parker, S. E. Lash and A. I. Kingon *J. Appl. Phys.* **86** (1999) 4565

[6] R. D. Vispute, J. Narayan, K. Dovidenko, K. Jagannadham, N Parikh, A. Suvkhanov and J. D. Budai *J. Appl. Phys.* **80** 6720 (1996)

[7] S. Nagata, T. Ueda, A. Noma, H. Koizumi, K. Kanazawa, H. Ishida and C. P. D. Araujo, IEEE Int. Solid-State Circuits Conf., San Francisco TP 11.3 172 (1993)

[8] N. K. Kim, S. G. Soon, W. J. Lee and H. G. Kim *J. Mater. Res.* **12** 1160 (1997)

[9] K. Ikuta, M. Tsukada and H. Nishimura *Jpn. J. Appl. Phys.* **37** 1960 (1998)

[10] T. B. Nishimura, N. Iwata, K. Takemura, M. Kuzuhara and Y. Miyasaka *Jpn. J. Appl. Phys*. **35** L1683 (1996)

[11] J. R. Belsick and S. B. Krupanidhi *J. Appl. Phys.* **74** 6851 (1993)

[12] X. Wang, U. Helmersson, L. D. Madsen, I. P. Ivanov, P. Münger, S. Rudner, B. Hjörvarsson and J. –E. Sundgren *J. Vac. Sci. Technol. A* **17** 564 (1999)

[13] G. Shirane and Y. Yamada *Phys. Rev.* **177** 858 (1969)

[14] M. A. Saifi and L. E. Cross *Phys. Rev. B* **2** 677 (1970)

[15] K. A. Müller and H. Burkard *Phys. Rev. B* **19** (1979) 3593

[16] T. Sakudo and H. Unoki *Phys. Rev. Lett.* **26** 851 (1971)

[17] A. Linz Jr. *Phys. Rev.* **91** 753 (1953)

[18] J. M. Herbert, Ceramic Dielectrics and Capacitors, Gordon and Breach, P.226 (1985)

[19] S. K. Streiffer, C. Basceri, C. B. Parker, S. E. Lash and A. I. Kingon *J. Appl. Phys*. **86** 4565 (1999)

[20] T. R. Taylor, P. J. Hansen, N. Pervez, B. Acikel, R. A. York and J. S. Speck *J. Appl. Phys.* **94** 3390 (2003)

[21] C. Zhou and D. M. Newns *J. Appl. Phys.* **82** 3081 (1997)

[22] C. Basceri, S. K. Streiffer, A. I. Kingon and R. Waser *J. Appl. Phys.* **82** 2497 (1997)

[23] C. S. Hwang *J. Appl. Phys.* **92** 432 (2002)

[24] C. A. -P de Araujo, J. D. Cuchiaro, L. D. McMillan, M. C. Scott and J. F. Scott *Nature* 374 627 (1995)

[25] D. P. Vijay and S. B. Desu *J. Electrochem. Soc.* **140** 2640 (1993)

[26] H. N. Al-Shareef, K. R. Bellur, O. Auciello and A. I. Kingon *Integr. Ferroelectr.* 2 185 (1994)

[27] L. Krusin-Elbaum and M. Wittmer *J. Electrochem. Soc.* **135** 2610 (1998)

[28] C. N. Rao and G. V. Subba Rao, National Bureau of Standards Report No. NSRDS-NBS49, 1974

[29] S. Komatsu, K. Abe and N. Fukushima *Jpn. J. Appl. Phys.* **37** 5651 (1998)

[30] H. Yamaguchi, S. Matsubara and Y. Miyasaka *Jpn. J. Appl. Phys.* **30** 2197 (1991)

[31] H. Yamaguchi, P. Y. Lesaicherre, T. Sakuma, Y. Miyasaka, A. Ishitani and M. Yoshida *Jpn. J. Appl. Phys.* **32** 4069 (1993)

[32] M. –C. Wang, F. –Y. Hsiao, H. –H. Huang and N. –C. Wu *Jpn. J. Appl. Phys.* **43** 6323 (2004)

[33] J. E. Bauerle *J. Phys. Chem. Solids* **30** 2657 (1969)

[34] J. R. Macdonald, Impedance Spectroscopy, Willey, New York (1987)

[35] B. Prijamboedi, H. Takashima, R. Wang, A. Shoji and M. Itoh *Phys. Stat. Sol. (a)* **202** R152 (2005)

[36] C. Ang and Z. Yu *Phys. Rev. B* **61** 11363 (2000)

[37] W. Kleemann and H. Schremmer *Phys. Rev. B* **40** 7428 (1989)

[38] B. Karunagaran, S. J. Chung, E. –K. Suh and D. Mangalaraj *Physica B* 369129 (2005)

[39] P. C. Joshi and S. B. Krupanidhi *J. Appl. Phys.* **73** 7627 (1993)

[40] Z. Qiao, R. Latz and D. Mergel *Thin Solid Films* **466** 250 (2004)

[41] E. J. Tarsa, E. A. Hachfeld, F. T. Quilan, J. S. Speck and M. Eddy *Appl. Phys. Lett.* **68** 490 (1996)

[42] S. Schmidt, J. Liu, S. P. Keane, L. D. Bregante, D. O. Klenov and S. Stemmer *J. Am. Ceram. Soc.* **88** 789 (2005)

[43] T. M. Shaw, Z. Suo, M. Huang, E. Liniger, R. B. Laibowitz and J. D. Baniecki *Appl. Phys. Lett.* **75** 2129 (1999)

[44] T. R. Taylor, P. J. Hansen, B. Acikel, N. Pervez, R. A. York and S. K. Streiffer, J. S. Speck *Appl. Phys.Lett.* **80** 1978 (2002)

[45] L. H. Parker and A. F. Trsch *IEEE Circuits Device Mag.* **6** 17 (1990)

[46] K. Radhakrishnan, C. L. Tan, H. Q. Zheng and G. I. Ng *J. Vac. Sci. Technol. A* **18** 1638 (2000)

[47] T. Kimura, H. Yamauchi, H. Machida, H. Kokubun and M. Yamada *Jpn. J. Appl. Phys.* **33** 5119 (1994)

[48] C. Ang, Z. Yu, L. E. Cross, R. Guo and A. S. Bhalla *Appl. Phys. Lett.* **79** 818 (2001)

[49] Z. Wang, V. Kugler, U. Helmersson, E. K. Evangelou, N. Konofaos, S. Nakao and P. Jin *Phil. Mag. B* **82** 891 (2002)

[50] D. Mergel, K. Thiele and Z. Qiao *J. Mater. Res.* **20** 2503 (2005)

[51] D. Mergel and Z. Qiao *J. Appl. Phys.* **95** 5608 (2004)

[52] M. Mahesh Kumar and M. L. Post *J. Appl. Phys.* **97** 114916 (2005)

[53] M. Li, A. Fereira and D. C. Sinclair *J. Appl. Phys.* **98** 084101 (2005)

[54] C. K. Suman, K. Prasad and R. N. Choudary *J. Mater. Sci.* **41** 369 (2006)

[55] Y. J. Li, X. M. Chen, R. Z. Hou and Y. H. Tang *Solid State Commun.* **137** 120 (2006)

[56] S. Sen, P. Pramanik and R. N. P. Choudhary *Appl. Phys. A* **82** 549 (2006)

[57] S. Saha and T. P. Sinha *J. Appl. Phys.* **99** 014109 (2006)

[58] H. Beltràn, E. Cordoncillo, P. Escribano, D. C. Sinclair and A. R. West *J. Appl. Phys.* **98** 094102 (2005)

[59] S. Jayanthi and T. R. N. Kutty *J. Mater. Sci.* **16** 269 (2005)

[60] J. Yu, T. Ishikawa, Y. Arai, S. Yoda, M. Itoh and Y. Saita *Appl. Phys. Lett.* **87** 252904 (2005)

[61] J. E. Diosa, R. A. Vargas, I. Albinsson and B. –E. Mellander *Solid State Commun.* **136** 601 (2005)

[62] M. Shen, Z. Dong, Z. Gan, S. Ge and W. Cao *Appl. Phys. Lett.* **80** 2538 (2002)

[63] F. M. Pontes, E. R. Leite, E. Longo, J. A. Varela, E. B. Araujo and J. A. Eiras *Appl. Phys. Lett.* **76** 2433 (2000)

[64] J. Liu, C-G. Duan, W. N. Mei, R. W. Smith and J. R. Hardy *J. Appl. Phys.* **98** 093703 (2005)

5. Frequency and temperature dependent electrical properties of $BaTiO_3$ thin film capacitors studied by complex impedance spectroscopy

Abstract

Thin film capacitors with $BaTiO_3$ as dielectric and RuO_2 as electrode material have been prepared by rf-magnetron sputtering at temperatures up to 750°C and under various oxygen partial pressures. They have been analyzed by complex impedance spectroscopy in the temperature range 20 to 200°C. At about 10 kHz, the grain effect is dominant and the electrical and dielectric properties of the bulk grains can be extracted. The activation energies of the conductivity are in the range 30 to 100 meV, characteristic for hopping of electrons. The dielectric constant at room temperature ranges from 120 to 1500, depending on the preparation conditions. There is a maximum in the temperature dependence of ε_r that shifts to lower temperatures when the capacitors have been prepared with more oxygen. Above that temperature, Curie-Weiss behaviour is observed with characteristic temperatures in the range 250 to 400 K. Biggest dielectric permittivity and lowest dielectric loss are obtained for films prepared at 750°C at medium oxygen partial pressures. With increasing oxygen content the grain boundary effect becomes stronger for the films prepared at all deposition temperatures. The films prepared with high oxygen partial pressure show increased crystallinity and dense columnar structure.

5.1 Introduction

Perovskite type high permittivity thin film materials have been receiving great interest as new dielectric materials replacing SiO_2 and/or Si_3N_4 dielectrics [1] by classical perovskite materials $SrTiO_3$, $BaTiO_3$, and $(Ba_xSr_{1-x})TiO_3$ in future ultra-large scale integrated electronic circuits, e.g., dynamic random access memories (DRAM) [2] and tunable microwave device applications [3], because these materials shows high insulating properties with large values of relative permittivity and low dielectric loss, and large change in dielectric constant with an applied dc electric field [4]. $BaTiO_3$ thin films have been widely studied because of its high dielectric constant in thin film hybrid and integrated circuits [5] for above mentioned applications.

To obtain the thin film of perovskite materials, various deposition techniques have been employed, including excimer laser ablation [6], flash evaporation [7], chemical vapor deposition (CVD) [8], sol-gel process [9], metal-organic chemical vapor deposition (MOCVD) [10] and rf magnetron sputtering [11]. The rf magnetron sputtering has been demonstrated to be the most promising method, because it offers good reproducibility, uniformity and simplicity [12].

Until recent days Pt has been the most commonly used electrode for ferroelectric thin film capacitors due to the low resistivity and chemical stability [13], during the annealing in the oxygen ambient above 500°C, however, the degree of oxidation and interdiffusion remarkably increased, resulting in the degradation of the electrical properties of ferroelectric materials [14]. Also the sputtered Pt electrode is known to have the disadvantage of hillock formation, which can electrically short-circuit the capacitor. To overcome these problems, RuO_2 is a promising conductive metallic oxide, due to its low resistivity (~ 40 μΩcm), excellent diffusion barrier properties, good thermal stability and high corrosion resistance [15,16].

Impedance spectroscopy has been used for probing the relaxation processes during the charge transport within the electronic ceramics [17]. The equivalent circuit can be envisaged as a series of lumped elements, i.e. several resistance and capacitance elements in parallel, each corresponding to a different process occurring at the electrode interface, at the grain boundaries

or within the grains themselves. In most types of the electronic ceramics, the relaxations are non-uniform so that a Cole-Cole type distribution prevails. The complex impedance spectra of polycrystalline ceramics are modified by the defect distribution, including impurities [18] in the grains and the contribution from the grain boundaries [19] caused by segregation of impurities and native defects.

There have been several reports on frequency and temperature dependent [20-23] dielectric properties of $BaTiO_3$ materials. But, there are very few reports on the study of the RuO_2 electrode based perovskite [24,25] thin film capacitors with emphasis of frequency and temperature dependent.

In this work, we study the effect of oxygen flux during the deposition and substrate temperature on the properties of $BaTiO_3$ thin film capacitors with RuO_2 as a top and bottom electrodes by means of impedance spectroscopy.

5.2 Experimental

$BaTiO_3$ thin films were deposited by rf magnetron sputtering (Von Ardenne LS 500 S). A sintered and stoichiometric $BaTiO_3$ target (purity 99.99% and rf power 300 W) was sputtered in an Ar/O_2 plasma to deposit $BaTiO_3$ thin films at substrate temperatures from 450 to 750°C. The high purity (5N) Ar (50 sccm) and O_2 (0 to 15 sccm) gas mixtures were used. Circular p-type Si(100) wafer substrates of 25 mm diam. and about 0.5 mm thickness were cleaned in an ultrasonic bath. A SiO_2 layer was grown by thermal oxidation.

The capacitor structure comprised RuO_2 layers as bottom (50 nm) and top (30 nm) electrodes. They are deposited by rf magnetron sputtering of a RuO_2 target (purity 99.99%, Ar 50 sccm, rf power 75 W) at 540°C and room temperature, respectively. The area of the top electrode is 7 mm^2. The sputter chamber was pumped down to $3.5x10^{-6}$ mbar, and the $Ar+O_2$ pressure during deposition was $1.2x10^{-2}$ mbar. The thickness of the films ranges from around 350 to 750 nm.

The thickness of the $BaTiO_3$ thin films was determined with a profilometer (Dektak 6M Stylus). Structure determination was carried out by x-ray diffraction (Philips 1710 x-ray diffractometer) with Co $L\alpha$ (1.7902 Å) radiation. The complex impedance was measured using a Solartron Schlumberger SI 1260 impedance/gain-phase analyzer. The temperature and frequency dependent dielectric properties were measured from 20 to 200°C and 10 Hz to 10 MHz, respectively. Cross sections of the films have been obtained by scanning electron microscopy with a FEI Quanta 400 FEG on the edges of broken Si substrates.

Sample	P [x10^{-2} mbar]	T_{sub}	O_2 %	d [nm]	ε_r			E_σ [meV]
					at 100 Hz	10 KHz	$^*RC_p$	
CB-4	3.0	600°C	30	625	5553	702	1468	25
CB-5	2.4	600°C	20	635	4061	791	1268	94
CB-6	2.4	600°C	10	610	141	64	179	26
CB-7	2.0	600°C	0	490	70	70	-	-
CB-8	1.9	450°C	0	480	4157	464	58	-
CB-9	2.2	750°C	0	370	497	329	366	-
CB-13	4.1	750°C	10	750	247	203	767	-
CB-14	4.8	750°C	20	775	759	184	1486	-

Table 5.1 The deposition parameters, dielectric permittivity (ε_r) and activation energies for investigated capacitors (Thickness, d, conductivity activation energy, E_σ, *at room temperature)

5.3 Results and discussion

5.3.1 *Structural properties*

X-ray diffractograms have been taken for all samples. Most peaks can be explained with the perovskite structure. We have selected two angular regions that show clear differences between the samples. The diffractograms have been treated in the way described by Mergel et al. [26]: the background is subtracted and the intensity is corrected with respect to thickness.

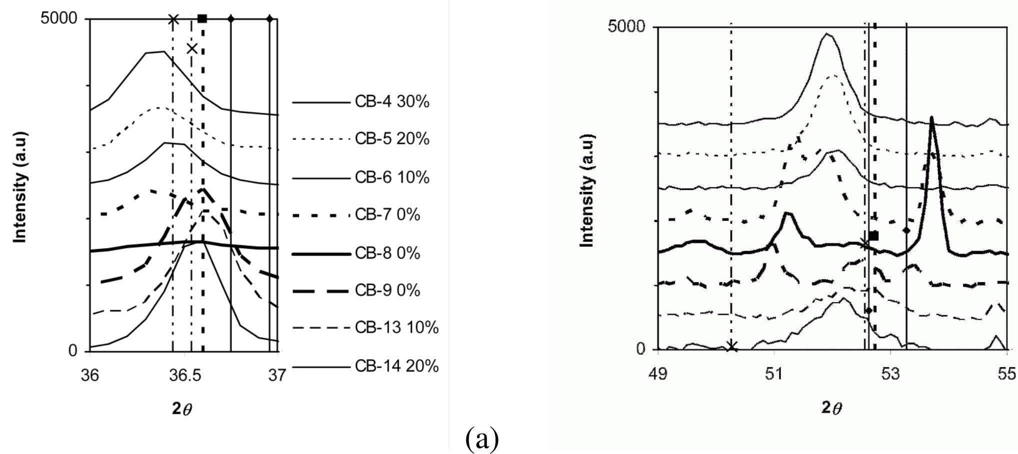

Fig. 5.1a to **b** (a) X-ray diffractograms of all samples in the angular region of the (110) reflex of the perovskite structure, with the lines of the cubic (---), tetragonal (––) and hexagonal (– · – ·) single crystalline phases. CB-4 to CB-7: prepared at 600°C, CB-8: prepared at 450°C, CB-9 to CB-14: prepared at 750°C. The baseline of the various diffractograms has been shifted by an intensity of 500 with respect to the lower curve. (b) As Fig. 1a, for the (200) reflex.

Fig. 5.1a (2θ = 36° to 37°) shows the region around the (110) reflex of the cubic structure, the strongest of the PDF measurement. We see that the samples prepared at 750°C show peaks at the exact crystalline position. The sample prepared at 450°C does not exhibit any intensity peak in this region. The peaks of the samples prepared at 600°C are shifted to smaller 2θ values indicating bigger lattice constants with increasing oxygen partial pressure.

Fig. 5.1b (2θ = 49° to 55°) shows the region around the cubic and tetragonal (200) reflexes and the hexagonal (106) and (204) reflexes. The samples prepared at 600°C show the same shift as for the (110) reflex. The peaks close to cubic (200) of the samples prepared at 750°C are weaker but seem to show also the trend to be shifted towards smaller 2θ values (bigger lattice constants) with increasing oxygen partial pressure. The samples prepared with 0% oxygen show additional peaks around 51° and 54°. They cannot be clearly identified but it should be noticed that their distance corresponds to the distance of the two hexagonal peaks in this region. Therefore, it is possible that they belong to a hexagonal structure with smaller lattice constant (larger 2θ values) than the ideal crystalline one.

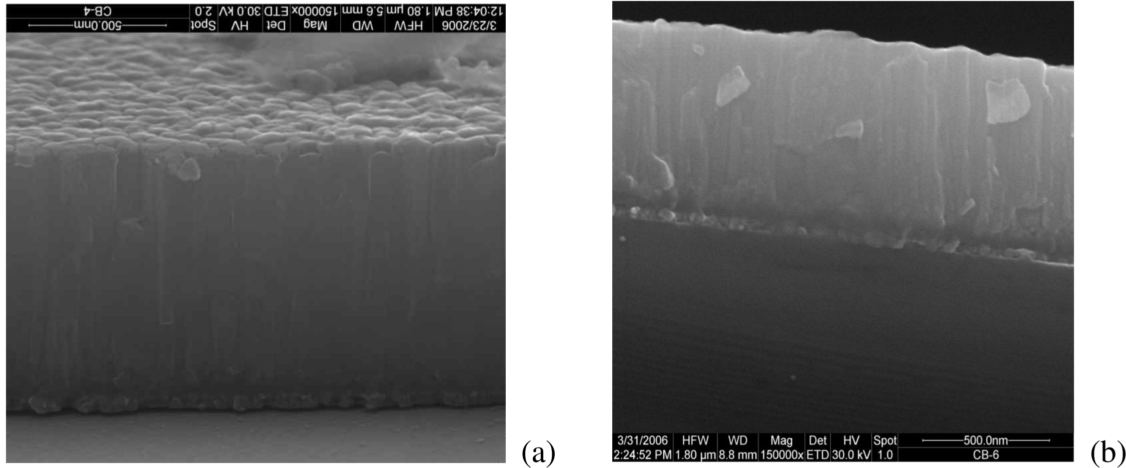

Fig. 5.2 a and **b** Cross-sectional SEM of $BaTiO_3$ capacitors deposited at 600°C substrate temperature. (a) CB-4 (30% O_2) and (b) CB-6 (10% O_2).

Figs. 5.2 (a) and (b) show cross sections of CB-4 (30% O_2) and CB-6 (10% O_2), respectively. Close to the substrate, the about 50 nm thick RuO_2 film is to be seen. It exhibits a relatively grainy structure. The $BaTiO_3$ thin films on top of it exhibit a columnar structure. In CB-4, the columns are more regular with an average diameter of 50 to 80 nm. In CB-6, the diameter ranges between 50 and 150 nm and some large grains are to be seen.

5.3.2 Complex impedance study

Complex impedance spectroscopy (IS) gives a possibility to distinguish between different effects during the metal-insulator-metal capacitor test. The experimental data are analyzed in terms of the complex formula for the impedance, $Z^*=Z'+jZ''$. The complex impedance was measured by a Solartron Schlumberger SI 1260 impedance/gain analyzer. The temperature and frequency dependent properties of Z^* were measured from 20 to 200°C and 10 Hz to 10 MHz, respectively.

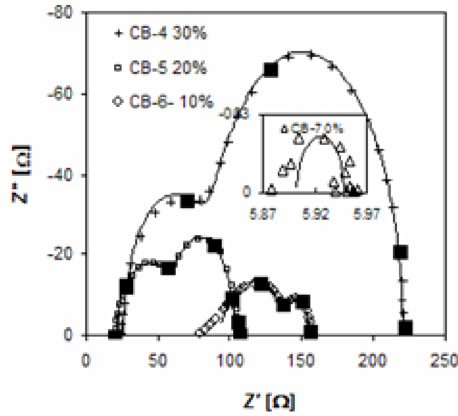

(a)

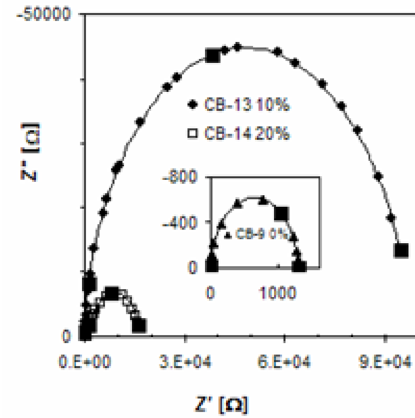

(b)

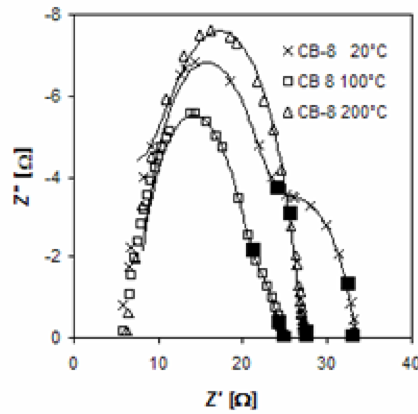

(c)

Fig. 5.3 Some *Z′-Z″* plots of capacitors prepared at 600°C (a) 750°C (b) and 450°C (c). Experimental data points together with the curves obtained from the RC simulations. The frequency decades are marked with large filled squares.

Figs. 5.3 (a) and (b) show the IS plots of $BaTiO_3$ thin films deposited in various oxygen partial pressures at 600°C and 750°C substrate temperature, respectively. Fig. 5.3 (c) shows the film deposited at 450°C without oxygen for different measuring temperatures. All spectra are shown with the simulated curves along with frequency decades. It is evident that the spectra consist of a superposition of semicircles. They could indeed be modeled as a series of two to three RC_p elements, sometimes with a resistor in series. RC_p means a parallel circuit of a resistance R and a capacitor C. For the samples CB-6 and CB-8 one R and two RQ_p had to be taken to get a good simulation of the measured curve. RQ_p means a parallel circuit of a resistance, R and a constant phase element (CPE), Q. The impedance of a Q-element is given by $Z = A{\cdot}(\mathrm{i}\omega)^{-1}$.

Usually in the literature, the semicircle dominant at the lowest frequency is attributed to the electrode, that at the highest frequency to the bulk grain and that at middle frequencies to the grain boundaries.

When there is more than one semicircle, we have to decide which one is related to the grain boundary and which to the bulk grain. From the literature it is known that the resistance and the capacitance of the grain boundaries are always larger than those of the bulk grains. We conclude that the relaxation time $\tau = RC = \rho\varepsilon_r\varepsilon_0$ is larger for the grain boundaries. Consequently, the characteristic frequency $f_g = (2\pi\tau)^{-1}$ is relatively smaller and the semicircle of the grain boundaries occurs at lower frequencies. The bulk grain resistance is determined from the high-frequency semicircle of the RC_p or RQ_p equivalent circuit. This procedure is well established in the literature. It has been applied in the case of many dielectric and ferroelectric materials [62,63,64,65].

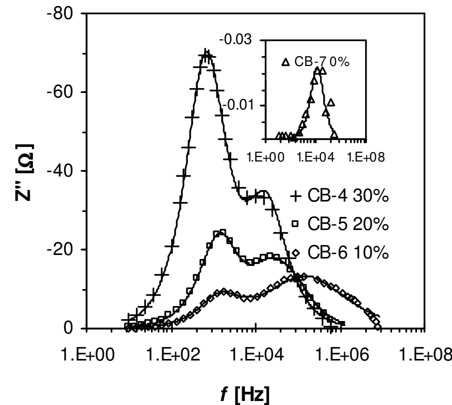

Fig. 5.4 Imaginary part of the impedance vs. frequency of samples prepared at 600°C under various oxygen partial pressures.

Fig. 5.4 shows the imaginary impedance (Z'') vs. frequency (f) of CB-4, 5, 6, and 7 deposited at 600°C in 20, 10, 5, and 0 sccm oxygen flux, respectively, together with the simulated curves. It clearly shows that with increasing oxygen partial pressure, the low-frequency peak attributed to the grain boundary effect increases dramatically.

5.3.2.1 Bulk conductivity and relaxation time

The conductivity of the material has been evaluated as a function of 1000/*T* (not shown here). We try to explain it by a thermally activated transport of Arrhenius type governed by the relation:

$$\sigma = \sigma_0 \exp\left(-\frac{E_\sigma}{kT}\right) \tag{5.1}$$

where σ, E_σ, and *k* represent the pre-exponential factor, the activation energy of the mobile charge carriers and the Boltzmann constant, respectively. The activation energies have been estimated and are shown in Table 5.1. They are comparable to those reported in the literature for various materials: 4 to 11 meV for $SrTiO_3$ [28], 33 to 62 meV for $(Sr,Bi)TiO_3$ [29], 12 meV for $(Sr,Ca)TiO_3$ [30], and 100 meV for TiO_2 [31]. Such small activation energies have been attributed to hopping of electrons between traps generated e.g. by off-centre defects.

Similar activation energies are observed for the relaxation time, $\tau = RC$ (not shown here). The activation energies (E_τ) obtained from this Arrhenius plot is 0.08, 0.15 and 0.61 eV for CB-4, 5 and 6, respectively. The activation energy of CB-6, prepared at 10% oxygen is 0.61, a value similar to that reported by Kang et al. 2003.

In perovskite oxides or in many other ionic solid materials, the major mode of charge transport is a multiple hopping process [32]. The hopping process normally takes place across the potential barriers set up by the lattice structure and the local environment of other atoms/ions. However, due to irregularities in the lattice structure as e.g. near defect sites, the potential barriers will have different magnitudes, as well as varied widths [33,34].

5.3.2.2 Dielectric properties

The dielectric permittivity of $BaTiO_3$ films was calculated from Eq. (5.2):

$$\varepsilon_r = \frac{-Z''}{(2\pi f C_0)(Z'^2 + Z''^2)} = \frac{-Z''}{(2\pi f \varepsilon_0)(Z'^2 + Z''^2)} \cdot \frac{d}{A} \quad (5.2)$$

where d, A, C_0 and ε_0 are thickness of the dielectric film, area of the electrode, capacitance of the empty capacitor, and permittivity of free space (8.854x10^{-12} F/m), respectively. It is depicted in Figs. 5.5 and 5.6 as a function of frequency for samples prepared at 600°C and 750°C, respectively. It clearly shows that at lower frequencies (up to 1 kHz) ε_r values are higher (~5000), and then drop abruptly to lower values. It is considered that on the low-frequency part of the step, electrode and grain boundary effects dominate and at higher frequencies, the properties are determined by the bulk grains.

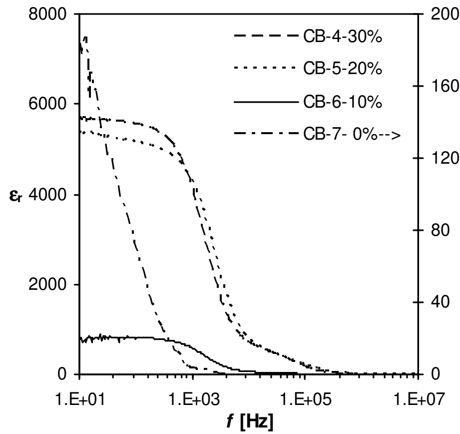

Fig. 5.5 Dielectric permittivity as obtained from Eq. (2) vs. frequency for samples prepared at 600°C under various oxygen partial pressures.

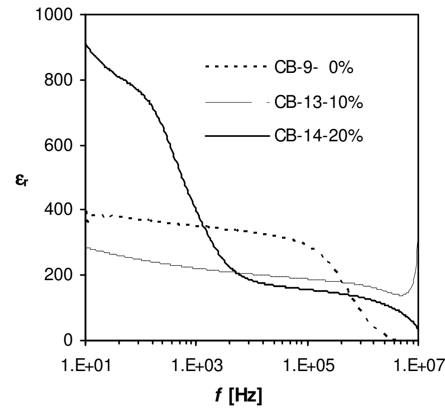

Fig. 5.6 Dielectric permittivity as obtained from Eq. (2) vs. frequency for samples prepared at 750°C under various oxygen partial pressures.

In the literature, similar phenomena have been observed for $(Ba,Sr)TiO_3$ films. Shen et al. [66] observed a low frequency dielectric relaxation when they annealed their films in oxygen atmosphere at 350°C. They attribute this effect to the large amount of negatively charged oxygen ions. Pontes et al. [67] also observed a low-frequency relaxation for samples post-annealed in O_2 at 350°C and attribute it to space charge polarization or Maxwell-Wagner type interfacial polarization. They relate the space charge polarization to a non-uniform charge accumulation.

The ε_r values at 100 Hz and 10 kHz are tabulated in Table 5.1 for all samples. In this table we also report the ε_r values obtained from the equivalent circuit with the highest frequency attributed to the bulk of the grains. It is evident that with increasing oxygen partial pressure ε_r values are higher. In the literature, small ε_r values are attributed to a large concentration of oxygen vacancy defects [35]. This explanation applies also to our results since with more oxygen during deposition less oxygen vacancies are expected.

As a typical behavior, the dielectric constant is higher at lower frequencies and decreases with increasing frequency. Such behavior has been observed in many MIS (metal-insulator-semiconductor) systems [36] and various models have been proposed in terms of the frequency dispersion of the permittivity of the insulator film, the presence of a highly resistive interfacial layer or a high density distribution of interface states. A simple way to account for the increase in permittivity with decreasing frequency is to assume the presence of some interface traps which were induced by stress. These interface traps respond to all frequencies and the permittivity induced by the interface state is changing with the frequency. The lower the frequency, the more the interface states charges can follow the alternative current variation and thus the larger the interface states capacitance which leads to the anomalous frequency dispersion, contributing to the total capacitance. Similar results were reported by Sawada et al [37]. Such interface effects may be the reason for the increase of ε_r of CB-14 below 100 Hz.

The semicircle attributed to the grain boundaries is centred at about 1 kHz. When the impedance of the grain boundaries is much larger than that of the grains then the ε_r calculated from Eq. (5.2) is too large by a factor corresponding to the ratio of the thickness of the grains to that of the grain boundaries.

Around 10 kHz, all spectra exhibit a plateau. According to our model, the RC_p or RQ_p-element of the grains dominates the spectra. In this case, the assumed thickness of the dielectric layer and consequently the value of the empty capacitance (C_0 in Eq. (5.2)) is correct. Therefore, only the ε_r values at 10 kHz in Table 1 are physically meaningful.

The sharp decrease at higher frequencies for CB-9 and CB-14 is due to the fact that we observe non-zero resistance when the frequency approaches the high-frequency limit; but the imaginary part vanishes. This leads to vanishing ε_r, according to Eq. (5.2).

We now discuss the possible effect of the oxygen partial pressure during deposition on the dielectric properties of the capacitors. It may be a combined effect of the oxygen content and the crystalline structure. The dielectric constant of the $BaTiO_3$ thin film increases due to the improved crystallinity of the $BaTiO_3$ film. There are indications for increasing crystallinity with increasing oxygen content in Figs. 5.1a and b. The peak intensity at around 36.3° in Fig. 5.1a and that around 52° in Fig. 5.1b is biggest for CB-4, the film prepared with 30% oxygen. It is considered that the oxygen-rich atmosphere during the deposition of $BaTiO_3$ thin films promoted the formation of denser and more stable $BaTiO_3$ films, since perovskite ($BaTiO_3$) films need more oxygen to recover the oxygen vacancies during the nucleation and growth stage [38].

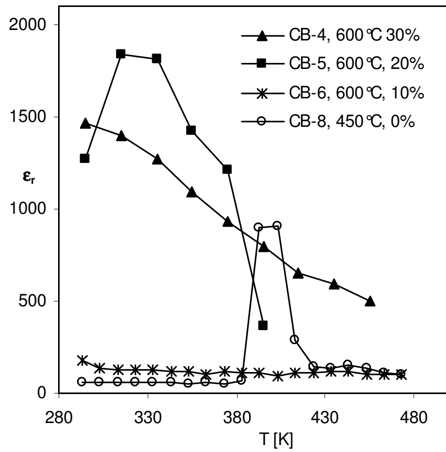

Fig. 5.7 Dielectric permittivity obtained from the RC-simulations vs. temperature for the samples prepared at 600°C and 450°C.

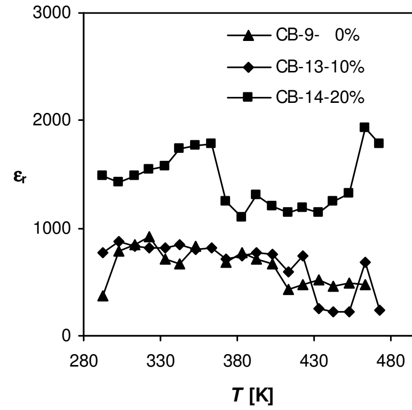

Fig. 5.8 Dielectric permittivity obtained from the RC-simulations vs. temperature for the samples prepared at 750°C.

From Figs. 5.7 and 5.8 (ε_r as a function of temperature) it can be observed that the dielectric permittivity of some samples is temperature dependent, with a maximum at medium temperatures. Films deposited at higher oxygen pressures (CB-4, 30% and CB-5, 20%) show higher ε_r than CB-6 (10%). The dielectric permittivity of CB-6 is temperature independent in the

measured range. We assume that the maximum is related to a cubic to tetragonal phase transition that has already been discussed in the literature [39]. The characteristic temperatures are in the range 293 to 493 K. For CB-4 it is 280 K or below. The lower values of T_c are observed for higher oxygen partial pressures during deposition. This may be explained with a stress effect as is discussed below.

At lower oxygen pressures, a higher concentration of oxygen vacancies is expected [35] with a reduction in the dielectric properties. At higher oxygen pressure more stress is induced in the film [40]. It has been shown that films in tensile stress show higher ε_r values than those in compressive stress [41,42]. With high stress in the film the ferroelectric phase transition temperature will move to lower values and the transition is broadened [43]. Buessem et al. [44] argued that the stress system would consist of a combination of uniform mechanical compression along the *c* axis and tensions along both *a* axes and that such a stress system would lead to a decrease in T_c. Shifts in the phase transformation temperature are expected from a thermodynamic theory developed to explain the properties of epitaxial perovskite films under biaxial stress [45,46].

The film deposited at the lowest substrate temperature (450°C) without additional oxygen shows the sharpest phase transition with T_c about 400K, which is well consistent with literature values for single crystals [47,48]. We suppose that under these preparation conditions there will be negligible stress in the films.

Fig. 5.8 shows the dielectric constant of films deposited at 750°C in various oxygen partial pressures as a function of temperature. The ε_r values are relatively large and do not vary much in the measuring temperature range (293-473 K). A similar trend was observed for multilayer ceramic capacitors (MLCC) by Feng et al [49]. Our ε_r values are well consistent with their results.

It is often observed that the dielectric permittivity of $BaTiO_3$ in the cubic phase follows the Curie-Weiss law:

$$\varepsilon_r = \frac{C}{T - \Theta} \qquad (5.3)$$

where C and Θ are the Curie-Weiss constant and Curie-Weiss temperature, respectively. The Curie-Weiss temperature is in general smaller than the temperature T_c of the cubic-tetragonal phase transition: $\Theta < T_c$. In Fig. 5.9 the inverse dielectric permittivity ($1/\varepsilon_r$) is depicted vs. T. The data follow roughly a linear relationship and Θ can be extracted. Our Curie-Weiss temperature values are well consistent with the values of Takeuchi et al. [50] who observed values of 400 to 470 K. Saad et al. [51] and Johnson [52] also obtained Θ–values very close to 400 K.

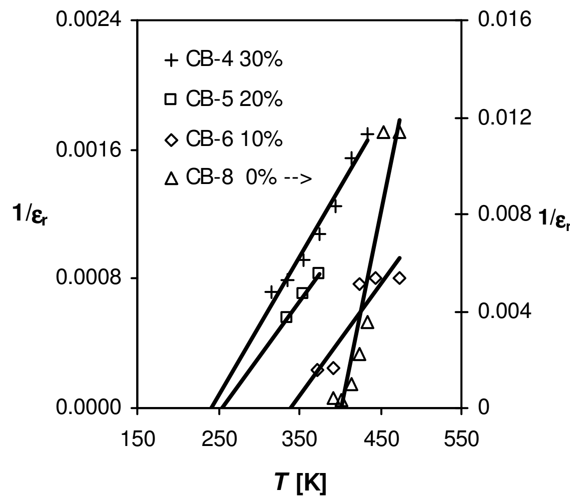

Fig. 5.9 Curie-Weiss plot of the dielectric permittivity for temperatures above the temperature of the maximum in Figs. 5.7 and 5.8.

In our films, the Curie-Weiss temperature shifts to lower values for samples prepared at higher oxygen partial pressures. Shifts of the Curie-Weiss temperatures in thin films have been explained with a reduced polarizability because of Ti non-stoichiometry by Steiffer et al. and with biaxial mechanical stress [53,54].

Since large variations in material properties occur at the transition temperature, it is desirable to use in many applications, e.g. in DRAMs, a material whose transition temperature is

beyond the operating temperature range [55]. This condition is for our preparation method best fulfilled for films prepared at 750°C.

5.3.2.3 *Dielectric loss* (tan δ)

The dielectric loss (tan δ) of $BaTiO_3$ thin films was calculated from:

$$\tan\delta = -\frac{Z'}{Z''} \qquad (5.4)$$

where, Z' and Z'' are real and imaginary parts of the complex impedance, respectively. Our results are shown in Figs. 5.10 (films prepared at 750°C) and 5.11 (films prepared at 600°C).

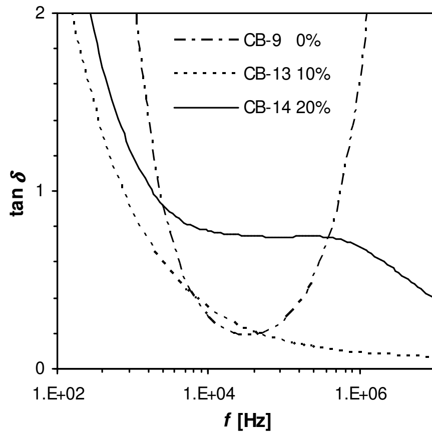

Fig. 5.10 Dielectric loss tangent of the samples prepared at 750°C.

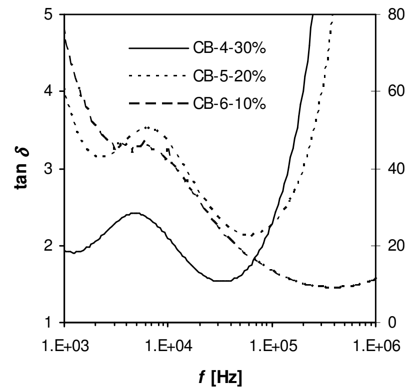

Fig. 5.11 Dielectric loss tangent of the samples prepared at 600°C.

Films deposited at higher oxygen pressures show lower dielectric loss. The values of our films prepared at 750°C are comparable with those reported in the literature [56]. Those for films prepared at lower temperatures are much larger.

Reference	Method	Capacitor stack	*d* [nm]	ε_r
Zeng et al. [56]	MOCVD	Pt/Si/BTO/Pt	1000	~120 [a]
Ring et al. [57]	rf	Pt/barrier/BTO/Pt	700	~750 [c]
Lee et al. [58]	Poly.	$Si/SiO_2/Pt/BTO/Au$	560	700[b]
B. Lee et al. [59]	Sol-Gel	$Si/SiO_2/Ti/Pt/BTO/Au$	500	~320[b]
Jia et al. [60]	rf	Al/Si/BTO/Au	~200	~45 [d]
Our samples	rf	$Si/SiO_2/RuO_2/BTO/RuO_2$	~350-750	~130-1500

Table 5.2 Literature values of ε_r for $BaTiO_3$ films. (Thickness, *d*, rf magnetron sputtering, rf, poly= Polymeric precursor method) Dielectric permittivity (ε_r) calculated, [a] 1 kHz, [b] 10 kHz, [c] 100 kHz, [d] 1 MHz.

5.4 Conclusions

The films prepared with high oxygen partial pressure show increased crystallinity and a dense columnar structure.

The films prepared at the highest temperature (750°C) exhibit the best dielectric properties with respect to applications: the dielectric permittivity is high and relatively temperature independent in the temperature range 20°C to 200°C; and the dielectric loss is low. Best results are obtained for 10% oxygen admixture to the sputter gas. These results are comparable with those prepared with Pt electrodes.

Films prepared at lower temperatures show signs of a phase transition in the measuring temperature range, 20°C to 200°C. The characteristic temperature decreases with increasing oxygen partial pressure during deposition. This is tentatively explained with increased stress in the films. The activation energies of conductivity are below 100 meV. This is characteristic for hopping conduction between defects. Altogether, we conclude that RuO_2 electrodes are well suited for thin film capacitors with $BaTiO_3$ as dielectric material.

Acknowledgment

We thank Werner Osswald, Tamara Gurenko and Christian Pauly for having performed the impedance measurements.

Appendix: Resistance of $BaTiO_3$

The resistances of various $BaTiO_3$ samples obtained from impedance measurements reported in the literature are shown in the figure below. The bottom line at "Reference 0" represents our range. From the table and the figure it can be seen that our films cover the whole range reported in the literature.

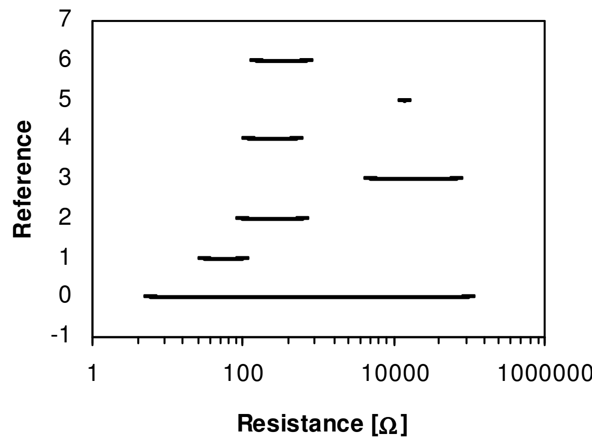

Reference	Prep. method	Simulation	*d* [nm]	Resistance [Ω]
Yu et al. [1]	Single crystal	3 *RC*		30-100 at R.T
Kim et al. 2005 [2]	Ceramic	-		100-600 at R.T
Yang et al. [3]	Ceramic	3 *RC*		$0.5\text{-}7\times10^4$
Hari et al. [4]	Ceramic	2 *RC*		120-500
Victor et al. [5]	PLD	-	500-800	1.4×10^4
Kim et al. 2004 [6]	Ceramic	-		150-700
Our samples	rf mag. sputtering	2 *RC* and *RQ*	~500-800	6×10^0 to 1×10^5

Literature for resistance:

1. Yu ea al. Appl. Phys. Lett. **87** 252904 (2005)
2. J. –G. Kim et al. J. Mater. Sci.: Mater.Electr. **16** 7 (2005)
3. Yang et al. J. Appl. Phys. **96** 7492 (2004)
4. Hari. et al. J. Mater. Sci.: Mater.Electr. **8** 15 (1997)
5. Victor et al. J. Appl. Phys. **94** 7702 (2003)
6. J. –G. Kim et al. J. Mater. Sci.: Mater.Electr. **15** 807 (2004)

References

[1] S. Yamamichi, et al. in proceedings of the International Electron Devices Meeting (IEEE, New York, 1995), P. 119

[2] S. Yamamichi, T. Sakuma, T. Hasse and Y. Miyasaka *Mater. Res. Soc. Symp. Proc.* **243** 297 (1992)

[3] L. A. Knauss, J. M. Pond, J. S. Horwitz, D. B. Chrisey, C. H. Mueller and R. Treece *Appl. Phys. Lett.* **69** 25 (1996)

[4] B. J. Gibbons, B. Park, Y. Gim, Y. Fan, A. T. Findikoglu, D. W. Reagor and Q. X. Jia *Integr. Ferroelectr.* **39** 1211 (2001)

[5] M. H. Yeh, Y. C. Liu, K. S. Liu, N. I. Lin, J. M. Lee and H. F. Cheng *J. Appl. Phys.* **74** 2143 (1993)

[6] O. Auciello and R. Ramesh *MRS Bulletin* **21** 31 (1996)

[7] L. S. Philips *Electron. Comp.* **12** 523 (1971)

[8] M. de Kejiser and G. J. M. Dormans *MRS Bulletin* **21** 37 (1996)

[9] B. A. Tuttle and R. W. Schwartz *MRS Bulletin* **21** 49 (1996)

[10] T. W. Kim and S. S. Yom *Appl. Phys. Lett.* **65** 15 (1994)

[11] S. B. Krupanidhi, N. Maffei, M. Sayer and K. El-Assal *J. Appl. Phys.* **54** 6601 (1983)

[12] M. R. Craven, W. M. Cranton, S. Total and H. S. Reehal *Semicond. Sci. Technol.* **13** 404 (1998)

[13] G. R. Fox, S. Trolier-McKinstry and S. B. Krupanidhi *J. Mater. Res.* **10** 1508 (1995)

[14] T. Sakuma, S. Yamamichi, S. Matsubara, H. Yamaguchi and Y. Miyasaka *Appl. Phys. Lett.* **57** 2431 (1990)

[15] C. N. Rao and G. V. Subba Rao, National Bureau of Standards Report No. NSRDS-NBS49, 1974

[16] L. Krusin-Elbaum and M. Wittmer *J. Electrochem. Soc.* **135** 2610 (1998)

[17] J. E. Bauerle *J. Phys. Chem. Solids* **30** 2657 (1969)

[18] X. Guo, C. Pithan, C. Ohly, C. -L. jia, J. Dornseiffer, F. –H. Haegel and R. Waser *Appl. Phys. Lett.* **86** 082110 (2005)

[19] M. H. Frey, Z. Xu, P. Han and D. A. Payne *Ferroelectrics* **206-207** 337 (1998)

[20] B. S. Kang and S. K. Choi *Appl. Phys. Lett.* **80** 103 (2002)

[21] B. S. Kang and S. K. Choi *Solid State Commun.* **121** 441 (2002)

[22] B. S. Kang and S. K. Choi *J. Mater. Res.* **17** 127 (2002)

[23] B. S. Kang, S. K. Choi and C. H. Park *J. Appl. Phys.* **94** 1904 (2003)

[24] K. Takemura, T. Sakuma and Y. Miyasaka *Appl. Phys. Lett.* **64** 2967 (1994)

[25] C. W. Law, K. Y. Tong, J. H. Li, K. Li and M. C. Poon *Thin Solid Films* **354** 162 (1999)

[26] D. Mergel, K. Thiele and Z. Qiao *J. Mater. Res*. **20** 2503 (2005)

[27] G. Y. Yang, E. C. Dickey, C. A. Randall, D. E. Barber, P. Pinceloup, M. A. Henerson, R. A. Hill, J. J. Beeson and D. J. Skamser *J. Appl. Phys.* **96** 7492 (2004)

[28] B. Prijamboedi, H. Takashima, R. Wang, A. Shoji and M. Itoh *Phys. Stat. Sol. (a)* **202** R152 (2005)

[29] C. Ang and Z. Yu *Phys. Rev. B* **61** 11363 (2000)

[30] W. Kleemann and H. Schremmer *Phys. Rev. B* **40** 7428 (1989)

[31] B. Karunagaran, S. J. Chung, E. –K. Suh and D. Mangalaraj *Physica B* **369** 129 (2005)

[32] V. Gupta and A. Mansingh *Phys. Rev. B* **49** 1989 (1994)

[33] H. Kleim *IEEE Trans. Electr. Insul.* **24** 185 (1989)

[34] R. Waser *Science and Technology of Electroceramic Thin Films* (Kluwer Academic, Dordrecht, The Netherlands 1995).

[35] C. L. Li, Z. H. Chen, Y. L. Zhou and D. F. Cui *J. Phys.: Condens. Matter.* **13** 5261 (2001)

[36] P. C. Joshi and S. B. Krupanidhi *J. Appl. Phys.* **73** 7627 (1993)

[37] T. Sawada and H. Hasegawa *Thin Solid Films* **56** 183 (1979)

[38] S-H. Paek, K-S. Lee, J-Y. Sung, S-Y. Son, C-S. Park and J-H. Chung *J. Mater. Sci. Lett.* **17** 95 (1998)

[39] J. Moulson and J. M. Herbert *Electronic Ceramics: Materials, Properties and Applications* (Chapman & Hall, New York, 1990)

[40] W. J. Kim, W. Chang, S. B. Qadri, J. M. Pond, S. W. Kirchoefer, D. B. Chrisey and J. S. Horwitz, *Appl. Phys. Lett.* **76** 1185 (2000)

[41] T. Schmizu *Solid State Commun.* **102** 523 (1997)

[42] W. Chang D.Sc. thesis in Material Science, School of Engineering and Applied Science, George Washington University (1999)

[43] R. Vest *Ferroelectrics* **53** 102 (1990)

[44] W. R. Buessem, L. E. Cross and A. K. Goswami *J. Am. Ceram. Soc.* **49** 33 (1966)

[45] N. A. Pertsev, A. G. Zembilgotov and A. K. Tagantsev *Phys. Rev. Lett.* **80** 1988 (1998)

[46] A. K. Tagantsev, N. A. Pertsev, P. Muralt and N. Setter *Phys. Rev. B* **65** 012104 (2002)

[47] K. –H. Hellwege and A. M. Hellwege, Eds., Landolt-Börnstein: *Numerical Data and Functional Relationship in Science and Technology* (Springer, Berlin, 1981), New Series-Group III, Vol. 16a, P. 67, 73 and 74

[48] L. L. Hench and J. K. West *Principles of Electronic Ceramics* (Wiley, New York P. 243 1990)

[49] Q. Feng and C. J. McConville *J. Am. Ceram. Soc.* **87** 1945 (2004)

[50] T. Takeuchi, E. Bétournè, M. Tabuchi, H. Kageyana, Y. Kobayashi, A. Coats, F. Morrison, D. C. Sinclair and A. R. West *J. Mater. Sci.* **34** 917 (1999)

[51] M. M. Saad, P. Baxter, R. M. Bowman, J. M. Gregg, F. D. Morrison and J. F. Scott *J. Phys.: Condens. Matter.* **16** L451 (2004)

[52] C. J. Johnson *Appl. Phys. Lett.* **7** 221 (1965)

[53] T. M. Shaw, Z. Suo, M. Huang, E. Liniger, R. B. Laibowitz and J. D. Baniecki *Appl. Phys. Lett.* **75** 2129 (1999)

[54] T. R. Taylor, P. J. Hansen, B. Acikel, N. Pervez, R. A. York, S. K. Streiffer and J. S. Speck *Appl. Phys. Lett.* **80** 1978 (2002)

[55] L. H. Parker and A. F. Trsch *IEEE Circuits Device Mag*. **6** 17 (1990)

[56] J. Zeng, H. Wang, M. Wang, S. Shang, Z. Wang and C. Lin *J. Phys. D: Appl. Phys.* **31** 2416 (1998)

[57] K. M. Ring and k. L. Kavanagh *J. Appl. Phys.* **94** 5982 (2003)

[58] E. J. H. Lee, M. Pontes, E. R. Leite, E. Longo, J. A. Varela, E. B. Araujo and J. A. Eiras *J. Mater. Sci. Lett.* **19** 1457 (200)

[59] B. Lee and J. Zhang *Thin Solid Films* **388** 107 (2001)

[60] Q. X. Jia, J. L. Smith, L. H. Chang and W. A. Anderson *Phil. Mag. B* **77** 163 (1998)

[61] S. K. Streiffer, C. Basceri, C. B. Parker, S. E. Lash and A. I. Kingon *J. Appl. Phys.* **86** 4565 (1999)

[62] M. Mahesh Kumar and M.L. Post *J. Appl. Phys.* **97** 114916 (2005)

[63] M. Li, A. Feteira and D.C. Sinclair *J. Appl. Phys.* **98** 084101 (2005)

[64] S. Sen, P. Pramanik and R.N.P. Choudhary *Appl. Phys. A* **82** 549 (2006)

[65] S. Saha and T.P. Sinha *J. Appl. Phys.* **99** 014109 (2006)

[66] M. Shen, Z. Dong, Z. Gan, S. Ge and W. Cao *Appl. Phys. Lett.* **80** 2538 (2002)

[67] F.M. Pontes, E.R. Leite, E. Longo, J.A. Varela, E.B. Araujo and J.A. Eiras *Appl. Phys. Lett.* **76** 2433 (2000)

6. Annealing effects on structural and dielectric properties of $Ba_{0.75}Sr_{0.25}TiO_3$ thin film capacitors with RuO_2 electrodes

Abstract

Three capacitors with $Ba_{0.75}Sr_{0.25}TiO_3$ as dielectric were prepared and submitted to different post heating treatments. The deposition and annealing (in oxygen and vacuum) results in a significant difference in the dielectric properties of $Ba_{0.75}Sr_{0.25}TiO_3$ thin films. The dielectric constant in the low-frequency region is found to be very large for the oxygen annealed film and small for the vacuum annealed film. For the as-deposited film the dielectric constant is relatively low (~500). Dielectric constant at low frequency is probably from the non-uniform charge accumulation at grain-boundaries.

6.1 Introduction

Thin films of $(Ba_xSr_{1-x})TiO_3$ (BST) are promising ferroelectrics for applications in future ultra-large scale integrated electronic circuits, e.g. dynamic random access memories (DRAM) [1] and tunable microwave device applications [2], because these materials show high insulating properties with large values of relative permittivity and low dielectric loss and large change in dielectric constant with an applied dc electric field [3]. $(Ba_xSr_{1-x})TiO_3$ thin films have been widely studied because of their high dielectric constant in thin film hybrid and integrated circuits [4,5,6] for above mentioned applications. The high relative dielectric constant of BST films can shrink the size of circuits and at the end it is easy to miniaturize the electronic devices into the nano-scale range.

$(Ba_xSr_{1-x})TiO_3$ thin films have been fabricated using various deposition techniques including excimer laser ablation [7], flash evaporation [8], chemical vapor deposition (CVD) [9], sol-gel processes [10] and rf magnetron sputtering [11]. The rf magnetron sputtering method has been demonstrated to be the most promising method, because it offers good reproducibility, uniformity and simplicity [12].

A large number of studies on the properties of perovskite thin films using noble metal electrodes including Pt have been reported [13]. The sputtered Pt electrode is known to have the disadvantage of hillock formation, which can electrically short-circuit the capacitor. To overcome this problem, RuO_2 is a promising conductive metallic oxide, due its low resistivity (about 40 μΩcm), excellent diffusion barrier properties, good thermal stability and high corrosion resistance [14,15]. There have been only a few studies on BST thin films with the application of RuO_2 as the electrodes [16]. There has been very limited study on $Ba_{0.75}Sr_{0.25}TiO_3$ thin film properties [17].

Substrate temperature and oxygen partial pressure could have a severe effect on the oxygen content of thin films. There are numerous reports that vacuum annealing can produce a deficiency in oxygen [18], while excess oxygen can be produced by annealing in oxygen [19].

There is very limited study on the annealing in vacuum and oxygen [20] on the $Ba_{0.75}Sr_{0.25}TiO_3$ thin film properties.

It is interesting to study the $Ba_{0.75}Sr_{0.25}TiO_3$ thin film properties under annealing in oxygen atmosphere. However, often large variations in the physical and structural properties of thin films are observed depending on their annealing treatment. It is generally recognized that post-deposition annealing can repair the oxygen vacancies and reduce the number of organic inclusions (i.e., from the sol-gel process) within the as-deposited BST thin films. In fact, the properties of thin films strongly dependence on the processing parameters to suit various technological requirements.

In this study, we examine $Ba_{0.75}Sr_{0.25}TiO_3$ thin films prepared by rf magnetron sputtering on different substrates and subjected to different annealing conditions to study their structural, stoichiometric and dielectric properties.

6.2 Experimental

$Ba_{0.75}Sr_{0.25}TiO_3$ thin films were prepared by rf magnetron sputtering in a Von Ardenne LS 500 S sputtering system. The sputter chamber was pumped down to 3.5 x 10^{-5} mbar, and the Ar+O_2 pressure was 1.2 x 10^{-2} mbar. A sintered and stoichiometric $Ba_{0.75}Sr_{0.25}TiO_3$ target (purity 99.99% and rf power 100 W) was sputtered in Ar and O_2 mixed atmosphere to deposit thin films at room temperature and at 700°C. The films were later annealed for 1 hour in vacuum or in oxygen (O_2 = 20 sccm) of samples CBS-0.75-1 and CBS-0.75-2, respectively. The as-deposited film without post-annealing is CBS-0.75-5. High purity (5N) Ar (50 sccm) and O_2 (10 sccm) gas mixtures were used. The p-type Si(100) (circular) wafer substrates of 25 mm diameter and 0.50 mm thickness were used and cleaned in ultrasonic bath. A SiO_2 layer was grown by thermal oxidation. The capacitor structure comprised RuO_2 as bottom (50 nm) and top layer (30 nm) electrodes. They are deposited by rf magnetron sputtering with a RuO_2 target (purity 99.99%, Ar 50 sccm and rf power 75 W) at substrate temperatures of 540°C and room temperature of bottom and top electordes. The area of the top electrode is 7 mm^2. The thickness of the $Ba_{0.75}Sr_{0.25}TiO_3$ films is 300 ± 20 nm.

The thickness of the $Ba_{0.75}Sr_{0.25}TiO_3$ thin films was determined with a profilometer (Dektak 6M stylus profiler), structure determination was carried out by x-ray diffraction, XRD (Siemens D5000 x-ray diffractometer) with Cu $K\alpha_1$ (λ = 1.5405 Å) radiation. The complex impedance was measured with a Solartron Schlumberger SI 1260 impedance/gain analyzer, the temperature and frequency dependent dielectric properties were measured from 20 to 200°C and 10 Hz to 10 MHz, respectively.

6.3 Results and discussion

In Table 6.1 the deposition and annealing parameters are summarized along with the dielectric properties of the $Ba_{0.75}Sr_{0.25}TiO_3$ thin film capacitors.

Sample	P [x10^{-2} mbar]	O_2 %	T_{sub}	d [nm]	ε_r			E_σ [meV]
					at 100 Hz	100 KHz	*RQ_p	
CBS-0.75-1	2.2	20	R.T (Ann. at 700°C in O_2=40%)	~305	143710	13682	17742	34
CBS-0.75-2	2.2	20	R.T (Ann. at 700°C in vaccum)	~300	11267	667	1094	17
CBS-0.75-5	2.4	20	As dep. 700°C	~315	-	1235	475	0

Table 6.1 The deposition parameters and dielectric permittivity of BST-0.75 capacitors

6.3.1 X-ray diffraction study

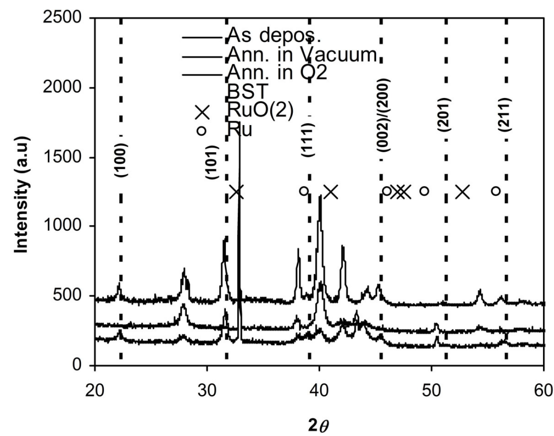

Fig. 6.1 XRD diffractogram of BST-0.75 thin films (vertical lines indicates BST-0.75 phases), top to bottom (As. dep., Ann. in Vac. and Ann. in O_2)

XRD results of $Ba_{0.75}Sr_{0.25}TiO_3$ thin films annealed in different conditions are shown in Fig. 6.1. It can be seen that (100), (101), (200) and (202) of the perovskite $Ba_{0.75}Sr_{0.25}TiO_3$ peaks can be observed. As deposited film (BST-0.75-5) and annealed in O_2 film (CBS-0.75-1) shows (100) and (200) preferred orientations and very weak (101) orientation. Film annealed in vacuum (BST-0.75-2) shows only (202) preferred orientation.

6.3.2 Impedance spectroscopy study

Complex impedance spectroscopy (IS) is a useful method in view of its simplicity and clarity in describing the electrical processes occurring in a system to characterize the electrical microstructure of ceramics and can allow the intrinsic (bulk) electrical properties to be distinguished from extrinsic contributions, such as grain boundaries, surface layers, and dielectric-electrode interfaces. The output response, when plotted in a complex plane plot, appears in the form of a succession of semicircles representing electrical phenomena due to bulk material, grain boundary effect and interfacial phenomena and gives the true bulk grain resistance [21]. The complex impedance can be plotted in a variety of complex plane formalisms, e.g., impedance Z^*, permittivity ε^*, or spectroscopic plots of the real and/or imaginary components. Complex IS has been quite well known for its applications in solid electrolyte conductivity determination, and its use has also long been extended to the studies of other solid dielectrics.

For many electroceramics the concept of a brick layer model consisting of uniform-sized grains separated by thin (high capacitance), insulating grain boundaries is appropriate, but it is only in ideal conditions, in general grains are non-uniform poly-grains. Each region can be realistically described by a parallel combination of a capacitor and resistor. The complex IS normally describes as $Z^* = Z' + jZ''$, where Z' and Z'' are real and imaginary parts of complex impedance.

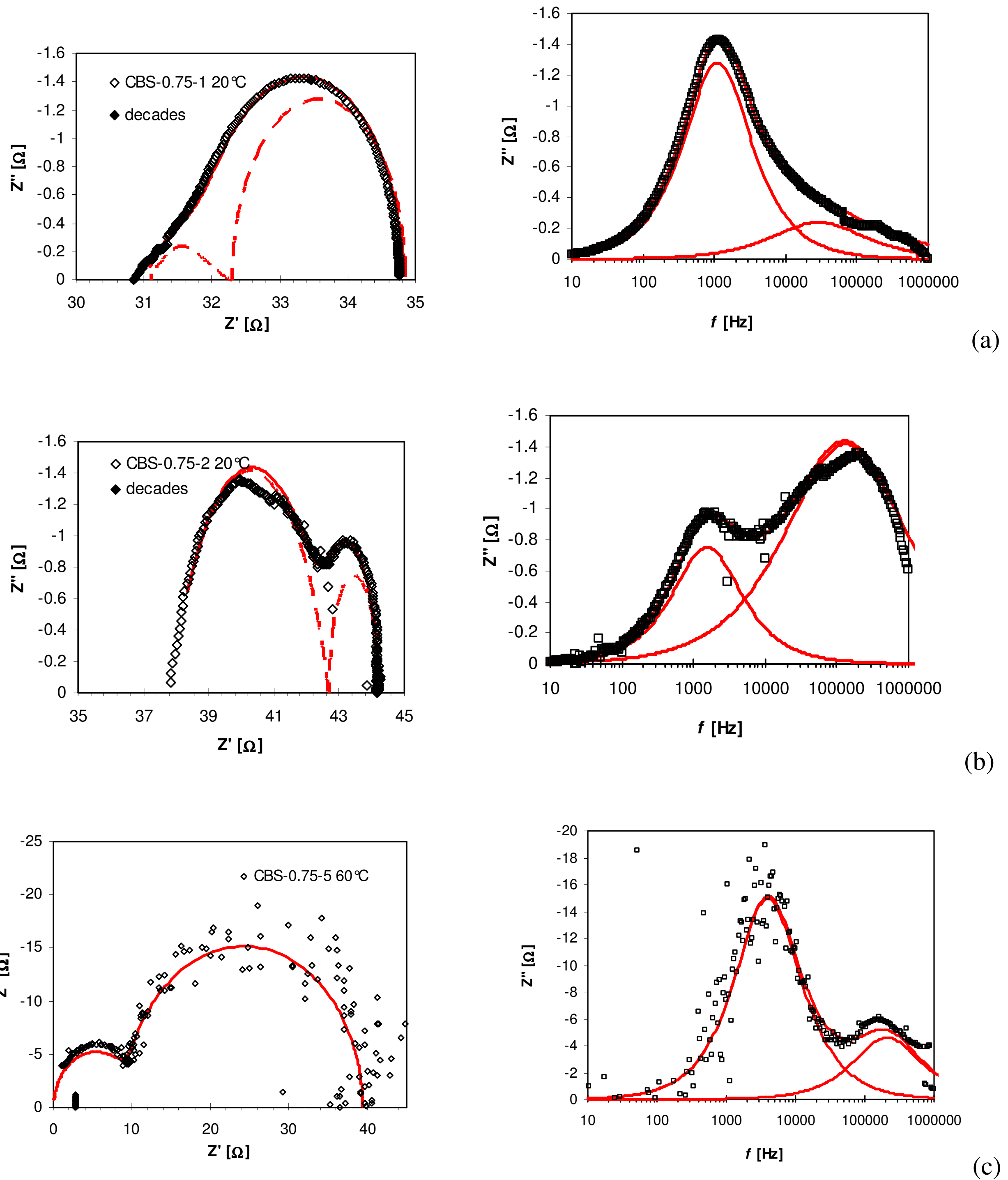

Fig. 6.2 Cole-Cole plot of BST-0.75 thin films along with simulated curve including deconvolution of high and low frequency curves (a) CBS-0.75-1 film annealed in O_2 (f_g=1.28x10^2, R=1.3 Ω, α=0.57), (b) CBS-0.75-2 film annealed in vacuum (f_g=1.6x10^3, R=4.8 Ω, α=0.67), (c) CBS-0.75-5 as deposited film at 700°C (f_g=2x10^5, R=10 Ω, α=1.0).

Fig. 6.2(a), (b) and (c) show the complex impedance of the samples CBS-0.75-1, CBS-0.75-2, and CBS-0.75-5, respectively. It can be observed that it is not an ideal semicircle and needs to be fitted with one R and two parallel RQ (RQ_p) elements connected in series. We assume that the high frequency RQ_p element represents the intragranular (bulk/grain) capacitance C_b and resistance R_b, and the medium frequency RQ element represents the intergranular (grain boundary, gb) capacitance, C_{gb}, and resistance, R_{gb}. This is based on the assumptions that $R_{gb} \gg R_g$ and that the permittivity of the bulk and grain-boundary regions are similar in size such that $C_{gb} \gg C_g$. Then the time constant (where $\tau = RC$) for the bulk element, τ_b, is much smaller than that of the grain-boundary element, τ_{gb}.

Each RQ_p element gives rise to an arc in the complex impedance plane plot Z^* and the electrical relaxation ($\omega\tau = 1$, where $\omega = 2\pi f$ and f is the applied frequency in Hz) occurs at much lower frequency for the grain boundary element compared to the bulk element. The diameter of the arcs represent the magnitudes of R_b and R_{gb}, and C_b and C_{gb} can be estimated using the relationship $\omega\tau = 1$ at the arc maxima ($\omega_{max} = 2\pi f_{max}$; $C = 1/2\pi R f_{max}$). Consequently, the characteristic frequency $f_g = (2\pi\tau)^{-1}$ is relatively smaller and the semicircle of the grain boundaries occurs at lower frequencies. The bulk grain resistance is determined from the high-frequency semicircle of the RC_p or RQ_p equivalent circuit. This procedure is well established in the literature. It has been applied in the case of many dielectric and ferroelectric materials [22,23].

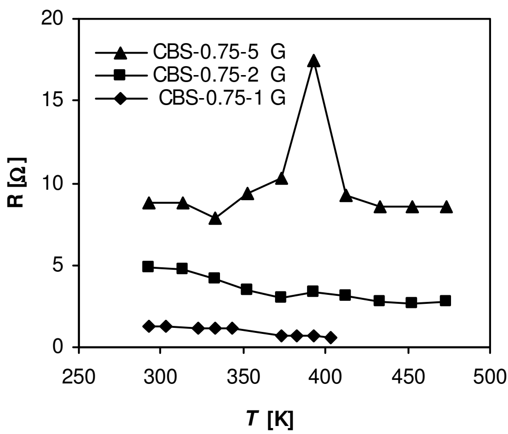

(a)

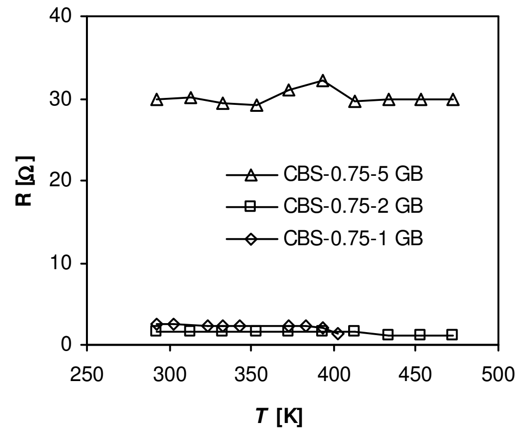

(b)

Fig. 6.3 Resistance of BST-0.75 films extracted from RQ simulations. (a) Grain, G and (b) grain boundary, GB.

In Fig. 6.3 the relationship of $R_{gb}>R_g$ vs. temperature is shown for the sample CBS-0.75-1, CBS-0.75-2 and CBS-0.75-5. The contribution from the grain boundaries plays an important role in the total insulation resistance of the capacitors. It is well established that deposition at higher oxygen pressure makes films more insulating [24,25].

The frequency-dependent relative dielectric constant (ε_r) as calculated from Eq. (1) [26,27] can be seen in Fig. 6.4.

$$\varepsilon_r = \frac{-Z''}{(2\pi f C_0)(Z'^2 + Z''^2)} \tag{1}$$

The Z'-value for $f \rightarrow \alpha$ was substracted from Z'(f). As a typical behavior, the dielectric constant is higher at lower frequencies and decreases with increasing frequency. Such behavior has been observed in many MIS systems [28] and various models have been proposed in terms of the frequency dispersion of the permittivity of the insulator film, the presence of a highly resistive interfacial layer or a density distribution of interface states.

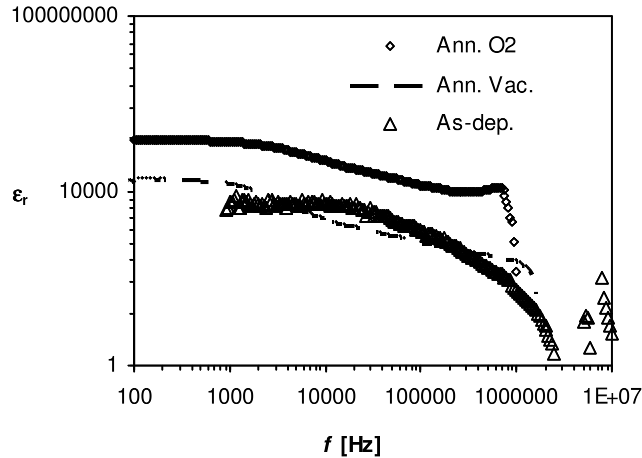

Fig. 6.4 Relative dielectric permittivity of BST-0.75 films calculated from Eq. (2) with respect to frequency.

The dielectric constant of our film annealed in oxygen shows is larger than those of the as-deposited film and the film annealed in vacuum.

The increase in the dielectric constant in the low frequency range is possibly due to the space charge polarization. This can be explained in other terms like Maxwell-Wagner type interfacial polarization or space charge polarization at grain boundaries, contributions from interfacial polarizability due to the presence of two layers of material of different conductivity. The space charge polarization is inherently related to the non-uniform charge accumulation. These charges can be originated during the post annealing treatment in an oxygen atmosphere. In polycrystalline ceramics, this kind of behavior is commonly observed when the grains are semiconducting and the grain boundaries are insulating. The actual mechanism in our sample is difficult to determine since all these could be source of the dispersion. In general interfacial polarization is relatively slow compared with other types of polarization (atomic, electronic, dipolar) produced by displacement or orientation of bound charge carriers, which can only affect the dielectric properties of the samples at a low frequency [29]. Such giant dielectric permittivity at lower frequencies has been observed for dielectrics: e.g. ($CaCuTi_4O_{12}$) [30], ferroelectrics: e.g., ($BaTiO_3$:Nb) [31] and composite materials: e.g., ($Ni_{0.8}Zn_{0.2}Fe_2O_4/Sr_{0.5}Ba_{0.5}Nb_2O_6$) [32].

The sharp decrease at higher frequencies is due to the fact that we observe non-zero resistance when the frequency approaches the high-frequency limit; but the imaginary part vanishes. This leads to vanishing ε_r, according to Eq. (2).

When the resistance of the grain boundaries is much larger than that of the grains then the ε_r calculated from Eq. (2) is too large by a factor corresponding to the ratio of the thickness of the grains to that of the grain boundaries.

Around 10 kHz, all spectra exhibit a step. According to our model, the *RQ*-element of the grains dominates the spectra. Following the discussion above, only the value at 100 kHz is physically meaningful. It is attributed to the bulk grains. In this case, the assumed thickness of the dielectric layer and consequently the value of the empty capacitance (C_0 in Eq. (2)) was correct.

Post annealing in an oxygen atmosphere increased the dielectric constant while a small dielectric constant was observed for the vacuum annealed film.

Pontes et al. [33] and Shen et al. [34] observed that when films are annealed in oxygen there is an increase of the dielectric constant in the low-frequency region. This is because the oxygen atoms segregate into the grain boundaries and forms interface layers with high resistance, so the interface conductivity is different from the bulk conductivity. These phenomena can be explained as the space charge polarization is inherently related to the non-uniform charge accumulation.

We calculated the bulk ε_r from the high frequency semicircle of the simulations of the complex impedance attributed to the bulk capacitance values from the equation Eq (2), (where $C=1/2\pi Rf_{max}$)

$$\varepsilon_r = \frac{Cd}{\varepsilon_0 A} \tag{2}$$

where C is the capacitance, d is the thickness of the film, ε_0 is the permittivity of vacuum (8.854 x 10^{-12} F/m), and A is the area of the electrode (7.07 mm^2).

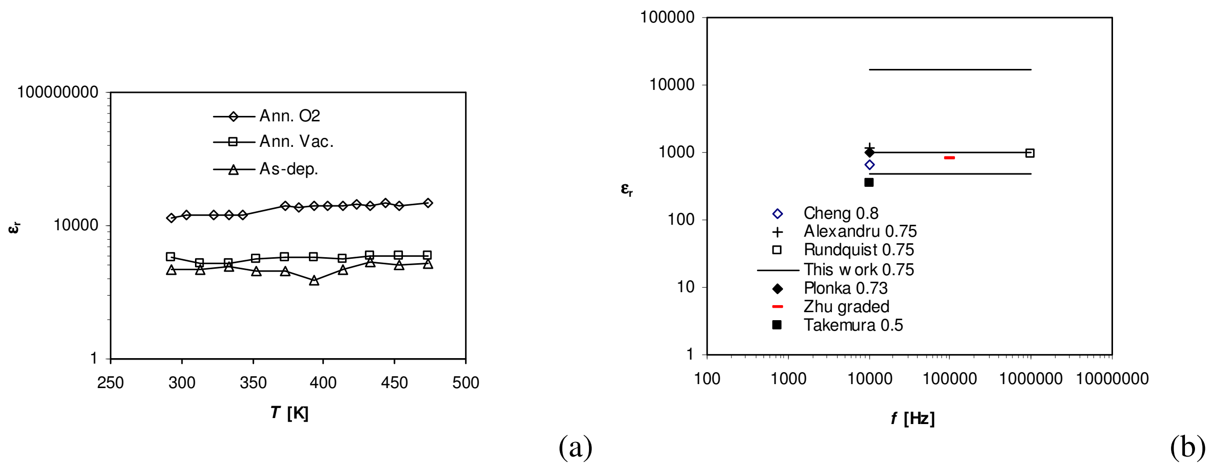

Fig. 6.5 (a) Dielectric permittivity of bulk grains of BST-0.75 films calculated from RQ simulations with respect to temperature, (b) literature comparison.

The ε_r values are plotted with respect to the measured temperature in Fig. 6.5(a). From this figure it is very clear that, at about 140°C there is trend for all films, increasing the ε_r values.

The ε_r values of our films are well consistent with literature values can be found in Fig. 6.5(b): Cheng et al. [35] observed ε_r ~650 for $Ba_{0.80}Sr_{0.20}TiO_3$ thin films prepared by the sol-gel process. This result is good agreement with our as-deposited film. Takemura et al. [36] observed for ~100 nm $Ba_{0.50}Sr_{0.50}TiO_3$ thin films with RuO_2 electrodes, ε_r very close to our values for as deposited film (ε_r ~360 at 10 kHz). They also observed that on RuO_2 electrodes the ε_r values are higher than on Pt or Pd electrodes. Zhu et al. deposited thin films of graded BST (pulsed laser deposition) under different oxygen partial pressures and observed ε_r from 300 to 900. Alexandru et al. [37] also observed for $Ba_{0.75}Sr_{0.25}TiO_3$ prepared by standard solid state reaction technology that the ε_r values are 1200 at 10 kHz. For $Ba_{0.73}Sr_{0.27}TiO_3$ thin films (120 nm thickness) ε_r values about 1000 (at 10 kHz) are observed by Plonka et al. [38]. Rundquist et al. [39] observed ε_r maximum values about 940 at 1 MHz for $Ba_{0.75}Sr_{0.25}TiO_3$ thin films with thickness of 280 nm.

These results indicate that, annealing (in oxygen or vacuum) will improve the dielectric properties. But an in depth study is necessary to understand the actual mechanism in the improving the dielectric properties by annealing.

Conductivity (σ)

The bulk conductivity of the material has been evaluated from the complex impedance plots of the CBS-0.75 samples at different temperatures and is depicted in Fig. 6.6.
At higher temperatures, the bulk conductivity versus temperature (1000/*T*) is linear and can be explained by a thermally activated transport of Arrhenius type governed by the relation:

$$\sigma = \sigma_0 \exp\left(-\frac{E_\sigma}{kT}\right) \quad (3)$$

where σ_0 and E_σ are conductivity at higher temperature and the activation energy of the mobile charge carriers, respectively.

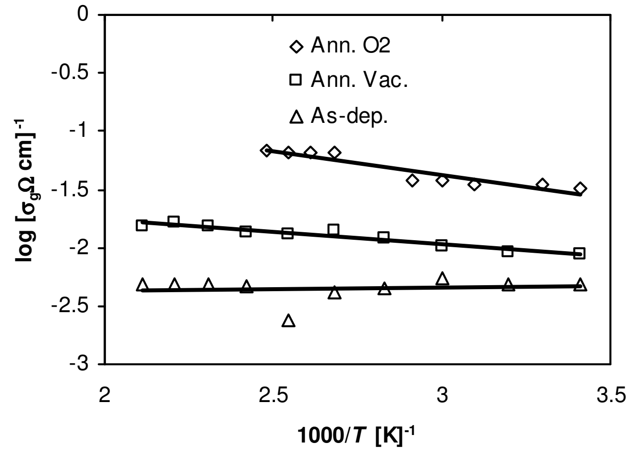

Fig. 6.6 Arrhenius plot of bulk conductivity

Over the temperature range of 273 to 493 K the conductivity reveals linear behavior with essentially the same activation energy between 0 to 34 meV. The activation energies of conductivity and relaxation times are relatively low. Such low activation energies have also been observed in the literature for different materials: 4 to 11 meV for $SrTiO_3$ [40], 33 to 62 meV for $(Sr,Bi)TiO_3$ [41], 12 meV for $(Sr,Ca)TiO_3$ [42], and 100 meV for TiO_2 [43]. Such small activation energies have been attributed to hopping of electrons between traps generated e.g. by off-centre defects.

Dielectric loss (tan δ)

The dielectric loss (tan δ) of the capacitors was calculated from, The Z'-value for $f \rightarrow \alpha$ was substracted from Z'(f):

$$\tan\delta = -\frac{Z'}{Z''} \quad (4)$$

where Z' and Z'' are the real and imaginary part of the complex impedance, respectively. Our results are shown in Fig. 6.7.

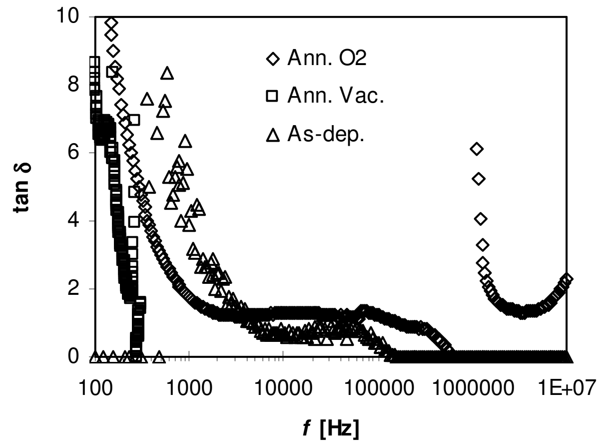

Fig. 6.7 Dielectric loss (tan *δ*) vs. frequency

The film annealed in oxygen and the film deposited at 700°C high show lower dielectric loss compared with the film annealed in vacuum. This can be explained with the assumption that films annealed in oxygen or deposited at high substrate temperature have a lower defect density compared with films annealed in vacuum, where there are more chances to have large defect density, especially of oxygen defects.

6.4 Conclusions

In conclusion, the deposition and annealing (in oxygen and vacuum) results in a significant difference in the dielectric properties of BST-0.75 thin films. The dielectric constant in the low-frequency region found to be very large for oxygen annealed film and small for vacuum annealed film. For the as-deposited film the dielectric constant is low. Dielectric constant at low frequency is probably from the non-uniform charge accumulation at grain-boundaries. For all films there is a relaxation step at 10 kHz. The dielectric constant at 100 kHz for oxygen annealed about 13000, vacuum annealed film is about 660 and for as deposited film is about 1235. The dielectric permittivity of bulk at room temperature for the oxygen annealed film is ~17000, this value is larger than for the other two samples: annealed in vacuum and as-deposited films ε_r values are ~1090 and ~470 at room temperature. Above 140°C the ε_r values

increased up. But an in depth analysis is necessary to understand the annealing effects in $Ba_{0.75}Sr_{0.25}TiO_3$ thin films.

References

[1] S. Yamamichi, T. Sakuma, T. Hasse and Y. Miyasaka *Mater. Res. Soc. Symp. Proc*. **243** 297 (1992)

[2] L. A. Knauss, J. M. Pond, J. S. Horwitz, D. B. Chrisey, C. H. Mueller and R. Treece *Appl. Phys. Lett.* **69** 25 (1996)

[3] B. J. Gibbons, B. Park, Y. Gim, Y. Fan, A. T. Findikoglu, D. W. Reagor and Q. X. Jia *Integr. Ferroelectr*. **39** 1211 (2001)

[4] M. H. Yeh, Y. C. Liu, K. S. Liu, N. I. Lin, J. M. Lee and H. F. Cheng *J. Appl. Phys.* **74** 2143 (1993)

[5] R. Liedtke, M. Grossman and R. Waser *Appl. Phys. Lett.* **77** 2045 (2000)

[6] A. I. Kingon, J. P. Maria and S. K. Streiffer *Nature* (London) **406** 1032 (2000)

[7] O. Auciello and R. Ramesh *MRS Bulletin* **21** 31 (1996)

[8] L. S. Philips *Electron. Comp.* **12** 523 (1971)

[9] M. de Kejiser and G. J. M. Dormans *MRS Bulletin* **21** 37 (1996)

[10] B. A. Tuttle and R. W. Schwartz *MRS Bulletin* **21** 49 (1996)

[11] S. B. Krupanidhi, N. Maffei, M. Sayer and K. El-Assal *J. Appl. Phys.* **54** 6601 (1983)

[12] M. R. Craven, W. M. Cranton, S. Total, and H. S. Reehal *Semicond. Sci. Technol*. **13** 404 (1998)

[13] X. –H. Zhu, H. L. –W. Chan, C. –L. Choy, K. –H. Wong *Appl. Phys. A* **80** 591 (2005)

[14] C. N. Rao, and G. V. Subba Rao, National Bureau of Standards Report No. NSRDS-NBS49, 1974

[15] L. Krusin-Elbaum and M. Wittmer *J. Electrochem. Soc.* **135** 2610 (1998)

[16] S. –H. Paek, K. –S. Lee, J. –Y. Sung, S. –Y. Son, C. –S. Park and J. –H. Chung *J. Mater. Sci. Lett.* **17** 95 (1998)

[17] S. A. Nasser and D. A. Payne *Phil. Mag.* B **80** 1153 (2000)

[18] H. L. Ju, J. Gopalakrishnan, J. L. Peng, Q. Li, G. C. Xiong, T. Venkatesan and R. L. Greene *Phys. Rev. B* **51** 6143 (1995)

[19] W. Prellier, M. Rajeswari, T. Venkatesan and R. L. Greene *Appl. Phys. Lett*. **75** 1446 (1999)

[20] S. J. Chang, J. S. Lee, M. C. Wei, J. F. Chen, C. H. Liu and U. H. Liaw *J. Vac. Sci. Tech. A* **20** 107 (2002)

[21] J. R. Macdonald *Impedance Spectroscopy*, Willey, New York (1987)

[22] M. Mahesh Kumar and M.L. Post *J. Appl. Phys.* **97** 114916 (2005)

[23] S. Sen, P. Pramanik and R.N.P. Choudhary *Appl. Phys. A* **82** 549 (2006)

[24] H. Beltràn, E. Cordoncillo, P. Escribano, D. C. Sinclair and A. R. West *J. Appl. Phys*. **98** 094102 (2005)

[25] S. Jayanthi and T. R. N. Kutty *J. Mater. Sci.* **16** 269 (2005)

[26] J. Yu, T. Ishikawa, Y. Arai, S. Yoda, M. Itoh, Y. Saita *Appl. Phys. Lett*. **87** 252904 (2005)

[27] J. E. Diosa, R. A. Vargas, I. Albinsson, B. –E. Mellander *Solid State Commun.* **136** 601(2005)

[28] P. C. Joshi and S. B. Krupanidhi *J. Appl. Phys* **73** 7627 (1993)

[29] J. D. Yu, P. F. Paradis, T. Ishikawa and S. Yoda *Appl. Phys. Lett*. **85** 2899 (2004)

[30] C. C. Homes, T. Vogt, S. M. Shapiro, S. Wakimoto and A. P. Ramirez *Science* **293** 673 (2001)

[31] M. Maglione and M. Belkaoumi *Phys. Rev. B* **45** 2029 (1992)

[32] Y. J. Li, X. M. Chen, R. Z. Hou and Y. H. Tang *Solid State Commun.* **137** 120 (2006)

[33] F. M. Pontes, E. R. Leite, E. Longo, J. A. Varela, E. B. Araujo and J. A. Eiras *Appl. Phys. Lett.* **76** 2433 (2000)

[34] M. Shen, Z. Dong, Z. Gan, S. Ge and W. Cao *Appl. Phys. Lett* **80** 2538 (2002)

[35] J.-G. Cheng, X.-J. Meng, J. Tang, S.-L. Guo and J.-H. Chu *Appl. Phys. A* **70** 411 (2000)

[36] K. Takemura, T. Sakuma and Y. Miyasaka *Appl. Phys. Lett* **64** 2967 (1994)

[37] H. V. Alexandru, C. Berbecaru, F. Stanculescu, A. Ioachim, M. G. Banciu, M. I. Toacsen, L. Nedelcu, D. Ghetu and G. Stoica *Mater. Sci. Eng. B* **118** 92 (2005)

[38] R. Plonka, R. Dittmann, N. A. Pertsev, E. Vasco and R. Waser *App. Phy. Lett*. **86** 202908 (2005)

[39] P. Rundqvist, Ph. D thesis, Chalmers University of Technology, Page. 28 (2006)

[40] B. Prijamboedi, H. Takashima, R. Wang, A. Shoji and M. Itoh *Phys. Stat. Sol. (a)* **202** R152 (2005)

[41] C. Ang and Z. Yu *Phys. Rev. B* **61** 11363 (2000)

[42] W. Kleemann and H. Schremmer *Phys. Rev. B* **40** 7428 (1989)

[43] B. Karunagaran, S. J. Chung, E. –K. Suh and D. Mangalaraj *Physica B* **369** 129 (2005)

7. Dielectric properties of $BaTiO_3$ / $SrTiO_3$ and $BaTiO_3$ / $Ba_{0.75}Sr_{0.25}TiO_3$ thin film heterostructures with RuO_2 electrodes

Abstract

Thin film capacitors with several layers of $BaTiO_3$/$SrTiO_3$ and $BaTiO_3$/ $Ba_{0.75}Sr_{0.25}TiO_3$ as dielectric were fabricated by rf magnetron sputtering. The properties of the capacitors were investigated as a function of the heterostructure periodicity. The dielectric constant increased with decreasing the individual layer thickness of $BaTiO_3$/$SrTiO_3$. The dielectric constant was significantly enhanced up to ~100000 for the $BaTiO_3$/ $Ba_{0.75}Sr_{0.25}TiO_3$ system. This is thought to be an artifact produced by space charge regions due to carrier migration to the interfaces within the dielectric.

7.1 Introduction

Perovskite thin films are forerunner in science and technology to miniaturization of the electronic devices. In recent years there is a great attention on perovskite type thin films for applications as dynamic and ferroelectric random access memories (DRAM and FeRAM), sensors, and microwave devices. Therefore, extensive research has been carried out to obtain large dielectric constant and non-linear dielectric properties for thin film ferroelectric devices. There is a great interest to enhance the properties of the most promising and typical ferroelectric materials such as $BaTiO_3$ (BTO) and $(Ba_xSr_{1-x})TiO_3$ (BST) by strain that is induced with different deposition methods. One possibility is the production of hetero-structures with different perovskite materials.

Plenty of theoretical and experimental results have revealed that the lattice strain induces an enhancement of the polarization and the relative dielectric constant of heterostructures. BTO or BST films on $SrTiO_3$ (STO) substrates increase their polarization [1] which is explained by the strain caused by the lattice mismatch between BTO and STO. Heterostructures of BTO and STO enhance the dielectric constant [2,3]. By changing the layer stack thicknesses of BTO/STO and BTO/ STO/ CTO ($CaTiO_3$), Shimuta et al. and Lee et al. [4] observed an increase of the polarization by a factor of three and 50% compared to a homogeneous single BTO film. Erbil et al. [5] deposited heterostructures of $PbTiO_3$ and $PbLaTiO_3$ and observed a giant dielectric constant of 420,000 at lower frequencies which they explained with the rigid body motion of ferroelectric domain walls. Qu et al.[6] reported a shift of the dielectric maximum to higher frequency with increasing measuring temperature, similar to the dielectric response relaxors. Catalan et al. [7] have tried to explain the anomalous dielectric properties of ferroelectric superlattices by means of a Maxwell-Wagner series capacitor model.

To manipulate the strain in a wide range, Kim et al [8] demonstrated that the dielectric constant and its non-linearity of BTO and STO reached a maximum at a certain degree of lattice distortion. Remarkable enhancement of voltage tunability (94%) has been achieved by Kim et al. [9] in BTO/STO super lattice system at the periodicity of each two unit cell. Several theoretical

calculations [10,11] based on first principle calculations, predicted that significant enhancement of the polarization can be achieved in perovskite oxide superlattices through larger misfit strain.

Although the dielectric constant response of ferroelectric superlattices does indeed resemble that of relaxors, it was recently observed that the appearance of dielectric enhancement and frequency relaxation could be correlated to the onset of Maxwell-Wagner (MW) behavior [12], suggesting that the observed relaxation and dielectric enhancement may be artifacts of carrier migration.

There are several reports on oxygen vacancies which play a pivotal role in structural and electrical properties of perovskite films. Oxygen vacancies will enhance the polarization, dielectric permittivity [13] and quality factor (Q=1/tan δ) [14] of the perovskite films. Kim et al. [13] also observed that the measured dielectric constant increases gradually as the strain goes from compressive strain (-0.14%) to tensile strain (0.12%), as determined from the lattice constant. An increased number of oxygen vacancies, increased the total polarizability by increasing the number of defect dipoles [15] and consequently the ionic polarizability.

A large number of studies on the properties of perovskite thin films using noble metal electrodes including Pt have been reported [16]. The sputtered Pt electrode is known to have the disadvantage of hillock formation, which can electrically short-circuit the capacitor. To overcome this problem, RuO_2, a conductive metallic oxide, was suggested as electrode material due its low resistivity (about 40 μΩcm), excellent diffusion barrier properties, good thermal stability and high corrosion resistance [17,18]. There have been only a few studies on perovskite thin films with the application of RuO_2 as electrodes [19].

In this study, heterostructures of $BaTiO_3$ (BTO)/$SrTiO_3$ (STO) and $BaTiO_3$ (BTO)/$Ba_{0.75}Sr_{0.25}TiO_3$ (BST-0.75) thin films are fabricated on substrates of RuO_2/SiO_2/p-Si and $RuO_2/TiO_2/SiO_2$/p-Si (one film). To the best of our knowledge it is the first time to attempt to study this combination.

7.2 Experimental

The films were fabricated by radio-frequency (rf) magnetron sputtering of $BaTiO_3$, $SrTiO_3$ and $Ba_{0.75}Sr_{0.25}TiO_3$ sputter targets with a diameter of 90 mm. The substrates were $RuO_2/SiO_2/Si$ or $RuO_2/TiO_2/SiO_2/Si$. The sputter chamber pressure is pumped down initially to $3x10^{-6}$ mbar but increases up to $3.5x10^{-5}$ mbar when the substrates are heated to 700°C. Later 50 sccm argon was introduced and the chamber pressure is $1.5x10^{-2}$ mbar during sputtering. The substrates were heated up to 700°C and the targets were pre-sputtered 15 min with argon.

Two kinds of heterostructures were deposited: BTO/STO and BTO/BST-0.75. The starting layer for both is BTO. These heterostructures were deposited in three different layer stacks; 5 x (30/30 nm), 3 x (50/50 nm), and 1 x (150/150 nm). For all films the total thickness was 300±20 nm; details can be found in Tables 7.1 and 7.2.

Table 7.1

Sample	P [x10^{-2} mbar]	T_{sub}	Stacks	d [nm]	ε_r at 100 Hz	ε_r 10 KHz	ε_r $^*RC_p$	R [Ω] Total
C-H-B-S-3	1.6	600°C	30/30	~290	355	297	461	65
C-H-B-S-1	1.7	600°C	50/50	~280	242	212	324	170
C-H-B-S-2	1.7	600°C (TiO_2)	50/50	~305	462	267	301	300
C-H-B-S-6	3.0	600°C	150/150	~277		145	224	200

Table 7.2

Sample	P [x10^{-2} mbar]	T_{sub}	Stacks	d [nm]	ε_r at 100 Hz	ε_r 10 KHz	ε_r $^*RC_p$	R [Ω] Total
C-B-BS-1	3.9	600°C	30/30	~312	9447	5676	9548	2000
C-H-B-BS-1	2.0	700°C	30/30	~307	10497	10483	7000	9
C-H-B-BS-3	1.6	700°C	50/50	~305	6303	3397	500	8
C-H-B-BS-5	1.5	700°C	50/50 in N_2	~300	572	66	67	180
C-H-B-BS-2	2.0	700°C	150/150	~300	-	9695	9544	30

Table 7.1 and **7.2** deposition parameters of C-H-B-S and C-H-B-BS system, respectively

The crystalline phase of the thin films was identified by x-ray diffraction (XRD) with a Philips 1760 powder diffractometer equipped with filtered Co Lα radiation (1.7902 Å). The film thickness was measured with a profilometer (Tencor Alpha-Step 500). For the study of the electrical properties of the hetero-structures we used impedance spectroscopy with a Solartron Schlumberger SI 1260 impedance/gain analyzer in the frequency range 10 Hz to 10 MHz and in the temperature range 20°C to 200°C.

7.3 Results and discussion

7.3.1 Phase analysis

Fig. 7.1 show the XRD patterns of BTO/STO and BTO/BST-075 heterostructure thin films, respectively. All films are polycrystalline with a perovskite structure. References (vertical lines) for the various phases are taken from Powder Diffraction File (PDF) data for BTO, STO, BST-0.75 and RuO_2. The lattice constant of the BTO cubic phase is ($a = b = c = 4.03$ Å, PDF: 31-174), that of cubic STO ($a = b = c = 3.91$ Å, PDF: 35-734) and those for BST-0.75 ($a = b = 3.997$ Å and $c = 3.9883$ Å, PDF: 44-93). The peaks of the various materials indicated by different vertical lines and symbols can be noticed in figure legends.

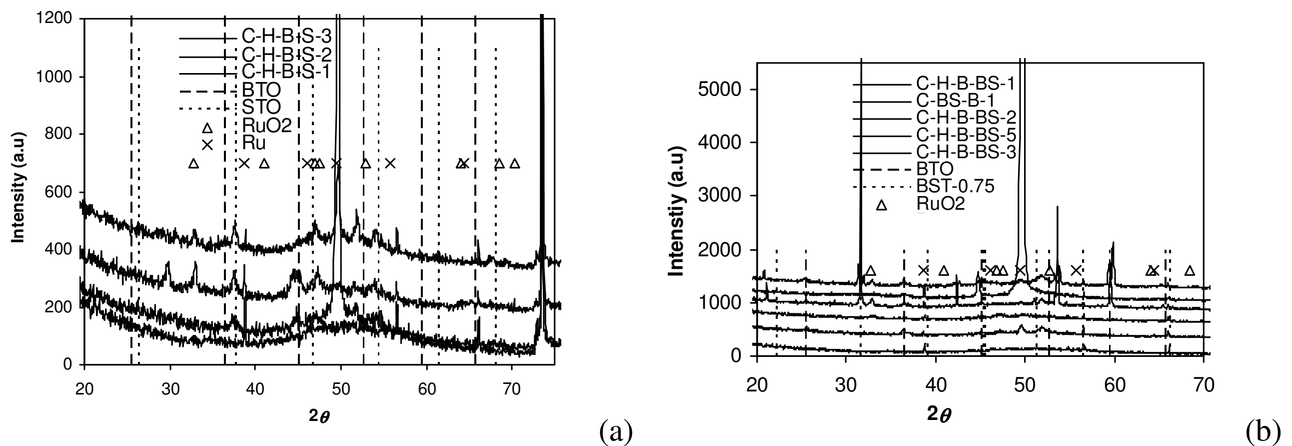

Fig. 7.1 XRD diffractograms of the heterostructures (a) C-H-B-S series (b) C-H-B-BS series

7.3.2 Impedance data

The resistance R and the capacitance C values of electrically active grain and grain boundary regions in many electroceramics can be estimated by complex impedance spectroscopy (IS). The complex impedance is normally described as $Z^* = Z' + jZ''$, where Z' and Z'' are the real and the imaginary part of the complex impedance, respectively.

The experimental data can often be modeled with an equivalent circuit consisting of two parallel RC_p or RQ_p elements connected in series, one RC_p or RQ_p element for the bulk and the other for the grain boundary response. For such a circuit, each RC_p or RQ_p element gives rise to ideally a semicircular arc in impedance complex plane plots, Z^* and a plateau in spectroscopic plots of the real component of the permittivity. RQ_p means a parallel circuit of a resistance R and a constant phase element (CPE), Q. The impedance of a Q-element is given by $Z = A\cdot(\mathrm{i}\omega)^{-1}$.

For many electro-ceramics the concept of a brick layer model consisting of uniformly-sized grains separated by thin high capacitance, insulating grain boundaries is appropriate [20]. Each region (grain or grain boundary) can be realistically described by a parallel combination of a capacitor and resistor. The position of the arcs in the frequency spectrum depends on their relaxation time, τ, where $\tau = RC = \rho\varepsilon\varepsilon_0$. At the arc maxima, the relationship $\omega_{max}RC = 1$ holds, where $\omega_{max} = 2\pi f_{max}$, and f is the applied frequency in Hz. In general, τ for grain boundary regions is much larger than for the bulk and the grain boundary response is relaxed out at lower frequencies than the bulk effects. Often, RC elements have ω_{max} that lie outside the available frequency range, especially if they represent either insulating regions with high R (ω_{max} smaller than minimum measuring frequency) or semiconducting regions with low R (ω_{max} bigger than maximum measuring frequency). In such cases, only parts of the arcs can be observed. Consequently, the characteristic frequency $f_g = (2\pi\tau)^{-1}$ is relatively smaller and the semicircle of the grain boundaries occurs at lower frequencies. The bulk grain resistance is determined from the high-frequency semicircle of the RQ_p equivalent circuit. This procedure is well established in

the literature. It has been applied in the case of many dielectric and ferroelectric materials [21,22].

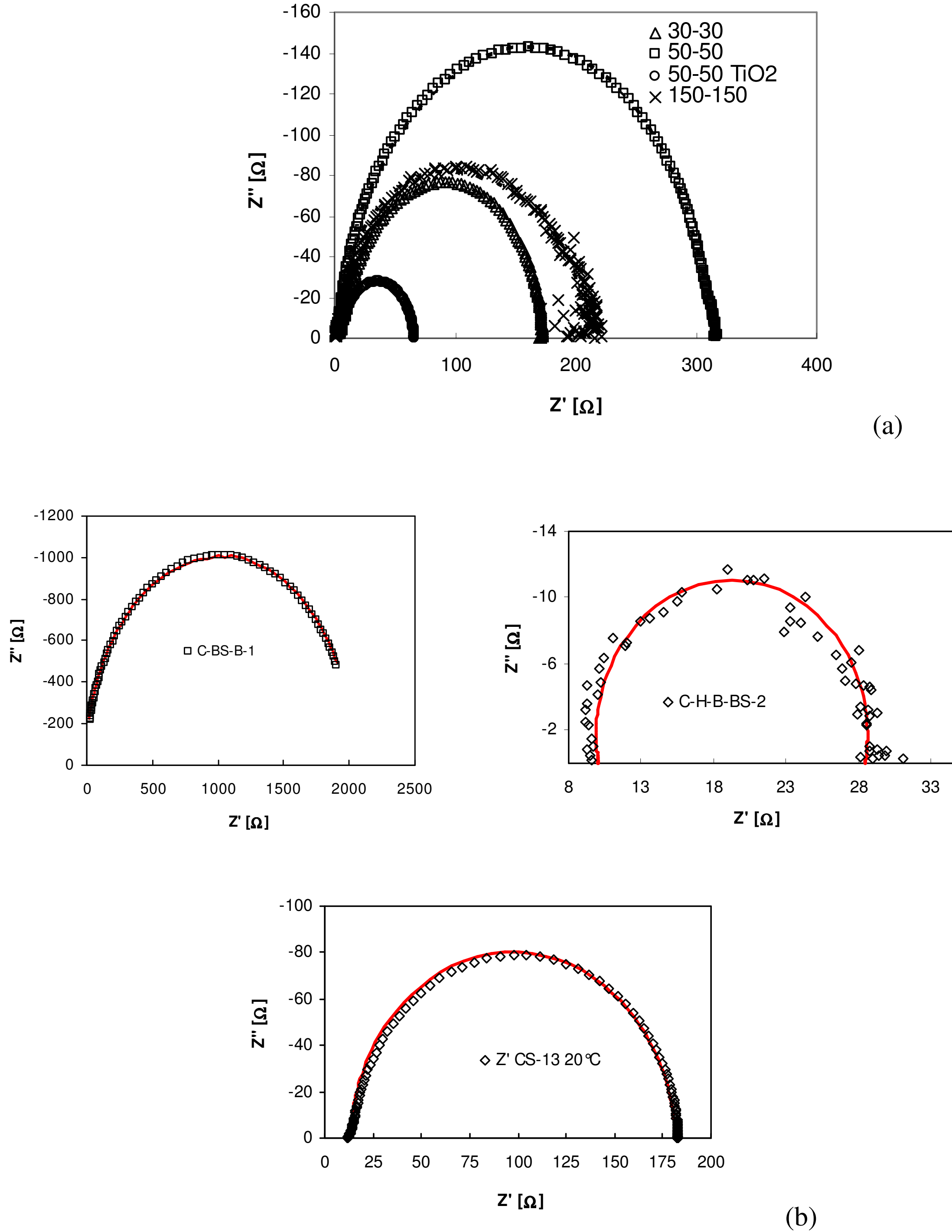

Fig. 7.2 Cole-Cole plots of heterostructures (a) C-H-B-S series (BTO/STO) together with the simulated curve (dashed lines) (b) C-H-B-BS (BTO/BST) heterostructures together with the simulated curve (red).

Fig. 7.2 (a) shows the complex impedance of the samples C-H-B-S-1, 2, 3 and 6 measured at room temperature. It can be observed that these are not ideal semicircles and need to be fitted with two RQ_p elements connected in series.

The frequency-dependent relative dielectric constant (ε_r) was calculated from Eq. (1) [23,24]:

$$\varepsilon_r = \frac{-Z''}{(2\pi f C_0)(Z'^2 + Z''^2)} \tag{1}$$

It can be seen in Fig. 7.3 (b). As a typical behavior, the dielectric constant is much higher at lower frequencies and decreases with increasing frequency. Such behavior has been observed in many MIS systems [25] and various models have been proposed in terms of the frequency dispersion of the permittivity of the insulator film, the presence of a highly resistive interfacial layer or a highly density distribution of interface states.

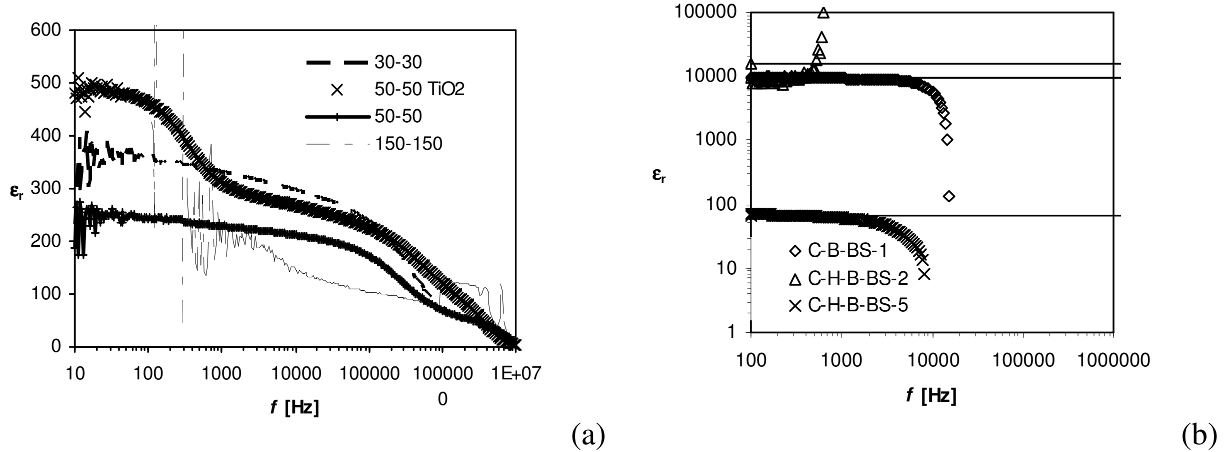

Fig. 7.3 Relative dielectric permittivity calculated from Eq. (1) with respective frequency of the (a) C-H-B-S series (b) C-H-B-BS series heterostructures

The increase in the dielectric constant in the low frequency range is possibly due to the space charge polarization, i.e., grain boundaries. This can be explained in other terms like Maxwell-Wagner type interfacial polarization or space charge polarization, contributions from interfacial polarizability due to the presence of two layers of material of different conductivity.

The sharp decrease at higher frequencies is due to the fact that we observe non-zero resistance when the frequency approaches the high-frequency limit and the imaginary part vanishes. This leads to vanishing ε_r, according to Eq. (1). In general interfacial polarization is relatively slow compared with other types of polarization (atomic, electronic, dipolar) produced by displacement or orientation of bound charge carriers, which can only affect the dielectric properties of the samples at a low frequency [26]. Such giant dielectric permittivity observed at lower frequencies for several dielectrics ($CaCu Ti_4O_{12}$) [27], ferroelectrics ($BaTiO_3$:Nb) [28] and composite materials ($Ni_{0.8}Zn_{0.2}Fe_2O_4/Sr_{0.5}Ba_{0.5}Nb_2O_6$) [29].

From Fig. 7.3(a) it can be observed that for all samples there is a plateau from 10 to 100 kHz, which can be attributed to the permittivity of the bulk grains.

The bulk conductivity of the material has been evaluated from the complex impedance plots of the C-H-B-S samples at different temperatures and is depicted in Arrhenius plot in Fig. 7.4. At higher temperatures, the bulk conductivity versus temperature (1000/*T*) is linear and can be explained by a thermally activated transport of Arrhenius type governed by the relation:

$$\sigma = \sigma_0 \exp\left(-\frac{E_a}{kT}\right) \tag{2}$$

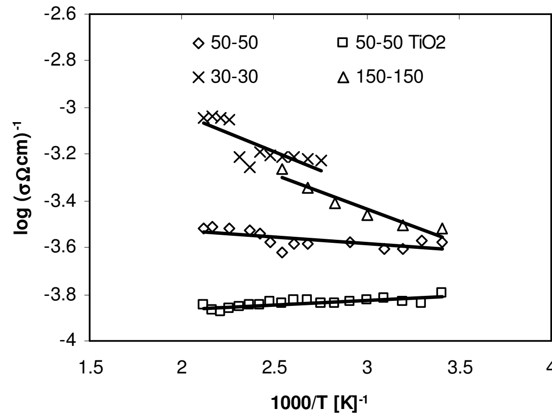

Fig. 7.4 Arrhenius plot of bulk conductivity of C-H-B-S series heterostructures

where σ_0 and E_σ, are conductivity at higher temperature, the activation energy of the mobile charge carriers, respectively. From the figure it can be seen that 30/30 layer stack show high conductivity. With increasing the stack thickness the conductivity goes lower.

The activation energies are very low, 0 to 27 meV, but comparable with other perovskite materials. The activation energies of conductivity and relaxation times are relatively low. Such low activation energies are also observed for different material systems in the literature: 4 to 11 meV for $SrTiO_3$ [30], 33 to 62 meV for $(Sr,Bi)TiO_3$ [31], 12 meV for $(Sr,Ca)TiO_3$ [32], and 100 meV for TiO_2 [33]. Such small activation energies have been attributed to hopping of electrons between traps generated e.g. by off-center defects.

There is hence an implication that the intrinsic dielectric constant of the ferroelectric materials does indeed increase as the slab thickness is decreased. This contrasts with other observations on single-film capacitors where it is well known that the dielectric constant drops off dramatically as thickness is reduced [34,35]. When the thickness of each slab is very thin the behavior of the superlattices is very similar to a simple ferroelectric with a first-order phase transition. This is understandable because, in this case, the long-range order within each slab is greatly suppressed; this is especially true in BTO which has a larger critical size.

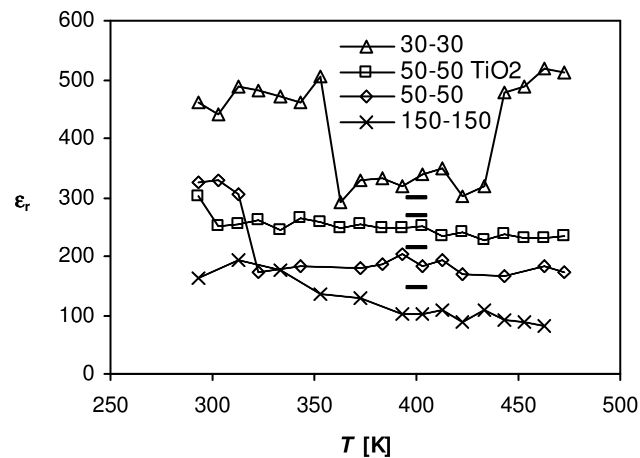

(a)

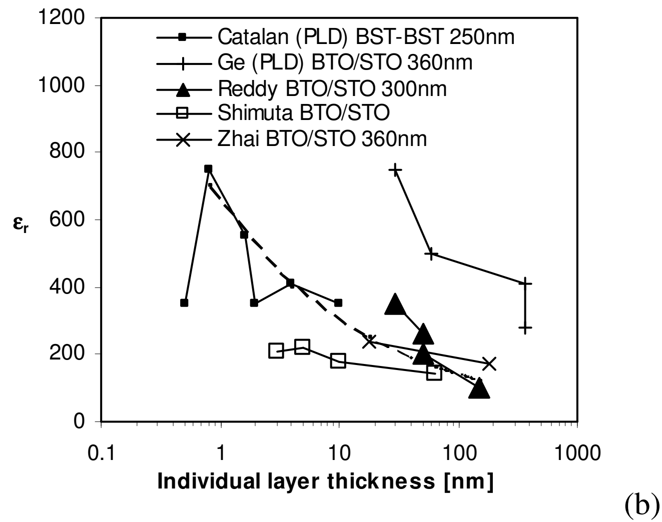

(b)

Fig. 7.5 Permittivity of the bulk grains calculated from the RC simulations of (a) C-H-B-S series heterostructures, (b) literature comparison of heterostructures.

And it is observed from the Fig. 7.5(a) in our BTO/STO system that the dielectric constant of the heterostructures is enhanced as the superlattice periodicity is increased up to $[BTO_{30\,nm}/STO_{30\,nm}]_{6,}$ which shows the dielectric constant ~461. Zhai et al [36] also observed that the $[BTO_{90\,nm}/STO_{90\,nm}]_{2}$ periodicity shows the bigger dielectric constant, than more or less of this periodicity.

Results similar to ours were obtained by Ge et al. [42] for the $[BTO_{30\,nm}/STO_{30\,nm}]_{6}$ stacking periodicity, it can be observed from Fig. 7.5(b). They observed a dielectric constant of 721 at 10 kHz. They explained that space charge may be produced at the interface between BTO and STO layers, which will lead to the formation of a special layer of high conductivity compared with the bulk of BTO and STO that have low conductivity. The film stacks consisting of two layers differing in electrical conductivity must give rise to the dielectric enhancement corresponding to the Maxwell-Wagner model. Such results were observed by O'Neill and Catalan et al.

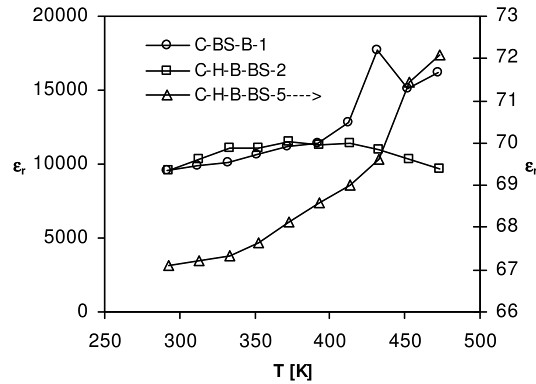

Fig. 7.5(c) Permittivity of the bulk grains calculated from the RC simulations of C-H-B-BS heterostructure series

From Fig. 7.5(c) shows the dielectric constant vs. temperature for the BTO/BST-0.75 heterostructures. The results shows that, $[BTO_{30\,nm}/BST_{30\,nm}]_6$ deposited at 600°C and $[BTO_{150\,nm}/BST_{150\,nm}]_1$ heterostructure deposited at 700°C shown much larger dielectric constant. The heterostructures of $[BTO_{50\,nm}/STO_{50\,nm}]_3$ which deposited at 700°C and annealed in N_2 shown much lower dielectric constant, it might be, because of high concentration of oxygen defects.

Shimuta et al. [37] also reported similar results: $(BTO_5/STO_5)_{\sim 250}$ with 5 unit cells shows a large dielectric constant (~250) that decreases with increasing layer thickness. This is because the individual layer thickness of the BTO or STO layer is above the critical thickness, which is about two unit cells according to O'Neill et al [38]. Shimuta et al. explained that the lattice parameter *c* of the BTO and STO in the superlattices decreases with increasing layer thickness, because the strain induced by the lattice mismatch between the in-plane lattice parameters of BTO and STO is relaxed with increasing thickness. Hence, the dielectric constant of the superlattices decreases, according to the strain-induced mechanism [39]. The sample (C-H-B-S-2) deposited on additional TiO_2 layer shows similar ε_r value like other samples, but shown larger overall resistance in the film (300 Ω). It is well known that TiO_2 will enhance the crystalline growth of the films [40,41]. This implies that a TiO_2 buffer layer can effectively serve as the high quality growth template of the perovskite film and improves the electrical properties.

It is well known that the dielectric constants of pure BTO and BST decrease with decreasing film thickness [43,44]. Tabata et al. reported that the superlattice structure and the stress present at the interface between the STO and BTO layers apparently play an important role in the variation of the dielectric constants. Kim et al. [45] reported that the dielectric constant of the BTO/STO heterostructures decreases as the thickness of the individual layers decreases due to severe lattice distortions of the BTO layer. It is expected that a reduction of the strain occurs with increasing thickness of the individual BTO/STO layers [46].

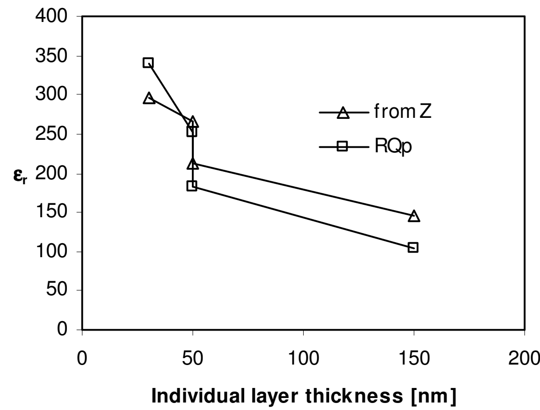

Fig. 7.5(d) dielectric constant vs. individual layer thickness of C-H-B-S series (Traingles: obtained from Eq.(1) and Sqaures: obtained from RQ simulations).

From Fig. 7.5(d) it is clear that, for BTO/STO system the dielectric constant increasing with decreasing the individual layer thickness. It is much evident from the literature that, for BTO/STO ferroelectric (FE)/paraelectric (PE) heterostructures system the dielectric constant enhancement is not larger and is similar like single layer films of BTO (ε_r=260) and STO (ε_r =230). But for ferroelectric/ferroelectric (FE/FE) heterostructures many researchers observed larger enhancement of dielectric constant for $PbTiO_3/Pb_{1-x}La_xTiO_3$ superlattices [Erbil et al.] and for $PbTiO_3/BaTiO_3$ superlattices [Ohya et al.]. Many theoretical studies explained that, these are effects of compositionally broken inversion symmetry and ultimately contribute to the linear and non-linear dielectric properties [48], compositional inhomegeneity always leads to broken inversion symmetry. Experimental observations and theoretical studies [49,50,51,52,53] clearly suggest that there is a strong interlayer coupling of the layers that must be considered to account for the properties of FE heterostructures. This interlayer coupling might be the long-range

interactions of FE/FE heterostructures, as it is already interpreted for $KTaO_3/KNbO_3$ system experimentally and theoretically by Christen et al. [54] and Shen et al. In our case we are not sure which are responsible.

Dielectric loss (tan δ)

The dielectric loss (tan δ) of the capacitors is calculated from:

$$\tan\delta = -\frac{Z'}{Z''} \qquad (3)$$

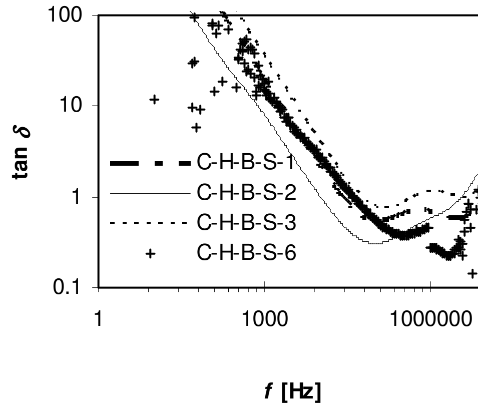

Fig. 7.6 Dielectric loss of C-H-B-S series heterostructures.

where Z' and Z'' are the real and imaginary part of the complex impedance, respectively. Our results are shown in Fig. 7.6, it can be observed that dielectric loss is much larger compare with normal films and Catalan et al also observed larger dielectric loss more than 2 for the heterostructures. Souni et al. [55] also observed dielectric loss of about 5 for Pd compound films.

7.4 Conclusions

In conclusion, we have demonstrated that artificial oxide heterostructures of thin film $BaTiO_3$/ $Ba_{0.75}Sr_{0.25}TiO_3$ provides remarkably improved dielectric properties, which might be

closely related with the lattice distortion of the consisting layers in the heterostructures and also might be the interlayer coupling of these two ferroelectric layers. But heterostructures of $BaTiO_3/SrTiO_3$ does not show larger than single phase films of $BaTiO_3$ or $SrTiO_3$. These effects can be explained by means of Maxwell-Wagner relaxation. The enhancement of the real part of the dielectric constant is an artifact produced by carrier migration to interface within the dielectric. It is needed to study the polarization properties of these heterostructures system.

References

[1] T. Shimuta, O. Nakagawara, T. Makino, S. Arai, H. Tabata and T. Kawai *J. Appl. Phys.* **91** 2290 (2002)

[2] O. Nakagawara T. Shimuta, T. Makino, S. Arai H. Tabata and T. Kawai *Appl. Phys. Lett.* **77** 3257 (2000)

[3] H. Tabata, H.Tanaka, and T. Kawai *Appl. Phys. Lett.* **65** 1970 (1994)

[4] H. N. Lee, H. M. Christen, M. F. Chisholm, C. M. Rouleau and D. H. Lowndes *Nature* **433**, 395 (2005)

[5] A. Erbil, Y. Kim and R. A. Gerhardt *Phys. Rev. Lett.* **77** 1628 (1996)

[6] B. D. Qu, M. Evstgneev, D. Johnson and R. H. Prince *Appl. Phys. Lett*. **72** 1394 (1998)

[7] G. Catalan, D. O' Neill, R. W. Bowman and J. M. Gregg *Appl. Phys. Lett.* **77** 3078 (2000)

[8] L. Kim and D. Jung *Appl. Phys. Lett*. **82** 2118 (2003)

[9] J. Kim, Y. Kim, Y. S. Kim, J. Lee, L. Kim and D. Jung *Appl. Phys. Lett.* **80** 3581 (2002)

[10] J. B. Neaton, C. –L. Hsueh and K. M. Rabe *Mat. Res. Symp. Proc.* **718** D10.26.1 (2002)

[11] J. B. Neaton and K. M. Rabe *Appl. Phys. Lett*. **82** 1586 (2003)

[12] D. O'Neill, R. M. Bownman and J. M. Gregg *Appl. Phys. Lett.* **77** 1520 (2000)

[13] W. J. Kim, W. Chang, S. B. Qadri, J. M. Pond, S. W. Kirchoefer, D. B. Chrisey and J. S. Horwitz *J. Appl. Phys*. **76** 1185 (2000)

[14] W. J. Kim, H. D. Wu, W. Chang, S. B. Qadri, J. M. Pond, S. W. Kirchoefer, D. B. Chrisey and J. S. Horwitz *J. Appl. Phys*. **88** 5448 (2000)

[15] C. H. Park and D. J. Chadi *Phys. Rev. B* **57** R13 961 (1997)

[16] X. –H. Zhu, H. L. –W. Chan, C. –L. Choy and K. –H. Wong *Appl. Phys. A* **80** 591 (2005)

[17] C. N. Rao and G. V. Subba Rao, National Bureau of Standards Report No. NSRDS-NBS49, 1974

[18] L. Krusin-Elbaum and M. Wittmer *J. Electrochem. Soc.* **135** 2610 (1998)

[19] S. –H. Paek, K. –S. Lee, J. –Y. Sung, S. –Y. Son, C. –S. Park and J. –H. Chung *J. Mater. Sci. Lett.* **17** 95 (1998)

[20] M. Li, A. Feteira and D. C. Sinclair *J. Appl. Phys* **98** 084101 (2005)

[21] M. Mahesh Kumar and M.L. Post *J. Appl. Phys.* **97** 114916 (2005)

[22] S. Sen, P. Pramanik and R.N.P. Choudhary *Appl. Phys. A* **82** 549 (2006)

[23] J. Yu, T. Ishikawa, Y. Arai, S. Yoda, M. Itoh and Y. Saita *Appl. Phys. Lett*. **87** 252904 (2005)

[24] J. E. Diosa, R. A. Vargas, I. Albinsson and B. –E. Mellander *Solid State Commun.* **136** 601(2005)

[25] P. C. Joshi and S. B. Krupanidhi *J. Appl. Phys* **73** 7627 (1993)

[26] J. D. Yu, P. F. Paradis, T. Ishikawa and S. Yoda *Appl. Phys. Lett*. **85** 2899 (2004)

[27] C. C. Homes, T. Vogt, S. M. Shapiro, S. Wakimoto and A. P. Ramirez *Science* **293** 673 (2001)

[28] M. Maglione and M. Belkaoumi *Phys. Rev. B* **45** 2029 (1992)

[29] Y. J. Li, X. M. Chen, R. Z. Hou and Y. H. Tang *Solid State Commun.* **137** 120 (2006)

[30] B. Prijamboedi, H. Takashima, R. Wang, A. Shoji and M. Itoh *Phys. Stat. Sol. (a)* **202** R152 (2005)

[31] C. Ang and Z. Yu *Phys. Rev. B* **61** 11363 (2000)

[32] W. Kleemann and H. Schremmer *Phys. Rev. B* **40** 7428 (1989)

[33] B. Karunagaran, S. J. Chung, E. –K. Suh and D. Mangalaraj *Physica B* **369** 129 (2005)

[34] S. B. Desu *Mater. Res. Soc. Symp. Proc.* **541** 457 (1999)

[35] W. Lee, H. Kim and Y. Yoon *J. Appl. Phys.* **80** 5891 (1996)

[36] J. Zhai, T. F. Hung and H. Chen *Appl. Phys. Lett.* **85** 2026 (2004)

[37] T. Shimuta, O. Nakagawara, T. Makino, S. Arai, H. Tabata, and T. Kawai *J. Appl. Phys.* **91** 2290 (2002)

[38] D. O. Neill, R. M. Bowman and J. M. Gregg *Appl. Phys. Lett.* **77** 1520 (2000)

[39] H. Tabata, H. Tanaka and T. Kawai *Appl. Phys. Lett.* **65** 1970 (1994)

[40] H-S. Kim, H-G. Kim, I-D. Kim, K-B. Kim and J-C. Lee *Appl. Phys. Lett.* **87** 212903 (2005)

[41] T. Higuchi,, M. Nakamura, Y. Hachisu and M. Saitoh *Jpn. J. Appl. Phys.* **43** 6585 (2004)

[42] S. Ge, Z. Ning, Z. Dong and M. Shen *J. Phys. D: Appl. Phys.* **35** 906 (2002)

[43] Y. Yano, K. Iijima, Y. Daitoh, T. Terashima and Y. Bando *J. Appl. Phys.* **76** 7833 (1994)

[44] C. B. Parker, J. –P. Maria and A. I. Kingon *Appl. Phys. Lett.* **81** 340 (2002)

[45] J. Kim, L. Kim, D. Jung, Y. S. Kim, W. Kim, J. H. Je and J. Lee *Jpn. J. Appl. Phys*. **42** 5901 (2003)

[46] A. Visinoiu, R. Scholz, S. Chattopadhyay, M. Alexe and D. Hesse *Jpn. J. Appl. Phys.,* Part 1 **41** 6633 (2002)

[47] Y. Ohya, T. Ito and Y. Takahashi *Jpn. J. Appl. Phys.* **33** 5272 (1994)

[48] N. Sai, K. M. Rabe and D. Vanderbilt *Phys. Rev. B* **66** 104108 (2002)

[49] B. D. Qu, W. L. Zhong and R. H. Prince *Phys. Rev. B* **55** 11218 (1997)

[50] J. Shen and Y. Q. Ma *Phys. Rev. B* **61** 14279 (2000)

[51] M. Sepliarsky, S. R. Phillpot, D. Wolf, M. G. Stachiotti and R. L. Migoni *Phys. Rev. B* **64** 060101 (2001)

[52] Z. G. Ban, S. P. Alay and J. V. Mantese *Phys. Rev. B* **67** 184104 (2003)

[53] Y. Zhou, H. K. Chan, C. H. Lam and F. G. Shin *J. Appl. Phys.* **98** 034105 (2005)

[54] H.-M. Christen, E. D. Specht, D. P. Norton, M. F. Chisholm and L. A. Boatner *Appl. Phys. Lett*. **72** 2535 (1998)

[55] M. Es-Souni, E. Girdauskaite, S. Iakovlev, C.-H. Solterbeck and V. Zaporojtchenko *J. Appl. Phys* **96** 5691 (2004)

Summary

We have prepared thin film capacitors with $SrTiO_3$, $BaTiO_3$ and $BaTiO_3/SrTiO_3$ heterostructures as dielectric material by rf magnetron sputtering. RuO_2 was used as electrode material for systematic perovskite material investigation. The O_2 partial pressure and the substrate temperature were systematically varied during the deposition.

For all dielectric materials the grain boundary resistance increased with increasing oxygen partial pressure. For $BaTiO_3$ a medium oxygen partial pressure and high temperature is suitable to get good dielectric properties: the dielectric constant is temperature and frequency independent. The transition temperature shifted to lower values when the films are deposited with high O_2 partial pressure.

Thin films of $BaTiO_3$, $SrTiO_3$ and $(Ba_xSr_{1-x})TiO_3$ are promising ferroelectrics for applications in future ultra-large scale integrated electronic circuits, e.g. dynamic random access memories (DRAM) and tunable microwave device applications, because these materials show high insulating properties with large values of relative permittivity The high relative dielectric constant of perovskite films can shrink the size of circuits and at the end it is easy to miniaturize the electronic devices into the nano-scale range.

Thin films of oxygen deficient $BaTiO_3$ were prepared by radio-frequency magnetron sputtering at substrate temperatures from 450 to 750°C and analyzed by x-ray diffraction, optical transmittance and Raman spectroscopy. Optical transmittance spectra were simulated by the SCOUT 2 simulation software to obtain the optical constants. The packing density of the films relative to the crystalline density increases from 0.75 at 450°C to about 1 at 750°C. At a substrate temperature of 450°C, the film is nanocrystalline (5 to 20 nm) with big lattice expansion, large band gap and pronounced hexagonal Raman lines. This film is homogeneous in the thickness direction. Films prepared at higher temperatures exhibit perovskite peaks in the Raman spectrum and an optical band gap of 3.38 eV. At 600 °C, the film exhibits a pronounced two-phase growth with a porous nucleation layer of initial packing density of 0.78, a preferred (100)-orientation of

the grains and minimum micro-strain. At 750°C, the films are again homogeneous in the thickness direction, have nearly crystalline packing density and preferably (110)-oriented grains.

Thin films of conductive ruthenium oxide (RuO_2) have been deposited at different substrate temperatures on various substrates by radio-frequency (rf) magnetron sputtering and were later annealed at different temperatures. The thickness of the films ranges from 50 to 700 nm. Films deposited at higher temperatures show larger grain size (about 140 nm) with (200) preferred orientation. Films deposited at lower substrate temperature have smaller grains (about 55 nm) with (110) preferred orientation. The electrical resistivity decreases slightly with increasing film thickness but is more influenced by the deposition and annealing temperature. Maximum resistivity is 640 μΩcm, observed for films deposited at room temperature on glass substrates. Minimum resistivity is 40 μΩcm observed for a thin film (50 nm) deposited at 540°C on a quartz substrate. Micro-Raman investigations indicate that strain-free well-crystallized thin films are deposited on oxidized Si substrates.

Thin film capacitors of $SrTiO_3$ with RuO_2 top and bottom electrodes on Si substrates were prepared by radio-frequency magnetron sputtering at substrate temperatures 500 and 700 °C and at various oxygen partial pressures. The thickness of the dielectric layer was varied between 200 and 900 nm. The impedance spectra of these samples could be interpreted with an equivalent circuit comprising a resistance and two RC or RQ --parallel elements in series. The dielectric permittivity ε_r of the bulk grains, as extracted from the high-frequency semicircle in the Cole-Cole plot, was in the range 300 to 600. High oxygen contents lead to high values of ε_r but also increase the grain boundary resistance.

Thin film capacitors with $BaTiO_3$ as dielectric and RuO_2 as electrode material have been prepared by rf-magnetron sputtering at temperatures up to 750°C and under various oxygen partial pressures. The dielectric constant at room temperature ranges from 120 to 1500, depending on the preparation conditions. There is a maximum in the temperature dependence of ε_r that shifts to lower temperatures when the capacitors have been prepared with more oxygen. Biggest dielectric permittivity and lowest dielectric loss are obtained for films prepared at 750°C at medium oxygen partial pressures. With increasing oxygen content the grain boundary effect

becomes stronger for the films prepared at all deposition temperatures. The films prepared with high oxygen partial pressure show increased crystallinity and dense columnar structure.

Three capacitors with of $Ba_{0.75}Sr_{0.25}TiO_3$ as dielectric were prepared and submitted to different post heating treatments. The deposition and annealing (in oxygen and vacuum) results in a significant difference in the dielectric properties of BST-0.75 thin films. The dielectric constant in the low-frequency region is found to be very large for the oxygen annealed film and small for the vacuum annealed film. For the as-deposited film the dielectric constant is relatively low (~500). Dielectric constant at low frequency is probably from the non-uniform charge accumulation at grain-boundaries.

Thin film capacitors with several layers of $BaTiO_3/SrTiO_3$ and $BaTiO_3/$ $Ba_{0.75}Sr_{0.25}TiO_3$ as dielectric were fabricated by rf magnetron sputtering. The properties of the capacitors were investigated as a function of the heterostructure periodicity. The dielectric constant was increased with decreasing the individual layer thickness of $BaTiO_3/SrTiO_3$. The dielectric constant was significantly enhanced up to ~100000 for the $BaTiO_3/$ $Ba_{0.75}Sr_{0.25}TiO_3$ system. This is thought to be an artifact produced by space charge regions due to carrier migration to the interfaces within the dielectric.

Zusammenfassung

Wir haben Dünnschichtkondensatoren mit $SrTiO_3$, $BaTiO_3$ und $BaTiO_3$/ $SrTiO_3$ -Heterostrukturen als dielektrisches Material durch RF-Magnetronsputtern hergestellt. Für diese systematische Perovskitematerialuntersuchung wurde RuO_2 als Elektrodenmaterial verwendet. Der O_2-Partialdruck und die Substrattemperatur wurden bei den Beschichtungen systematisch verändert.

Für alle dielektrischen Materialien erhöhte sich der Korngrenzenwiderstand bei Zunahme des O_2-Partialdrucks. Für $BaTiO_3$ ist ein mittlerer Sauerstoffpartialdruck und eine hohe Substrattemperatur geeignet um gute dielektrische Eigenschaften zu erhalten: die Dielektrizitätskonstante ist temperatur- und frequenzunabhängig. Die Übergangstemperatur verschob sich zu niedrigeren Werten, wenn die Filme bei hohem O_2-Partialdruck abgeschieden wurden.

Dünne Schichten aus $BaTiO_3$, $SrTiO_3$ und $(Ba_xSr_{1-x})TiO_3$ sind viel versprechende Ferroelektrika für Anwendungen in Dynamic Random Access Memories (DRAM) und abstimmbaren Mikrowellenbausteinen, denn diese Materialien zeigen hohe Isolationseigenschaften in Verbindung mit großen Werten für die relative Permittivität. Die hohe Dielektrizitätskonstate von Perovskiteschichten kann die Größe von Schaltkreisen minimieren um so am Ende Elektronikbausteine bis in die Nanometerregion zu verkleinern.

Unseres Wissens wurden in dieser Arbeit zum ersten mal dünne Schichten aus sauerstoffarmem $BaTiO_3$ durch Radiofrequenzmagnetronsputtern bei Substrattemperaturen von 450 bis 750°C hergestellt. Diese wurden mit Röntgenbeugung, optischer Transmissions- und Ramanspektroskopie analysiert. Die optischen Transmissionsspektren wurden mit der Simulationssoftware SCOUT 2 simuliert und ergaben die optischen Konstanten. Die Packungsdichte der Schichten relativ zur Kristalldichte stieg von 0,75 bei 450°C bis ungefähr 1 bei 750°C. . Bei Substrattemperaturen von 450°C, ist die Schicht nanokristallin (5 bis 20 nm) mit großer Gitteraufweitung, großer Bandlücke and ausgeprägten hexagonalen Ramanlinien. Diese Schicht ist in der Wachstumsrichtung homogen. Schichten die bei höheren Substrattemperaturen

abgeschieden wurden zeigen Perovskitlinien im Ramanspektrum und eine optische Bandlücke von 3.38 eV. Bei 600 °C, zeigen die Schichten ein ausgeprägtes Zweiphasenwachstum. Mit einer porösen Nukleationslage mit einer anfänglichen Packungsdichte von 0.78, einer bevorzugten (100)-Orientierung der Körner und minimaler Mikrospannung. Bei 750°C, sind die Schichten wieder homogen in der Wachstumsrichtung, haben nahezu kristalliene Packungsdichte und bevorzugt (110)-orientierte Körner.

Dünne Schichten aus leitfähigen Rutheniumoxid (RuO_2) wurden bei unterschiedlichen Substrattemperaturen auf verschiedenen Substraten durch Radiofrequenz -(rf) Magnetronsputten abgeschieden and später bei unterschiedlichen Temperaturen ausgelagert. Die Schichtdicke reichte von 50 bis 700 nm. Schichten die bei höheren Temperaturen abgeschieden wurden, zeigen größere Körner (um 140 nm) mit einer (200) Vorzugsrichtung. Schichten die bei niedrigeren Temperaturen abgeschieden wurden, zeigen kleinere Körner (um 55 nm) mit einer (110) Vorzugsrichtung. Der spezifische elektrische Widerstand nimmt mit wachsender Schichtdicke etwas ab, wird aber hautsächlich durch die Abscheide- und Auslagerungstemperatur bestimmt. Der maximale spezifische Widerstand von 640 μΩcm, wurde bei Schichten die bei Raumtemperatur auf Glassubstraten abgeschieden wurden beobachtet. Der minimale spezifische elektrische Widerstand von 40 μΩcm wurde bei einer Schicht die bei 540°C auf einem Quarzsubstrat abgeschieden wurde. Mikroramanuntersuchungen zeigen das spannungsfreie gut kristallinisierte Schichten auf oxidiertem Si-Substraten abgeschieden wurden.

Dünnschichtkondensatoren aus $SrTiO_3$ mit RuO_2 als obere und untere Elektrode wurden auf Si- Substraten mit Radiofrequenzmagnetronsputtern bei Substrattemperaturen von 500°C und 700 °C und bei unterschiedlichen Sauerstoffpartialdrücken hergestellt. Die Dicke der dielektrischen Lage wurde von 200 bis 900 nm variiert. Das Impedanzspektrum dieser Proben kann mit einem Ersatzschaltbild aus einem Widerstand und zwei RC-Parallelelementen in Serie interpretiert werden. Die Dielektrizitätskonstante ε_r der ganzen Körner, wie aus den Hochfrequenzhalbkreisen im Cole-Cole- Diagramm berechnet, war im Bereich von 300 to 600. Hoher Sauerstoffgehalt führt zu hohen Werten von ε_r, aber auch zu höherem Korngrenzenwiderstand..

Dünnschichtkondensatoren mit $BaTiO_3$ als Dielektrikum und RuO_2 als Elektrodenmaterial wurden mit Radiofrequenzmagnetronsputtern bei Temperaturen bis zu 750°C und bei unterschiedlichen Sauerstoffpartialdrücken hergestellt. Sie wurden mit Komplexer Impedanzspektroskopie im Temperaturbereich von 20 bis 200°C analysiert. Die Aktivierungsenergien der Leitfähigkeit sind im Bereich von 30 bis 100 meV, was charakteristisch für hopping Elektronen ist. Die Dielektrizitätskonstante bei Raumtemperatur variiert 120 to 1500, in Abhängigkeit von den Präparationsbedingungen. Es gibt ein Maximum in der Temperaturabhängigkeit von ε_r das sich zu tieferen Temperaturen hin verschiebt, wenn die Kondensatoren bei höheren Sauerstoffpartialdrücken hergestellt wurden. Über dieser Temperatur, wurde Curie-Weiss-Verhalten mit charakteristischen Temperaturen im Bereich von 250 bis 400 K beobachtet. Die größte Dielektrizitätskonstante und der niedrigste dielektrische Verlust wurde bei Schichten beobachte, die bei 750°C und bei mittleren Sauerstoffpartialdrücken hergestellt wurden. Mit steigendem Sauerstoffgehalt wird der Korngrenzeneffekt unabhängig von der Beschichtungstemperatur stärker. Die Schichten, die mit hohem Sauerstoffpartialdruck hergestellt wurden zeigen eine verbesserte Kristallinität und eine dichte Säulenstruktur.

Drei Kondensatoren mit $Ba_{0.75}Sr_{0.25}TiO_3$ als Dielektrikum wurden hergestellt und unterschiedlichen Wärmenachbehandlungen unterzogen. Die Beschichtung und das Ausheizen (in Sauerstoff und Vakuum) ergibt signifikante Unterschiede in der dielektrischen Eigenschaften von dünnen Schichten aus BST-0.75 . Es wurde ein sehr großer Wert für die Dielektrizitätskonstante im unteren Frequenzbereich für die in Sauerstoff ausgeheizte und ein sehr niedriger für die im Vakuum ausgeheizte Schicht gefunden. Bei der nicht nachbehandelten Schicht ist die Dielektrizitätskonstante relativ niedrig (~500). Die Dielektrizitätskonstante im unteren Frequenzbereich wird vermutlich von eine ungleichmäßigen Ladungsanreicherung an den Korngrenzen verursacht.

Dünnschichtkondensatoren mit mehreren lagen von $BaTiO_3/SrTiO_3$ und $BaTiO_3/Ba_{0.75}Sr_{0.25}TiO_3$ als Dielektrikum wurden mit RF-Magnetronsputtern hergestellt. Die Eigenschaften der Kondensatoren wurden im Hinblick auf die Heterostrukturperiodizität untersucht. Die Dielektrizitätskonstante wurde mit abnehmender, individueller Schichtdicke von $BaTiO_3/SrTiO_3$ erhöht. Die Dielektrizitätskonstante wurde signifikant bis zu ~100000 für das

$BaTiO_3$/ $Ba_{0.75}Sr_{0.25}TiO_3$-System erhöht. Dies ist anscheinend ein Artefakt produziert von Raumladungszonen die durch Ladungsträgerabwanderung zur Grenzfläche innerhalb des Dielektrikums hervorgerufen werden.

సంగ్రహం

పలుచని పొరలైన $BaTiO_3$, $SrTiO_3$ మరియు$(Ba_xSr_{1-x})TiO_3$లు బహుళ ప్రయోజనకరమైనవి, ఫెర్రో విద్యుత్ వినియోగమునకు ఉపయోగపడును ఉదా :- డైనమిక్ రాండమ్ యాక్సస్ మెమొరీస్(DRAM), సరళమైన సూక్ష్మ తరంగ పరికరములలో. ఎందుకంటే ఇవి హెచ్చు నిరోదకత్వమును ప్రదర్శించును, దానితోపాటు హెచ్చు సాపేక్ష పర్మిటివిటీని ప్రదర్శించును. ఈ ధర్మములను ప్రదర్శించు పెరోస్కైట్ పొరలను, వలయాలయొక్క పరిమాణంను తగ్గించి సూక్ష్మపరిమాణం గల ఎలక్ట్రానిక్ పరికరాలను తయారు చేయవచ్చు.

మాకు తెలిసినంతవరకు మేమే మొదటిసారి ఆమ్లజని లోపముకల్గిన $BaTiO_3$ పొరలను నిస్తంతి పౌనఃపుణ్య అయస్కాంతత్వ తుంపర్లద్వారా 450°C నుంచి 750°C ఉష్ణోగ్రతల వద్ద నిక్షేపించాము. వీటిని X-కిరణ వివర్తనము, చక్షుష వర్ణపట మరియు రామన్ వర్ణపట విజ్ఞానం ద్వారా వాటిని విశ్లేషించాము. చక్షుష సమాచార విలువలను SCOUT 2 చేత అభికరణచేశాం, దీనిద్వారా చక్షుష స్థిరాంకాలను రాబట్టాము. పొరలను హెచ్చు ఉష్ణోగ్రతలవద్ద నిక్షేపించినపుడు అవి పెరోస్కైట్ రూపమును రామన్ పటంలో గమనించాము మరియు వాటి యొక్కచక్షుష పట్టిక శూన్యత విలువ 3.38 eV, 600°C, ఉష్ణోగ్రత వద్ద నిక్షేపించిన పొర రెండు దశలుగా వృద్ధిచెందింది. 750°C వద్ద నిక్షేపించిన పొర సజాతీయంగా మందంవైపు వృద్ధిచెందును.

వాహక పొరలైన RuO_2 ను వివిధ ఉష్ణోగ్రతలవద్ద తయారుచేసి మరియు అనీలనము చేయడం జరిగింది. పొరలయొక్క మందం 50 నుండి 700 nm పొరలను హెచ్చు ఉష్ణోగ్రతల వద్ద తయారుచేసినపుడు పెద్దకణాలు (140 nm) తో (200) విన్యాసం ఏర్పడ్డాయి. పొరలు తక్కువ ఉష్ణోగ్రతల వద్ద తయారు చేసినపుడు చిన్న కణాలు (55 nm) లతో (110) విన్యాసంతో ఏర్పడ్డాయి. విద్యుత్‌నిరోధకత్వం పొరల మందం తగ్గినపుడు హెచ్చును. కానీ, నిక్షేపించే ఉష్ణోగ్రతలు ఎక్కువ ప్రభావం చూపెను. ఎక్కువ నిరోధము 640 $\mu\Omega$cm ను గదిఉష్ణోగ్రతల వద్ద చేసిన పొరలో గమనించాము. తక్కువ నిరోధకమును 540°C వద్ద తయారుచేసిన పొరలో గమనించాము. సూక్ష్మ రామన్ పరిశోధనలో వికృతిలేని స్ఫటికాకార పొరలను Si మీద నిక్షేపించాము.

పలుచని పొరలైన $SrTiO_3$ లను RuO_2 తో పైన మరియు క్రింద విద్యుతప్లాతో 500°C మరియు 700°C ఉష్ణోగ్రతలవద్ద మరియు వివిధమైన ఆమ్లజనితో పొరలయొక్క మందమును 50 నుంచి 700 nm నిక్షేపించాము. ఈ పొరల అవరోధము వర్ణపటవిజ్ఞానంచేత విశ్లేషించాము. వీటిని సమాంతర వలయములైన ఒక నిరోధము R మరియు రెండు RC or RQ లను శ్రేణి ద్వారా విశ్లేషించాము. విద్యుత్ నిరోధక ε_r పెద్ద కణములను హెచ్చు పౌనఃపున్య RC ల నుంచి రాబట్టాము. ఇవి 300 నుండి 600 మధ్య ఉన్నది. ఎక్కువ ఆమ్లజనితో హెచ్చు విద్యుత్ నిరోధమును పొందవచ్చును, కానీ కణహద్దులయొక్క నిరోదంకూడా పెరుగును.

$BaTiO_3$ పలుచని పొరలను RuO_2 విద్యుతప్లాతో వివిధ ఆమ్లజనితో నిక్షేపించాము, వాని అవరోధ వర్ణపటంద్వారా విశ్లేషించాము. విద్యుత్ నిరోధము గది ఉష్ణోగ్రత 120 నుండి 1500 వరకు ఉంది. అధిక ఆమ్లజని వాడినపుడు అత్యధిక విద్యుత్ నిరోధము, తక్కువ ఉష్ణోగ్రతల నిరోధులును తక్కువ విద్యుత్ నిరోధక్షయంను 750°C వద్ద నిక్షిప్తం చేసిన మధ్య ఆమ్లజనితో చేసిన పొరలను చూపాయి. తక్కువ ఆమ్లజనితో నిక్షిప్తం చేసిన వాటియొక్క స్ఫటీకరణ పెరుగును.

పలుచటి పొరలైన $BaTiO_3$ / $SrTiO_3$ మరియు $BaTiO_3$ / $Ba_{0.75}$ $Sr_{0.25}$ TiO_3 ధారణిలను హిటరోస్ట్రక్షర్‌లను నిక్షేపించాము. వీటిని హిటరోస్ట్రక్షర్ ఆవర్తనంల ద్వారా పరిశోధించాము. పొరల యొక్క మందం తగ్గించిన $BaTiO_3$ / $SrTiO_3$ యొక్క విద్యుత్ నిరోధం పెరిగెను. తక్కువ పౌనఃపున్యం వద్ద $BaTiO_3$ / $Ba_{0.75}$ $Sr_{0.25}$ TiO_3 యొక్క విద్యుత్ నిరోధం ఎక్కువగా గమనించాము.

$Ba_{0.75}$ $Sr_{0.25}$ TiO_3 పొరల యొక్క స్వభావము నిక్షేపించు పద్ధతి మరియు అనీలనముతో చాలా సున్నితము. అనీలనము చేసిన పొరలు ఎక్కువ విద్యుత్ నిరోధనమును ప్రదర్శించెను. అనీలనము చేయని పొరల యొక్క విద్యుత్ నిరోదము తక్కువ.

Appendix A

(Source: Pradhan et al.[3])

Complex impedance spectroscopy (Complex IS)

Complex impedance spectroscopy (IS) is a relatively new and powerful method of characterizing many of the electrical properties of materials and their interfaces with electronically conducting electrodes. It may be used to investigate the dynamics of bound or mobile charge in the bulk or interfacial regions of any kind of solid or liquid material: ionic, semiconducting, mixed electronic-ionic and even insulators (dielectrics). Complex IS is a valuable tool for studying both the bulk transport properties of a material and the electrochemical reactions on its surface [1,2]. The value of IS derives from the effectiveness of the technique in isolating individual reaction/migration steps in a multi-step process. That is, because each reaction or migration step has, ideally, a unique time constant associated with it, these steps can be separated in the frequency domain. Experimentally, one applies a small sinusoidal current perturbation to an equilibrium system and measures the corresponding voltage response. The ratio of the voltage response to the current perturbation is the impedance.

The output response, when plotted in a complex plane plot, appears in the form of a succession of semicircles representing electrical phenomena due to bulk material, grain boundary, grain boundary effect and interfacial phenomena if any [3]. In view of this specialty, complex IS makes it possible to separate the contribution due to different components in a polycrystalline sample, which of course have different time constants, in the frequency domain.

Typically, IS experiments are carried out over a wide range of frequencies (several mHz to several MHz), and the interpretation of the resulting spectra is aided by analogy to equivalent circuits involving simple components such as resistor (R) and capacitor (C) in parallel (RC_p) and in series (RC_s). In general, such equivalent circuits are not unique, and indeed there exists an infinite set of circuits that can represent any given impedance. It is common to select a physically plausible circuit containing a minimal number of components and, in a somewhat ad hoc manner,

[3] D. K. Pradhan, B. K. Samantaray, R. N. P. Choudhary and A. K. Thakur *Mater. Sci. Eng.* B **116** 7 (2005)

assign physical significance to the derived parameters. Often, a meaningful insight into material behavior can be gained from such analyses, which certainly explains the rise in popularity of impedance spectroscopy as a materials characterization tool.

Nevertheless, some researchers think that such equivalent circuits are insufficient and that constant phase elements (CPE), Q, instead of capacitors should be used because of the (microstructural, compositional, etc.) inhomogeneity of polycrystalline materials. In such situations RQ_p- elements instead of RC_p- elements can be use. The impedance of Q is $A\cdot(i\omega)^{-\alpha}$ instead of $(i\omega C)^{-1}$ for a capacitor.

When there is more than one semicircle, we have to decide which one is related to the grain boundary and which to the bulk grain. From the literature it is known that the resistance and the capacitance of the grain boundaries are always larger than that of the bulk grains.
We conclude that the relaxation time $\tau = RC = \rho\varepsilon_r\varepsilon_0$ is larger for the grain boundaries. Consequently, the characteristic frequency $f_g = (2\pi\tau)^{-1}$ is relatively smaller and the semicircle of the grain boundaries occurs at lower frequencies. The grain resistance is determined from the high-frequency semicircle of the RC_p or RQ_p equivalent circuit. This procedure is well established in the literature. It has been applied in the case of many dielectric and ferroelectric materials [4,5].

The frequency dependent properties of a material are normally described in terms of any of the formalism expressed as follows. Complex IS gives a possibility to distinguish between different effects during the MIM capacitor test. The experimental data could be analyzed in terms of the complex formula for the impedance, $Z^*=Z'+jZ''$.

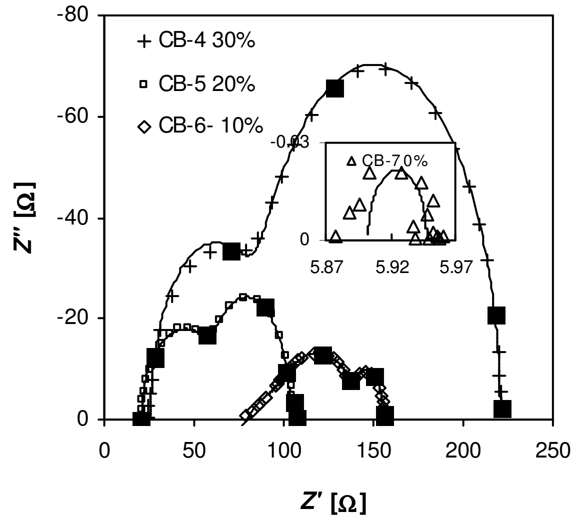

Fig. 1 Complex IS of $BaTiO_3$ thin films (our samples) deposited at different oxygen partial pressures at 600°C substrate temperature along with the RC_p simulated curves and decades.

Complex impedance $$Z^* = Z' + jZ'' = R_s + \frac{j}{\omega C_s} \quad (1a)$$

Complex admittance, $$Y^* = Y' + jY'' = \frac{1}{R_p} + j\omega C_p = G(\omega) + jB(\omega) \quad (1b)$$

Complex permittivity, $$\varepsilon^* = \varepsilon' + j\varepsilon'' \quad (1c)$$

Complex modulus, $$M^* = \frac{1}{\varepsilon^*} = M' + jM'' = j\omega C_0 Z^* \quad (1d)$$

And the dielectric loss $$\tan\delta = \frac{-Z'}{Z''} = \frac{Y'}{Y''} = \frac{\varepsilon''}{\varepsilon'} = \frac{M''}{M'} \quad (1e)$$

Where (Z', Y', ε', M') and (Z'', Y'', ε'', M'') are the real and imaginary components of impedance, admittance, permittivity and modulus, respectively. G: conductance, B: susceptance, and tan δ: dielectric loss. They are interrelated with each other. Each semicircular arc in the impedance spectrum has a characteristic peak occurring at a unique relaxation frequency (ω_{max}) attributed to electrical phenomena due to different components in the sample. It can be expressed as:

$$\omega_{\max} RC = \omega_{\max} \tau = 1 \qquad (2)$$

$$\Rightarrow \omega_{\max} = \frac{1}{\tau} = \frac{1}{RC}$$

$$\Rightarrow f_{\max} = \frac{1}{2\pi R_b C_b}$$

Relaxation frequency and hence relaxation time (τ) is a parameter that depends only on the intrinsic properties of the material and not on the sample geometrical factors. The term intrinsic properties of the material refer to the properties attributed to structure/microstructure (i.e. grain interior or bulk, grain boundary, electrode interface). These properties govern the distribution of resistive and capacitive components in the material on which relaxation time ultimately depends in accordance with $\tau = RC$. So, the results obtained using impedance analysis is basically unambiguous and provide true picture of the samples' electrical behavior.

Dielectric permittivity (ε_r) could be extracted from the complex IS

$$\text{Where } \varepsilon^* = \frac{1}{j\omega C_0 Z^*}$$

Here it is real permittivity of the material $\varepsilon_r = \dfrac{-Z''}{(2\pi f C_0)(Z'^2 + Z''^2)}$ (4a)

The imaginary permittivity of the material is $\varepsilon_{im} = \dfrac{Z'}{(2\pi f C_0)(Z'^2 + Z''^2)}$ (4b)

Where f, C_0, Z', and Z" are frequency, permittivity of the free space (8.854×10^{-12} F/m), real part and imaginary parts of the impedance, respectively.

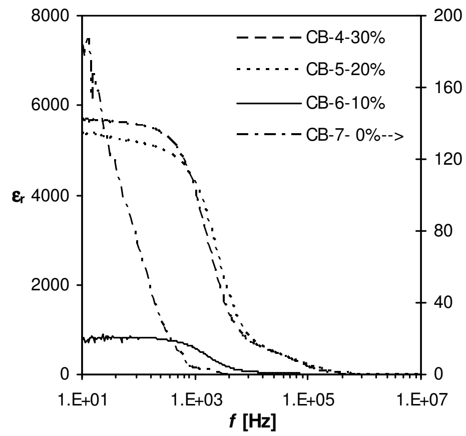

Fig. 2 dielectric permittivity of the $BaTiO_3$ thin films with respect to frequency calculated from Eq. 4b.

References

[1] S. P. Jiang, J. G. Love, and S. P. S. Badwal, ‘‘Electrochemical Techniques in Studies of Solid Ionic Conductors,’’ Key Eng. Mater., **125–126**, 81–132 (1997)

[2] J. R. MacDonald and W. B. Johnson, “Fundamentals of Impedance Spectroscopy” pp. 1–26 in Impedance Spectroscopy: Emphasizing Solid Materials and Systems, Edited by J. R. MacDonald. John Wiley and Sons, New York, 1987

[3] J. E. Bauerle, J. Phys. Chem. Solids **30** 2657 (1969)

[4] M. Mahesh Kumar, M. L. Post, J. Appl. Phys. **97** 114916 (2005)

[5] M. Li, A. Feteira, D. C. Sinclair, J. Appl. Phys. **98** 084101 (2005)

Appendix B

(Source: SCOUT 2 manual, www.mtheiss.com)

Optical constants:

In general the electric field of the source light wave that interacts with the sample and hence excitations can be observed in optical experiments that are going along with a polarization of the matter. The polarization P induced by an external electric field E in a homogeneous material is given by the electric susceptibility ℵ:

$$P = \varepsilon_0 \chi E \qquad (1)$$

The dielectric function ε which connects the dielectric displacement and the electric field vector is closely related to the susceptibility:

$$D = \varepsilon_0 \varepsilon E , \qquad \varepsilon = 1 + \chi \aleph \qquad (2)$$

The frequency dependence of the susceptibility is very characteristic for a material since it incorporates vibration of the electronic system and the atomic cores as well as contributions from free charge carriers.

a. Dielectric function models

Harmonic oscillator:

Microscopic vibrations involving the motion of the atomic nuclei (which are heavier than the electrons) usually have their resonance frequencies in the infrared region. These characteristic frequencies depend on the oscillating masses and the strength of the bonding between them and hence can be used for material identification. Susceptibilities describing microscopic vibrations can be modeled by harmonic oscillator terms:

$$\chi_{H.O} = \frac{\Omega_P^2}{\Omega_{TO}^2 - v^{\sim 2} - iv\Omega_\tau}. \quad (3)$$

Ω_p gives oscillator strength, $\Omega\tau$ damping and Ω_{TO} the resonance position. The index TO denote transverse optical phonon.

Drude model:

In the case of doped semiconductors and metals the charge carriers set free by the donors or acceptors can be accelerated by very little energies and hence do respond to applied electric fields with frequencies in the infrared region and free carries, respectively. A simple expression for the susceptibility of free carriers is given by Drude model where the carriers' concentration and a damping constant enter:

$$\chi_{Drude} = -\frac{\Omega_P^2}{v^2 + iv\Omega_\tau} \text{ with } \Omega_P^2 = \frac{ne^2}{\varepsilon_o m}. \quad (4)$$

where n is the volume density, e the charge and m the effective mass of the charge carriers, Ω_{p} is called plasma frequency, Ω_τ, the damping constant.

Inter-band transitions:

The most, generally used inter-band transition model is OJL [1] (O'Leary 1997A) where expressions for the joint density of states are given for the optical transition from the valence band to the conduction band. Parabolic bands are assumed with tail states exponentially decaying into the band gap.

The main important parameters in the SCOUT fit program: band gap energy E_{g}, the damping constant of the valence band, and the overall strengths of the transition expressed by a pre-factor called "mass" m. The imaginary part of the dielectric function is proportional to the

combined density of the states obtained from the above assumption on the density of states of the valence and conduction band.

In Fig. 1 we can see the simulated transmittance spectra of $BaTiO_3$ thin film deposited at 450°C (details can be find in Chapter 2) by using simple harmonic oscillator and OJL model, it fits quite well. From these simulations we can determine the optical constants like, e.g., band gap (E_g), refractive index (n), extinction coefficient (k), and absorption coefficient (α).

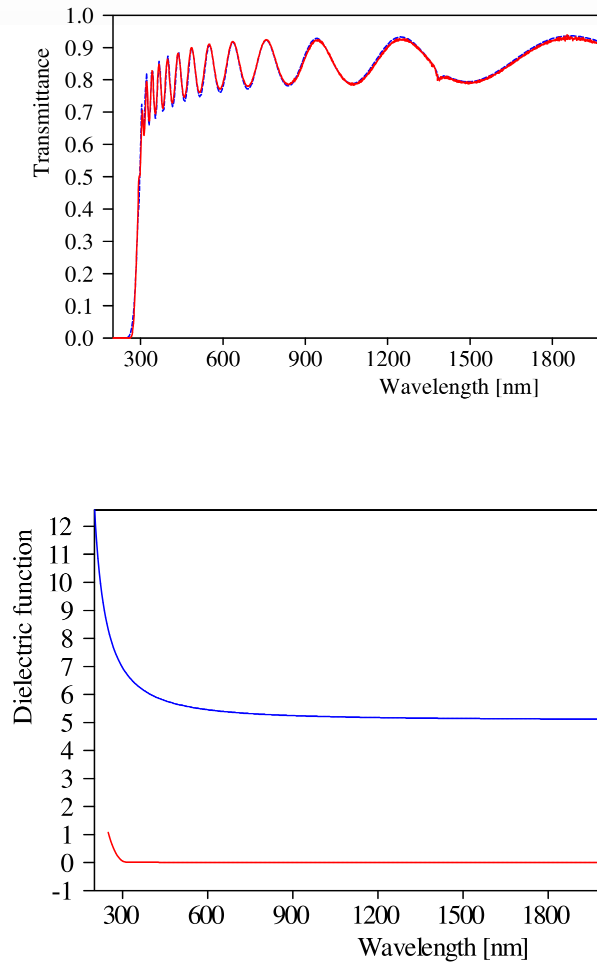

Fig. 1 Simulation of $BaTiO_3$ thin film deposited at 450°C

(a) Transmittance spectra along with simulated curve (dashed line)

(b) Dielectric function of BTO

b. Effective Medium Theory

The optical properties of inhomogeneous materials can be described by so-called effective dielectric functions, if the wavelength of the probing radiation is much larger than the typical sizes of the in-homogeneities of the system. In this case retardation effects can be neglected and the response of the mixed material to an incoming electromagnetic wave can be calculated in a quasi-static approximation.

Obviously the micro-geometry plays an important role for the effective dielectric function: for example, the embedded particles are metallic and the host material is an insulator the effective medium can show metallic or insulating behavior, depending on whether there is percolating network of the embedded particles or not.

There are several effective medium models; Maxwell Garnett [2], Bergman [3], and Bruggeman [4] are well known models.

Here we discuss on Bruggeman model, which is also known as an effective medium approximation (EMA) gives the relation in Eq. 5, and it is the most used effective medium concept.

$$(1-f)\frac{\varepsilon_M - \varepsilon_{eff}}{\varepsilon_M + 2\varepsilon_{eff}} + f\frac{\varepsilon - \varepsilon_{eff}}{\varepsilon + 2\varepsilon_{eff}} = 0 \tag{5}$$

For very low volume fraction it is equivalent to the Maxwell Garnett theory, but for increasing volume fraction its results are quite different. There is no percolation below $f = 1/3$, above that threshold the embedded particles are assumed to be partially connected. It is well fitted for the ferroelectric materials, and obtained satisfactory results, the results can be observe in chapters 1, 2, and 3.

Referenes

[1] S.K. O'Leary, S. R. Johnson and P. K. Kim *J. Appl. Phys.* **82** 3334 (1997)

[2] J. C. Maxwell Garnett *Phil. Trans. R. Soc. London* **203** 385 (1904)

[3] D. Bergman *Phys. Rep.* **C 43** 377 (1978)

[4] D. A. G. Bruggeman *Ann. Phys*. **24** 636 (1935)